SYNTHESIS, CHARACTERIZATION AND
ELECTROCHEMICAL PROPERTIES OF REDUCED
GRAPHENE OXIDE/FERRITE NANOCOMPOSITES

Isara Kotutha

A Thesis Submitted in Partial Fulfillment of the Requirements for the

Degree of Doctor of Philosophy in Physics

Suranaree University of Technology

Academic Year 2016

การสังเคราะห์ ลักษณะเฉพาะและสมบัติเชิงไฟฟ้าเคมี
ของวัสดุนาโนคอมพอสิตรีดิวซ์กราฟีนออกไซด์/เฟอร์ไรต์

นายอิศรา   โคตุทา

SYNTHESIS, CHARACTERIZATION AND ELECTROCHEMICAL PROPERTIES OF REDUCED GRAPHENE OXIDE/FERRITE NANOCOMPOSITES

Suranaree University of Technology has approved this thesis submitted in partial fulfillment of the requirements for the Degree of Doctor of Philosophy.
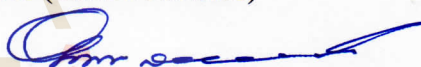
Thesis Examining Committee

_____
(Assoc. Prof. Dr. Prayoon Songsiriritthigul)

Chairperson

_____
(Prof. Dr. Santi Maensiri)

Member (Thesis Advisor)

_____
(Assoc. Prof. Dr. Ekaphan Swatsitang)

Member

_____
(Asst. Prof. Dr. Worawat Meevasana)

Member

_____
(Dr. Adisorn Tuantranont)

Member

_____
(Prof. Dr. Sukit Limpijumnong)

Vice Rector for Academic Affairs

and Innovation

_____
(Prof. Dr. Santi Maensiri)

Dean of Institute of Science

อิศรา โคตุทา : การสังเคราะห์ ลักษณะเฉพาะและสมบัติเชิงไฟฟ้าเคมีของวัสดุนาโน
คอมพอสิตรีดิวซ์กราฟีนออกไซด์/เฟอร์ไรต์ (SYNTHESIS,
CHARACTERIZATION AND ELECTROCHEMICAL PROPERTIES OF
REDUCED GRAPHENE OXIDE/FERRITE NANOCOMPOSITES). อาจารย์ที่
ปรึกษา : ศาสตราจารย์ ดร.สันติ แม้นศิริ, 113 หน้า.

งานวิจัยนี้ศึกษาการเตรียมวัสดุนาโนคอมพอสิตรีดิวซ์กราฟีนออกไซด์/เฟอร์ไรต์ โดยการ
ผสมเฟอร์ไรต์ลงบนแผ่นรีดิวซ์กราฟีนออกไซด์โดยวิธีไฮโดรเทอร์มอล การเตรียมวัสดุประกอบด้วย
การเตรียมผงกราไฟต์ออกไซด์ (GO) ด้วยวิธีของแฮมเมอร์แบบดัดแปลง (modified Hummers
method) ผงกราไฟต์ (graphite) ถูกออกซิไดซ์ในกรดเข้มข้น 98% H_2SO_4 ด้วยโพแตสเซียมเปอร์
มังกาเนต (KMnO$_4$) หลังจากกราไฟต์ผ่านกระบวนการออกซิไดซ์จะทำให้ระยะห่างระหว่างระนาบ
(d-spacing) ขยายความกว้างขึ้นจาก 0.33 nm เป็นประมาณ 0.88 nm โดยที่ตำแหน่งของการกระเจิง
รังสีเอกซ์จะมีการเปลี่ยน แปลงจากมุม 26.8° เป็น 10.70° จากนั้นผงกราไฟต์ออกไซด์จะถูกนำไป
ละลายในน้ำปราศจากไอออน (DI water) ด้วยความเข้มข้น 0.5 mg/ml โดยการเขย่าด้วยเครื่องเขย่า
ultrasonic เป็นเวลา 30 min รีดิวซ์กราฟีนออกไซด์ (rGO) เตรียมได้โดยใช้กระบวนการรีดิวซ์สาร
ละลายกราฟีนออกไซด์ด้วยไฮดราซีนโมโนไฮเดรต (H$_4$N$_2$ · H$_2$O) โดยวิธีไฮโดรเทอร์มอลที่อุณหภูมิ
200 °C เป็นเวลา 24 h การวิเคราะห์ด้วย XRD TEM และวิธีการกระเจิง Raman ใช้ยืนยันการเกิด
โครงสร้างของรีดิวซ์กราฟีนออกไซด์ พบตำแหน่งพีกที่แสดงลักษณะของโครงสร้างอสัณฐานเนื่อง
จากการเรียงตัวแบบสุ่มของแผ่น rGO ที่มุม 25.5° ในขั้นตอนการทดลอง Fe(NO$_3$)$_3$ · 9H$_2$O
Mn(NO$_3$)$_2$ · 6H$_2$O และ Co(NO$_3$)$_2$ · 6H$_2$O เป็นสารตั้งต้นในการเตรียมอนุภาคโลหะเฟอร์ไรต์
(CoFe$_2$O$_4$ และ MnFe$_2$O$_4$) ตรวจสอบการเกิดวัสดุผสมและศึกษาสมบัติพื้นฐานของโครงสร้างวัสดุ
ผสมที่เตรียมได้ด้วย XRD TEM FTIR และการกระเจิง Raman การวิเคราะห์ด้วย BET ใช้ในการ
ศึกษาความเป็นรูพรุนและพื้นที่ผิวต่อมวลจำเพาะ (specific surface area) ซึ่งพบว่าวัสดุผสมจะมีค่า
พื้นที่ผิวจำเพาะมากกว่าโลหะเฟอร์ไรต์แต่จะมีค่าน้อยกว่าแผ่น rGO เพียงอย่างเดียวเนื่องจากอนุภาค
ของโลหะเฟอร์ไรต์จะเข้าไปแทนที่ตำแหน่งรูพรุนของ rGO เมื่อนำวัสดุผสมที่ได้นี้ไปทำ เป็นขั้ว
ไฟฟ้า (working electrode) เพื่อวิเคราะห์สมบัติเคมีเชิงไฟฟ้า (electrochemical properties) ใน
สารละลายอิเล็กโทรไลต์ 6.0 M KOH โดยใช้การวัดแบบ 3 ขั้ว พบว่าค่าความจุไฟฟ้าจำเพาะที่วัด
ด้วยวิธี cyclic voltammetry (CV) มีค่าเท่ากับ 190.3 276.94 144.5 และ 203.5 F/g โดยมีอัตราการ
ให้ความต่างศักย์ 10 mV/s ในช่วงของการให้ความต่างศักย์ −1.0 − 0.0 V ในขณะที่ผลจากการวัด

274.6 134.4 และ 223.1 F/g ที่ความหนาแน่นกระไฟฟ้า 5.0 A/g สำหรับ rGO rGO/MFO05 rGO/MFO10 และวัสดุผสม rGO/CFO05 ตามลำดับ จากผลการทดลองพบว่าหากผสมเฟอร์ไรต์ลงบนแผ่น rGO จะทำให้ค่าความจุไฟฟ้าจำเพาะเพิ่มขึ้นแต่หากปริมาณของเฟอร์ไรต์มากเกินไปจะมีผลทำให้ค่าความจุไฟฟ้า และเสถียรภาพของขั้วไฟฟ้ามีแนวโน้มลดลง เนื่องจากเฟอร์ไรต์ที่มีปริมาณมากเกินไปจะทำให้พื้นที่ผิวจำเพาะและขนาดรูพรุนของวัสดุนาโนคอมพอสิตลดลง นอกจากนั้นปริมาณของไอออนของออกซิเจนจะทำให้สมบัติของความจุไฟฟ้าลดลงเนื่องจากความต้านทานของการแพร่ของการส่งผ่านไอออนระหว่างสารละลาย อิเล็กโทรไลต์กับรูพรุนบนขั้วไฟฟ้าเพิ่มขึ้น

สาขาวิชาฟิสิกส์

ปีการศึกษา 2559

ลายมือชื่อนักศึกษา_____

ลายมือชื่ออาจารย์ที่ปรึกษา_____

ลายมือชื่ออาจารย์ที่ปรึกษาร่วม_____

ลายมือชื่ออาจารย์ที่ปรึกษาร่วม_____

ISARA KOTUTHA : SYNTHESIS, CHARACTERIZATION AND
ELECTROCHEMICAL PROPERTIES OF REDUCED GRAPHENE OXIDE/
FERRITE NANOCOMPOSITES. THESIS ADVISOR : PROF.
SANTI MAENSIRI, Ph.D. 113 PP.

REDUCED GRAPHENE OXIDE
/FERRITE/NANOCOMPOSITES/ELECTROCHEMICAL/SUPERCAPACITOR

This research focuses on a simple facile route to prepare a rGO-based nanocomposite through a one-pot hydrothermal approach. Graphite oxide (GO) was prepared from graphite powder by a modified Hummers method. rGO and rGO-based nanocomposites were prepared by a simple facile hydrothermal method. Graphite powder was used as raw material for graphite oxide (GO) preparation with $KMnO_4$ in 98% H_2SO_4. A characteristic peak of graphite at 26.8 °C with $0.33\,nm$ of d-spacing was shifted to 10.70 °C with $0.83\,nm$ d-spacing. GO powder was used as the precursor for $0.5\,mg/ml$ graphene oxide solution by dispersion GO powder in DI water with ultrasonication for $30\,min$. Reduced graphene oxide (rGO) was synthesized by reduction of graphene oxide using hydrazine monohydrate ($H_4N_2 \cdot H_2O$) as a reducing agent at 200 °C for $24\,h$. The formation of rGO could be confirmed by XRD, TEM and Raman spectroscopy. After reduction, A characteristic peak of rGO was shown as amophous carbon due to the random orientation of rGO sheet at $25.5°$. Experimentals, $Fe(NO_3)_3 \cdot 9H_2O$, $Mn(NO_3)_2 \cdot 6H_2O$ and , $Co(NO_3)_2 \cdot 6H_2O$ were used as the precursors for the preparation of rGO-based nanocomposites. The formation of rGO-based nanocomposites was confirmed by XRD, TEM, FTIR, and Raman spectroscopy. The specific surface area of the prepared composite performed by BET analysis was lower than that of pure rGO but higher than that pure ferrite. Consequently, the electrochemical performance was investigated by using the three-electrode cell system within $6.0\,M\,KOH$. The results showed that the specific capacitances were obtained to be 190.3, 276.94, 144.5 and $203.5\,F/g$ at a scan rate of $10\,mV/s$, 194.9, 274.6, 134.4 and $223.1\,F/g$ at a current density of $5.0\,A/g$ for rGO, rGO/MFO05, rGO/MFO10, and rGO/CFO05

spectroscopy. The specific surface area of the prepared nanocomposites performed by BET analysis was lower than that of pure rGO but higher than that of pure ferrite. Consequently, the electrochemical performance was investigated by using the three-electrode cell system within 6.0 M KOH. The results showed the high specific capacitances of 190.3, 276.9, 144.5, and 203.5 F/g at a scan rate of 10 mV/s, 194.9, 274.6, 134.4 and 223.1 F/g at a current density of 5.0 A/g for the rGO, rGO/MFO05, rGO/MFO10, and rGO/CFO05 nanocomposites, respectively. These results suggest that composite of ferrite nanoparticles onto rGO nanosheet can improve the capacitive behavior of the fabricated electrode, but the electrochemical properties are also reduced when the ferrite concentration ratio is high, because of the decreases of specific surface area, mean pore size, and large number of oxygen-containing groups on the working electrode, and the increase of diffusion resistance towards the transfer of ions into the electrode pores.
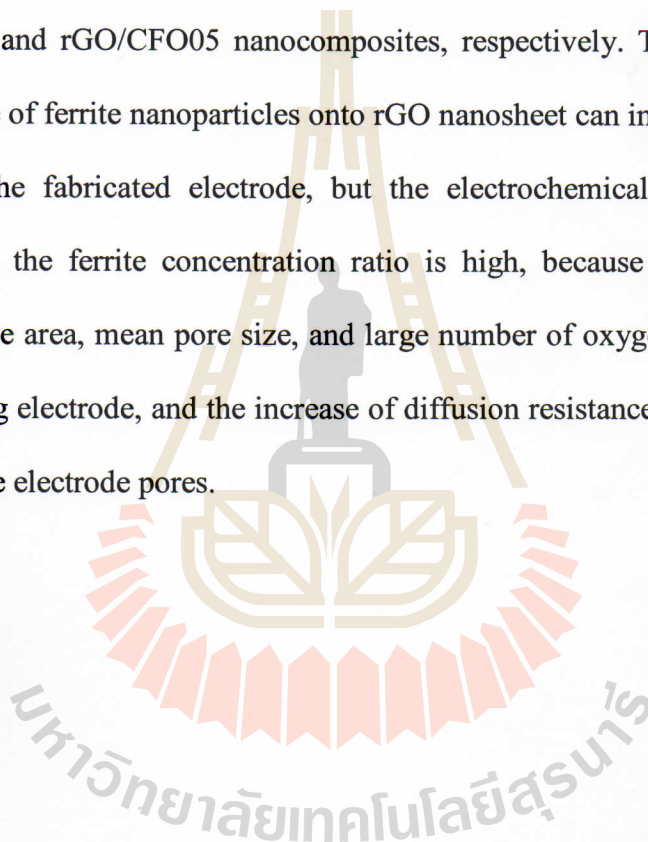
School of Physics   Student's Signature_____

Academic Year 2016   Advisor's Signature_____

                                  Co-advisor's Signature_____

                                  Co-advisor's Signature_____

ACKNOWLEDGEMENTS

CONTENTS

CONTENTS (Continued)

CONTENTS (Continued)

LIST OF TABLES

LIST OF FIGURES

LIST OF FIGURES (Continued)

LIST OF ABBREVIATIONS

GO	Graphite oxide
rGO	Reduced graphene oxide
$rGO/MnFe_2O_4$	rGO nanocomposite with $MnFe_2O_4$ nanoparticles
$rGO/CoFe_2O_4$	rGO nanocomposite with $CoFe_2O_4$ nanoparticles
rGO/MFO05	$rGO/MnFe_2O_4$ of $0.5\,mmol$ $MnFe_2O_4$
rGO/MFO10	$rGO/MnFe_2O_4$ of $1.0\,mmol$ $MnFe_2O_4$
rGO/CFO05	$rGO/CoFe_2O_4$ of $0.5\,mmol$ $CoFe_2O_4$
ESS	Energy storage system
ESR	Equivalent system resistance or effective series resistance
EDR	Equivalent distributed resistance
CPE, Q1	The constant phase element for the electrode interfacial impedance
R_{ct}	Faradaic resistance or charge transfer resistance
Z_{im}, Z'	Imaginary part of impedance
Z_{re}, Z''	Real part of impedance
ΔV	Potential window
Δt	Discharge time
i	Current density
CV	Cyclic voltammetry
GCD	Galvanostatic charge-discharge
HOPG	Highly oriented pyrolytic graphite
HEC	Hybrid electrochemical capacitor
EDLC	Electrochemical double layer capacitance
μ	Carrier mobility

LIST OF ABBREVIATIONS (Continued)

Y	Young's modulus
K	Thermal conductivity
DL	Double layer
E_g	Band gap energy
I_D	$D-\text{peak}$ intensity
I_G	$G-\text{peak}$ intensity
I_D/I_G	A fraction of the intesity of Dp and Gp obtained from Raman spectroscopy
SSA	Specific surface area
CVD	Chemical vapor deposition method
P	Power density
E	Energy density
ε_0	The vacuum permittivity
ε_r	The relative permittivity

CHAPTER I

INTRODUCTION

1.1 Principle and reason

Graphene was first discovered in 2004 (Novoselov et al., 2004). It is a single layer
of carbon atoms in 2D honeycomb structure with extremely interesting properties such as
electronic, mechanical, optical, and thermal properties (An et al., 2010). Graphene has
the highest surface area of $300 - 900 \, \mathrm{m^2/g}$ and a broad pore size distribution of about
$2 - 200 \, \mathrm{nm}$ (J. Li et al., 2006). Graphene and graphene-based nanocomposites play an im-
portant role in the development of electrochemical capacitor or supercapacitor. Reduced
graphene oxide (rGO) is graphene nanosheet which can be functionalized by remaining
epoxy and hydroxyl groups (G. Shao et al., 2012). rGO can be prepared from reduction
of graphite oxide (GO) and has been achieved via the modified Hummers method (Hum-
mers Jr and Offeman, 1958). There are many kinds of reducing agents used for preparation
of rGO such as hydrazine (Gao, Alemany, Ci and Ajayan, 2009; D. Li, Mueller, Gilje,
Kaner and Wallace, 2008), hydroquinone (W. Chen and Yan, 2010), sodium borohydride
($\mathrm{NaBH_4}$) (Shin et al., 2009) , or ascorbic acid (X. Zhu et al., 2012).

Nowaday, the demand of energy requirement increases dramatically. One of the
demanding devices with ultra-high power density ($10^{-3} - 10^{-4} \, \mathrm{W/g}$), fast charging, and
exceptionally long cycling life ($> 100,000$ cycles) (Dai et al., 2011) is supercapacitor

(G. Wang, Zhang and Zhang, 2012). Recently, various porous carbon materials with high specific surface area, such as activated carbons, carbon nanotubes, have been widely used as supercapacitor electrodes, because of their stable physicochemical properties, good conductivity, low cost, and long cycle life. (Béguin, Presser, Balducci and Frackowiak, 2014; Simon and Gogotsi, 2008). rGO is one of carbon materials having high surface area, high electrical conductivity, and good electrochemical stability (X. Huang, Zeng, Fan, Liu and Zhang, 2012; C. Liu, Li, Ma and Cheng, 2010). However, the re-stacking of the rGO layer during fabrication of the electrode, results in a decrease of electrochemical properties due to the decrease of its specific surface area. To overcome this problem, the introduction of graphene-based nanocomposites (Chakrabarti et al., 2013; X.-m. Chen, Wu, Jiang, Wang and Chen, 2011; Stankovich et al., 2006a) by decoration metal (Jagannadham, 2012), or metal oxide (Jiang et al., 2012) onto rGO nanasheet has been received much attention. Metal ferrite material is another material that can be used to prevent rGO nanosheet from re-stacking. It has high theoretical capacity but has poor electrical conductivity and electrode induced by large volume change between charge-discharge processes (M. Zhang, Jia, Jin, Wen and Chen, 2013). Thus, metal ferrite material is alone not suitable for using as electrochemical electrodes.

To improve the high cycling stability and high rate capability of metal ferrite for novel electrodes with high performance, decoration of metal ferrite onto rGO sheets has been investigated. Recently, Tang et al. (Tang, Gao, Xing, Tian and Bao, 2014) reported the preparation of $rGO/MnFe_2O_4$ and $rGO/CoFe_2O_4$ nanocomposite by a one-pot low-temperature process by coprecipitation of Mn and Co ions produced in the modified Hummer's method and in situ reduction of GO at $90\,°C$. In this work, $FeCl_3$ and $MnCl_2 \cdot 4H_2O$ were used as starting materials for preparation of $MnFe_2O_4$ and $rGO/MnFe_2O_4$ nanocom-

posite. Coprecipitation route was separately carried out for preparation of $MnFe_2O_4$ nanoparticles. The $rGO/MnFe_2O_4$ nanocomposite exhibited excellent electrochemical performance, retaining a reversible capacity of $581.2\,mA \cdot h/g$, about 70% of the theoretical capacity, at a specific current of $1\,A/g$ after 200 cycles.

In the present study, a simple facile route to prepare a $rGO/MnFe_2O_4$ and $rGO/CoFe_2O_4$ nanocomposite is carried out through a one-pot hydrothermal approach using GO, $Mn(NO_3)_2 \cdot 6H_2O$, $Co(NO_3)_2 \cdot 6H_2O$, and $Fe(NO_3)_3 \cdot 9H_2O$ as starting materials. The $rGO/MnFe_2O_4$ and $rGO/CoFe_2O_4$ nanocomposites were synthesized with different ratio under the similar quantity of rGO precursor, and the resulting products were characterized by X-ray diffraction (XRD), Raman spectroscopy (Raman), and transmission electron microscopy (TEM). The effect of $MnFe_2O_4$ and $CoFe_2O_4$ nanoparticles concentration on the electrochemical properties of $rGO/MnFe_2O_4$ and $rGO/CoFe_2O_4$ nanocomposites was investigated under the long charge-discharge process upto 1000 cycles

1.2 Objectives of the thesis

1.2.1 To synthesize rGO-based nanocomposites reinforced with metal oxide by the one-pot hydrothermal method.

1.2.2 To characterize the microstructure and phase composition of the synthesized rGO-based nanocomposites.

1.2.3 To study the electrochemical properties of the synthesized rGO-based nanocomposites by using cyclic voltammetry (CV), galvanostatic charge - discharge (GCD), and electrochemical impedance spectroscopy (EIS) technique.

1.3　Limitation of the study

1.3.1 Synthesis of GO, rGO, and rGO-based nanocomposites reinforced with metal oxide.

1.3.2 Study of microstructure and phase composition of the synthesized materials by using the XRD, and TEM techniques.

1.3.3 Study of reflectance of the synthesized rGO-based nanocomposites by using FTIR techniques.

1.3.4 Study the electrochemical properties of the synthesized rGO-based nanocomposites.

1.4　Location of research

1.4.1 Advanced Materials Physics Laboratory (AMP), School of Physics, Institute of Science, Suranaree University of Technology (SUT), Nakhon Ratchasima, 30000 Thailand.

1.4.2 The Center for Scientific and Technological Equipment (SUT), Suranaree University of Technology (SUT), Nakhon Ratchasima, 30000 Thailand.

1.4.3 Department of Physics, Faculty of Science, Khon Kaen University, Khon Kaen, 40002 Thailand.

1.4.4 Faculty of Science, Chiang Mai University, Amphur Muang, Chiang Mai, 50200 Thailand.

1.5 Anticipated outcomes

1.5.1 Knowhow of synthesis of rGO-based nanocomposites with excellent electrochemical properties.

1.5.2 Understanding of the effec of ferrite nanoparticles on the electrochemical properties of rGO–based nanocomposites.

1.5.3 International publications (ISI).

1.6 Thesis structure

This thesis is divided into five chapters. Chapter I is the introduction of the project. Review of literature is presented in Chapter II, including the background of graphene, supercapacitor, electrode materials, and electrolyte. The preparation, physical and electrochemical properties characterization of all the samples are presented in Chapter III. And then, the results obtained in this research and discussions of the results are given in Chapter IV. Finally, conclusions and suggestions are described in Chapter V, and future works are proposed in this chapter too.

CHAPTER II

LITERATURE REVIEW

This chapter presents a review of the background of graphene and graphene-based nanocomposites, basic properties, synthesis and characterization. Moreover, an application of graphene and graphene-based nanocomposite as raw material for fabrication of supeca-pacitor electrode, one type of energy storage system (ESSs), is reviewed.

2.1 Graphene

Graphene, which was discovered in 2004 (Novoselov et al., 2004), is an atomically thin sheet of carbon arranged in a two dimensional honeycomb crystal. It was surprising when graphene was first observed. Graphene has an intrinsic roughness and can be wrapped up into 0D fullerenes, rolled into 1D nanotubes or stacked into 3D graphite as shown in Figure 2.1 (Geim and Novoselov, 2007) and its morphology has been shown in Figure 2.2 (Thakur and Karak, 2012).
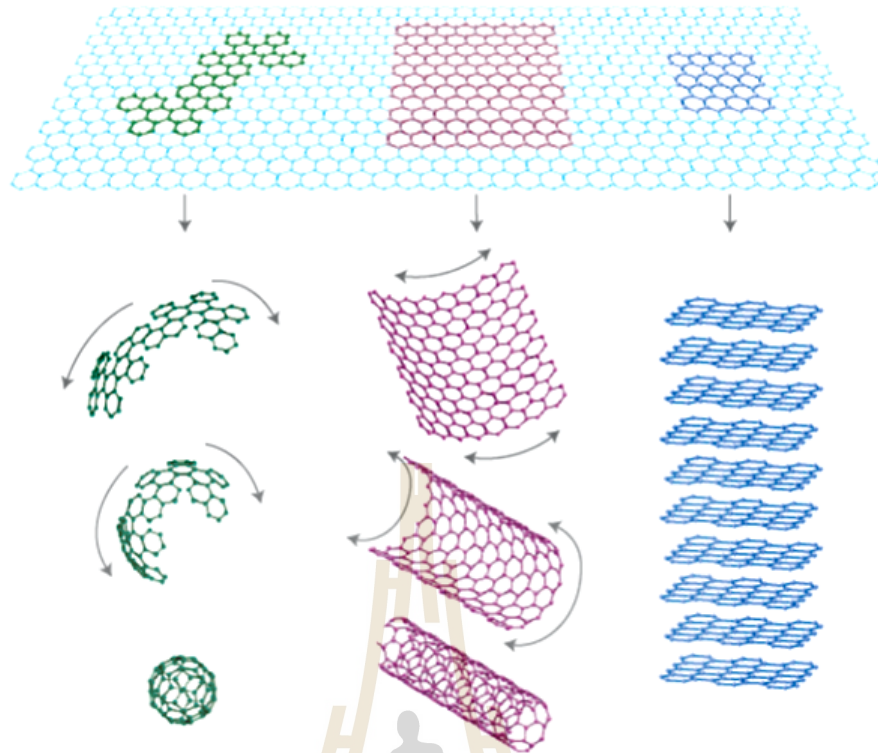
Figure 2.1 Graphene structure. Graphene is a 2D building material for carbon materials of all other dimensionalities. It can be wrapped up into 0D buckyballs, rolled into 1D nanotubes or stacked into 3D graphite (Geim and Novoselov, 2007).
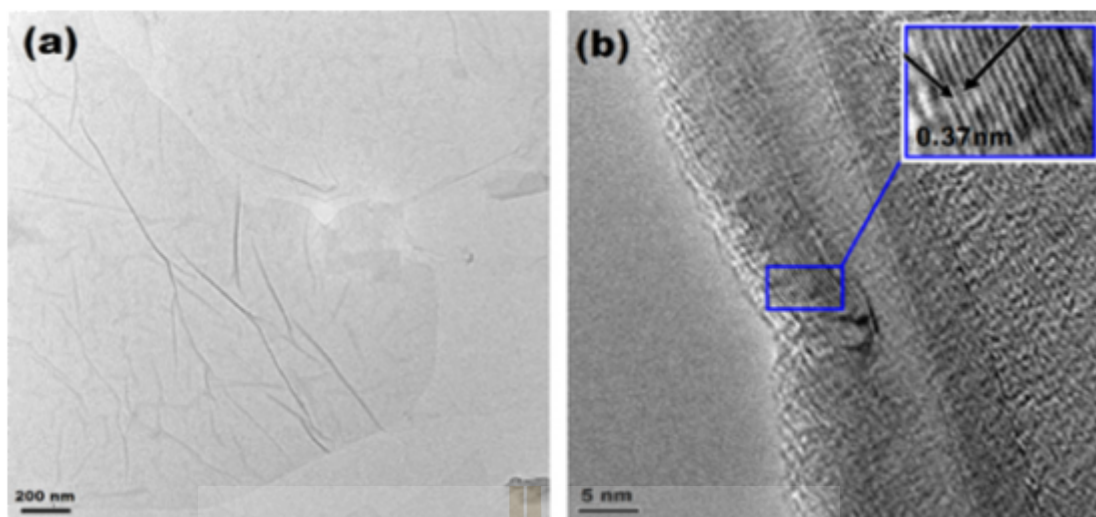
Figure 2.2 HRTEM images of rGO at different resolution (a) 200 nm and (b) 5 nm. (Thakur and Karak, 2012)

In the recent years, graphene is an exciting material. It has a large specific surface area ($2630\,\mathrm{m^2/g}$) (Cai et al., 2008), high electric carrier mobility of $200\,000\,\mathrm{cm^2/V \cdot s}$ (Bolotin et al., 2008), high Young's modulus of about $1.0\,\mathrm{TPa}$ (Lee, Wei, Kysar and Hone, 2008) and thermal conductivity in the range $\sim 4840\,\mathrm{W/m \cdot K}$ to $\sim 5300\,\mathrm{W/m \cdot K}$ (Balandin et al., 2008), and its optical transmittance of $\sim 97.7\%$ and good electrical conductivity merit attention for applications such as for transparent conductive electrodes (Cai, Zhu, Li, Piner and Ruoff, 2009)

2.1.1 Graphene preparations

There are many methods which have been developed to prepare graphene. In 2004, Geim and his coworkers (Novoselov et al., 2004) reported the graphene nanosheets prepared by mechanical exfoliation of highly oriented pyrolytic graphite (HOPG), which is called scotch-tape method. Although, this method is still widely used in many laboratories to prepare grapheme for basic scientific studying and for making basic devices base on graphene, it is not suitable for mass production. Therefore, the other methods for synthe-

sis graphene have been considered. For electronics applications, graphene has also been prepared by chemical vapor deposition method (CVD) growth on some of metal substrates e.g., Ni (Y. Huang et al., 2010; Kim et al., 2009), and Cu (X. Li et al., 2011) or by substrate-free CVD (C. Liu et al., 2010) as shown in Figure 2.3, which is a potential mass-production method. Another mass-production method is chemical reduction (Dai et al., 2011; Pei and Cheng, 2012), and thermal reduction (S. Chen, Zhu, Wu, Han and Wang, 2010; H. Wang and Hu, 2011) of graphite oxide (GO).
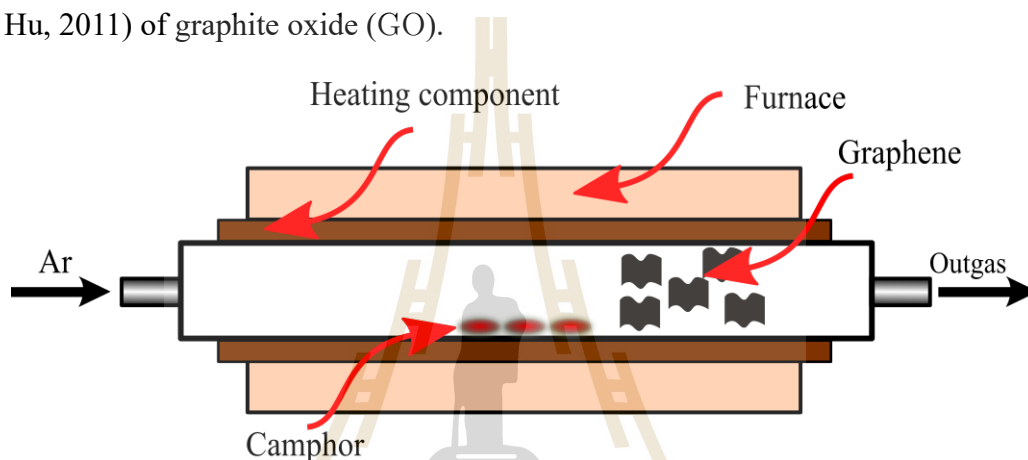
Figure 2.3 Experimental scheme of substrate-free synthesis of graphene film (adapted from C. Liu et al., 2010).

2.1.2 Graphite Oxide and reduced Graphene Oxide

Graphite oxide (GO) (Gómez-Navarro et al., 2007) is a layered material produced by the oxidation of graphite using concentrate acids as an oxidants (Hummers Jr and Offeman, 1958; Park and Ruoff, 2009) with $\mathrm{C}:\mathrm{O}$ atomic ratio of $2.0-2.9$ and the interlayer spacing ranging from $0.6-1.1$ nm depending on preparation procedure. GO behaves as an insulator because it contains oxygen-containing groups, hydroxyl $(\mathrm{C-OH})$, and epoxy $(\mathrm{C-O})$ groups on their basal planes, and carboxyl $(\mathrm{C=O})$ groups located at the sheet edges. The presence of these functional groups makes graphite oxide sheets strongly hydrophilic, which allows graphite oxide can be dispersed in water (Stankovich et al., 2006b).
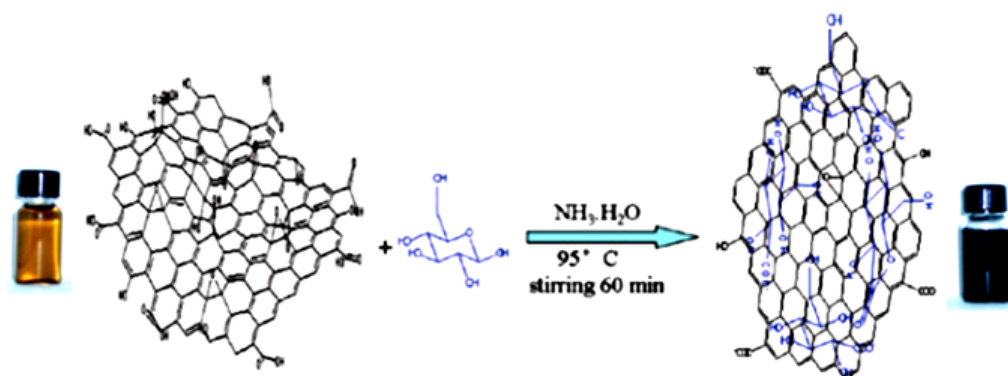
Figure 2.4 Illustration of the preparation of rGO based on glucose reduction (C. Zhu
et al., 2010).

Reduced graphene oxide (rGO) is a product of reduction of GO by using reducing agents. The electrical transport in rGO occurs when the electron hops over varying distances between nonoxidized graphene islands, therefore rGO can exhibit as the conductor (Gómez-Navarro et al., 2007).

Chemical reduction of graphite oxide (GO) as shown in Figure 2.4 is the procedure to prepare graphene in large quantities. GO is ultrasonicated in DI water to form a homogeneous colloidal dispersion of graphene oxide. rGO with properties similar to that of graphene nanosheet (GNS) is prepared by chemical, thermal, or electrochemical reduction of exfoliated graphite oxide. The reducing agents that are used for reducing aqueous dispersions of graphene oxide are hydrazine monohydrate (Z. Fan et al., 2012; Z.-J. Fan et al., 2010), $NaBH_4$ (Shin et al., 2009), hydroxylamine (Zhou et al., 2011) glucose (X.-H. Li, Kurasch, Kaiser and Antonietti, 2012), and ascorbic acid (Vitamin-C) (J. Zhu and He, 2012) as shown in Table 2.1.

Table 2.1 Reduced graphene oxide preparation by different reducing agents.

Reduction Method	C/O ratio	References
Hydrazine hydrate	10.3	Stankovich et al., 2007
Vitamin C	12.5	Wang et al., 2008
Hydrazine monohydrate	12.5	Wang et al., 2008
150 mM $NaBH_4$	8.6	Shin et al., 2009
Hydrazine vapor	~ 8.8	Yang et al., 2009
$NaBH_4$ solution	8.57	Gao et al., 2009
55% HI	> 14.9	Pei et al., 2010
Glucose	N/A	Zhu et al., 2010

2.2 Supercapacitors

The increasing cost of fuels, pollution, global warming and geopolitical concerns are among the problems connected with the dependence of modern societies on fossil fuels. Reducing these issues is an increasingly important goal that can be achieved through developing other energy sources and storage technologies. As a result, recently there has been a growing interest in high power and high energy density storage systems. A more wide- spread use of renewable sources and a better efficiency of transportation systems are two important goals to be pursued to overcome this problem.

Energy storage systems (ESSs) are the key to deal with the intermittent nature of renewable energy sources and increase the power transmitted into the grid from systems

such as wind and solar power. In addition, an increase in the efficiency of a vehicle requires kinetic energy to be stored somewhere whenever the vehicle slows down or stops. Although these operations have been successfully performed with batteries on a low-power scale, new methods for efficiency enhancement will require large amounts of power that can only be provided by other energy storage technologies such as supercapacitors. These have attracted significant attention due to their high power capabilities and long cycle-life, giving a very good chance to build more advanced hybrid ESSs, for both on-board and stationary applications.

Supercapacitors are devices capable of managing high power rates compared to batteries. Although supercapacitors provide hundred to many thousand times higher power in the same volume (Simon and Gogotsi, 2008), they are notable to store the same amount of charge as batteries do, which is usually $3-30$ times lower (Simon and Gogotsi, 2008). This makes supercapacitors suitable for those applications in which power bursts are needed, but high energy storage capacity is not required. Supercapacitors can also be included within a battery-based ESSs to decouple the power and energy characteristics of the ESSs, thus improving the sizing while fulfilling the power and energy requirements, and probably enlarging its lifetime. The power output of supercapacitors is lower than that of electrolytic capacitors, but can reach about 10 kW/kg.

Supercapacitors have high power capabilities, fast charged propagation within seconds and can be charged-discharged. They have very long cyclic life (usually greater than $100,000$ cycles), require low maintenance, and exhibit low self-discharging (K. Zhang, Zhang, Zhao and Wu, 2010); they have larger energy densities when compared to conventional capacitors, although, energy densities are lower than batteries and fuel cells (K. Zhang et al., 2010). For these advantages of thess devices, they are passive and static electrical

energy storage devices, utilized in applications such as portable electronics devices, memory back-up systems, and hybrid cars, where extremely fast charging is a valuable feature (Yan, Wei, Shao et al., 2010; K. Zhang et al., 2010).

On the other hand, their specific energy is several orders of magnitude higher than the one of capacitors (Pandolfo and Hollenkamp, 2006). These devices are interesting because they fill the gap between aluminum electrolytic capacitors and batteries, which are capable of storing large amounts of energy, but do not offer very high power densities (< 1 kW/kg) due to their storage mechanism. This can be graphically explained in a Ragone plot, in which the energy and power densities are represented in horizontal and vertical axes, also showing the discharge time of the devices in diagonal lines ($E = Pt$). Different storage technologies are represented in a Ragone plot in Figure 2.5. However, the Ragone plot does not reflect many other performance parameters such as cost, safety and cycle life. They need to be mentioned separately for a complete understanding of advantages and limitations of a particular energy storage technology. Thus, it is extremely important to note that supercapacitors can not only be discharged in a matter of seconds, but also be charged in such a short time period. This is an important benefit for energy recovery systems, e.g. for dynamic braking of transport systems. Table 2.2 shows comparation of supercapacitors with capacitors and batteries.
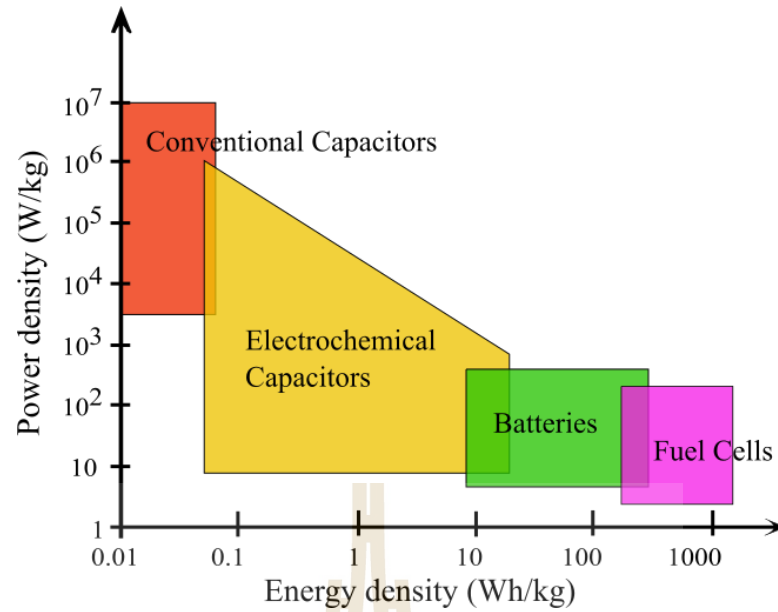
Figure 2.5 Sketch of Ragone plot for various energy storage and conversion devices. The indicated areas are rough guide lines (adapted from Kötz and Carlen, 2000).

Table 2.2 Comparation of supercapacitors with capacitors and batteries. (adapted from Kötz and Carlen, 2000).

Characteristics	Capacitor	Supercapacitor	Battery
Specific energy (W $\cdot$ h/kg)	< 0.1	$1 - 10$	$10 - 100$
Specific power (W/kg)	$\gg 10,000$	$500 - 10,000$	< 1000
Discharge time	$10^{-6} - 10^{-3}$	s to min	$0.3 - 3$ h
Charge time	$10^{-6} - 10^{-3}$	s to min	15 h
Coulombic efficiency (%)	About 100	$85 - 98$	$70 - 85$
Cycle-life	Almost infinite	$\gg 500,000$	About 1000

Another great advantage of supercapacitors is their cycle life. These devices can

withstand millions of cycles thanks to their charge storage mechanism, which does not involve irreversible chemical reactions, storing charges physically at the surface of the electrodes in an electric double layer. This allows exceeding the cycle life of batteries, which are at best capable of withstanding a few thousand cycles. The highly reversible electrostatic storage does not produce changes in the electrode volume, eliminating the swelling occurring in typical redox reactions in the bulk of a battery's active material during charge and discharge cycles. A supercapacitor electrode has no such rate limitations as those of redox battery electrodes due to electrochemical kinetics through a polarization resistance (Kötz and Carlen, 2000). The main disadvantage related to the charge storage mechanism is the operating voltage of a supercapacitor cell, which should be kept low in order to avoid the chemical decomposition of electrolytes. Table 2.3 compares the main differences in the properties of batteries and supercapacitors.

Table 2.3 Comparison between batteries and supercapacitors properties (Miller and Simon, 2008).

Comparison parametr	Battery	Supercapacitor
Storage mechanism	Chemical	Physical
Power limitation	Reaction kinetic, mass, transport	Electrolyte conductivity
Energy storage	High (bulk)	Limited (surface area)
Charge rate Kinetically	limited	High same as discharge
Cycle life limitations	Mechanical stability, chemical reversibility	Side reaction

2.3 Supercapacitors classification

Depending on the charge-storage mechanisms, capacitors can be classified into two types: electrochemical double layer capacitors (EDLCs) and faradaic pseudocapacitor as shown in Figure 2.6. The descriptions of which are explained in the following section.
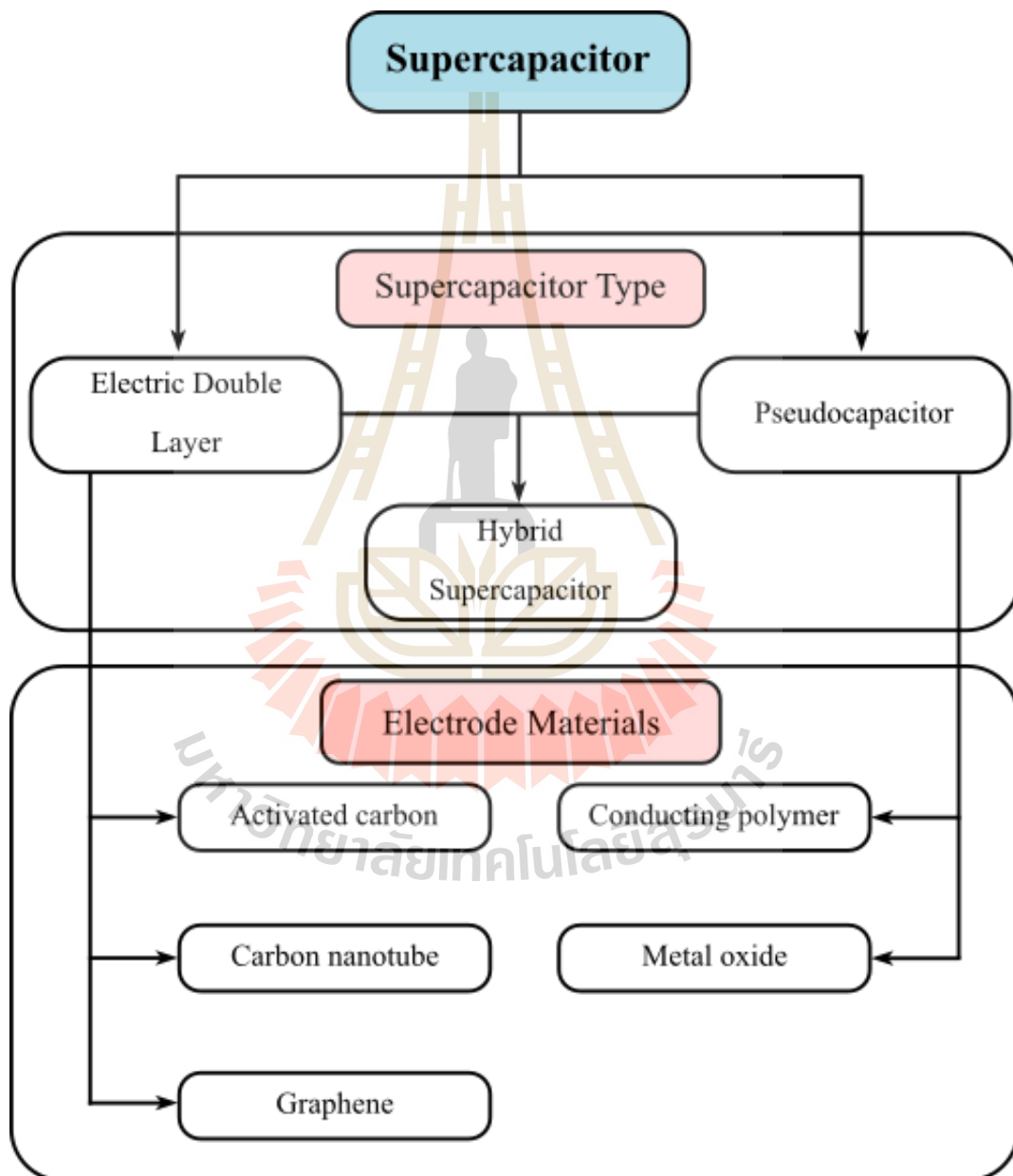
Figure 2.6 Classification of different supercapacitors (adapted from González et al., 2016).

2.3.1 Electrochemical double layer capacitors (EDLCs)

Electrochemical double layer capacitors (EDLCs) can store the electric charge directly across the layer of both electrode (Danaee, Jafarian, Forouzandeh, Gobal and Mahjani, 2009). Because there is no charge transfer across the interface, this is a true capacitance effect. Figure 2.7 shows a schematic of EDLCs charge storage mechanism. The electric charge is generated on the electrode surface and can be enumerated as: surface dissociation, ion adsorption from solution, and crystal lattice defect. The capacitance arises from an electrochemical DL directly analogous to a parallel plate capacitor. As an excess or deficiency of charge builds up on the electrode surface, ions of the opposite charge build up in the electrolyte near the electrode/electrolyte interface in order to provide electroneutrality. The thickness of the DL depends on the concentration of the electrolyte and the size of ions, which is in the order of $5 - 10$ Å for concentrated electrolytes. The capacitance of the EDLC as shown in Figure 2.8 is about $10 - 20$ mF/cm^2 for a smooth electrode in concentrated electrolyte solution and can be estimated according to equation (2.1)
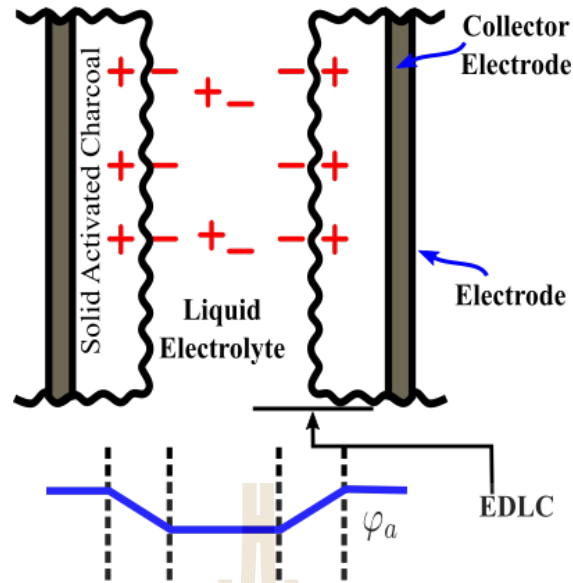
(a) Potential at non-charge
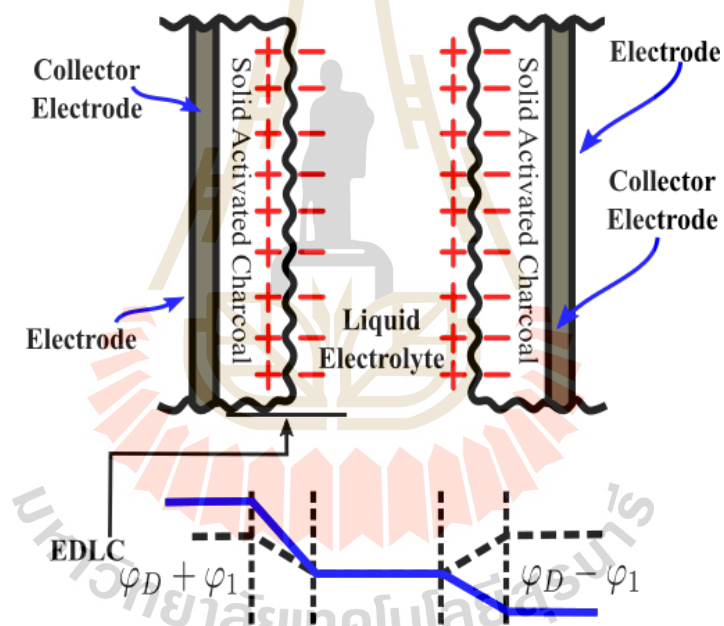
(b) Potential at charge

Figure 2.7 EDLC charge storage mechanism.

$$C = \varepsilon_0 \varepsilon_r \frac{A}{d} \qquad (2.1)$$

where ε_0 is the dielectric constant of vacuum, ε_r is the electrolyte dielectric constant, which is assumed as 10 for the water in the DL (Kötz and Carlen, 2000), d is the

thickness of the double layer, which is the charge separation distance, and A is the surface area of each electrode.
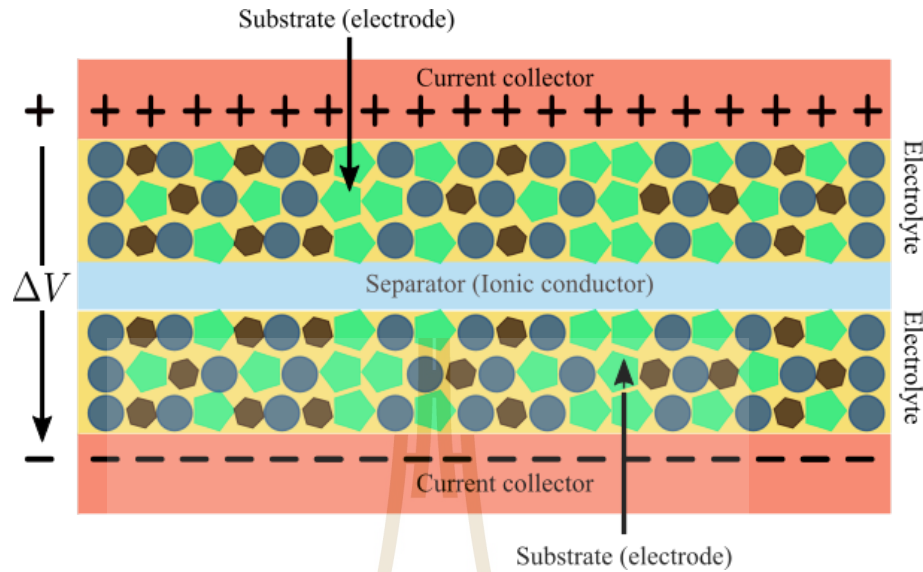
Figure 2.8 Symmetric supercapacitor schematic diagram (adapted from González et al., 2016).

The corresponding electric field in the electrochemical DL is as high as 10^6 V/cm. Eqn. (2.2) can be used to calculate the capacitance for a symmetrical capacitor.

$$\frac{1}{C_{cell}} = \frac{1}{C_1} + \frac{1}{C_2} \tag{2.2}$$

where C_1 and C_2 represent the capacitance of the first and second electrodes (Pandolfo and Hollenkamp, 2006)

The capacitance of a double layer capacitor is in the range of 5 and $20\,\mu\text{F}/\text{cm}^2$ depending on the electrolyte used (Pandolfo and Hollenkamp, 2006). Although, the specific capacitance used aqueous alkaline and acid solutions is generally higher than in organic electrolyte, organic electrolytes are more widely used. The organic electrolyte can sustain a higher operation voltage. For the symmetric double layer capacitor, their operation voltage

can be up to $2.7\,\mathrm{V}$ and they can store more energy, which is propotional to the square of voltage according to

$$E = \frac{1}{2}CV^2 \qquad (2.3)$$

where E is the energy density of the double layer capacitor, C is the capacitance, and V is the voltage across the capacitor.

The maximum power P_{max} that a supercapacitor is able to deliver, depends on the voltage and the internal resistance R as follows

$$P_{max} = \frac{V^2}{4R} \qquad (2.4)$$

There is no faradaic or redox reaction at EDLC electrode. Therefore, there is no effect from the electrochemical kinetics through a polarization resistance. The storage mechanism of double layer capacitor is on the surface of the electrode, so it consume very short time for charge or discharge process with high power performance. For battery, there is faradaic reaction between solid and electrolyte. This can limit the battery life with a few thousand cycles of charge-discharge process, but for EDLC, it can sustain millions of cycles.

Considering to the electrode with a small amount of pore size, the electrode surface with pores wider than $2\,\mathrm{nm}$ (mesopore) and micropores, the capacitance can be investigated with difference condition. For carbon electrode with mesopores (mesoporous carbon) with cylindrical pores, the capacitance can be calculated by the traditional model according to (J. Huang, Sumpter and Meunier, 2008)

$$C = \varepsilon_0 \varepsilon_r \frac{A}{b \ln\left(\frac{b}{b-d}\right)} \tag{2.5}$$

where b is the pore radius of carbon electrode, and d is the distance between ion and carbon electrode

For microporous carbon electrode, the ion could be fully desolvated, because ionic radius is close to the bare ion size. Therefore, the capacitance is calculated from (J. Huang et al., 2008)

$$C = \varepsilon_0 \varepsilon_r \frac{A}{b \ln\left(\frac{b}{a_0}\right)} \tag{2.6}$$

where b is the effective size of the ion.

Feng et. al. (Feng, Qiao, Huang, Sumpter and Meunier, 2010) shows that, the more relativistic approximation of carbon's pore shape is not in cylindrical pore, but it is a narrow slit. Therefore, the capacitance model can be shown as

$$C = \varepsilon_0 \varepsilon_r \frac{A}{b - a_0} \tag{2.7}$$

For the realistic capacitor test, the constant current tests are performed to determine the main characteristics of devices. The parameters that have to consider when calculate the capacitance of the capacitor consist of the equivalent system resistance (ESR), which is the resistance associate to the cell and the equivalent distributed resistance (EDR), which represents the resistance in the electrode's pores. These are calculated using the notation in Figure 2.9 with the following expressions:
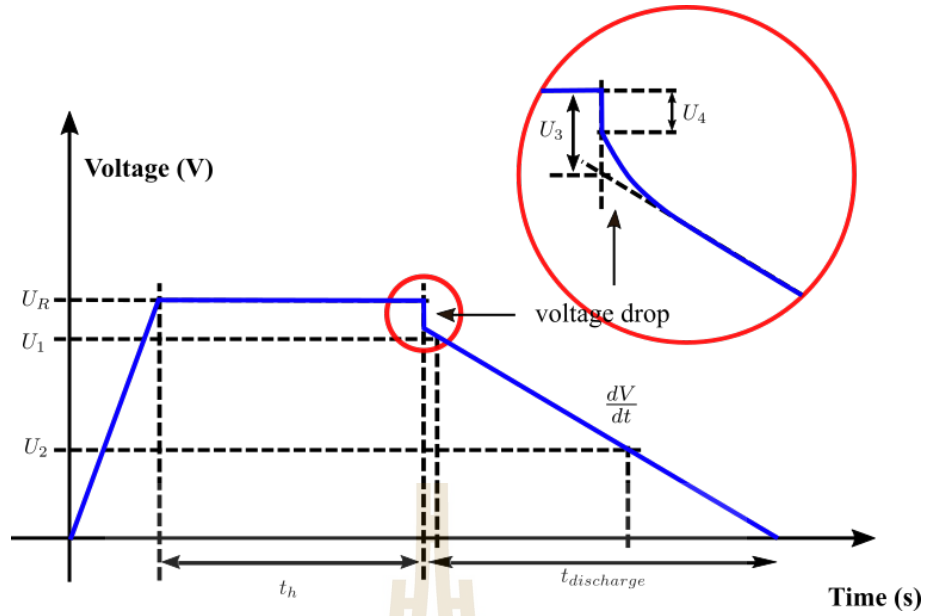
Figure 2.9 Constant current discharge supercapacitor cell test (adapted from González et al., 2016).

Also the current (I) across the supercapacitor will be

$$I = C\frac{dV}{dt} \tag{2.8}$$

where dV/dt is a slope of the curve during discharge process. Therefore, for the capacitance, ESR and EDR can be caculated from

$$C = \frac{(I_{discharge} t_{discharge})}{(U_1 - U_2)} \tag{2.9}$$

$$ESR = \frac{U_4}{I_{discharge}} \tag{2.10}$$

$$EDR = \frac{U_3}{I_{discharge}} \tag{2.11}$$

The electrical properties of a supercapacitor are mainly determined by components such as electrode materials, electrolytes, separators and current collectors. Electrode fabrication is made through coating a metallic current collector with an about $100\,\mu\text{m}$ thin layer of high surface area material. This active material is mixed with a binder so as to form slurry. The thickness of the slurry should be controlled for making the coated layer of active material sufficiently thin to be conductive throughout the material. Since the ESR of supercapacitor cells must be very low, special attention must be paid to the contact resistance between the active material and the current collector. The surface of current collectors should be treated before coating it with active materials. Surface treatments decrease the Ohmic drop at the current collector/active material interface (Portet, Taberna, Simon and Laberty-Robert, 2004). For supercapacitors designed to work with organic electrolytes, treated aluminum foils or grid current collectors are used. Using nanostructured current collectors with increased contact area is a way to control the current collector/active material interface (Gogotsi, 2011).

2.3.2 Pseudocapacitance

Pseudocapacitors is one of electrochemical capacitor, which arises on electrodes when the application of a potential induces faradaic current from reactions such as electrosorption or from the oxidation–reduction of electroactive materials such as, RuO_2, IrO_2, and Co_3O_4. The first process is electrosorption, which is occurs when chemisorption of electron donating anion such as Cl^-, B^-, I^-, or CNS^- as following equation

$$M + A^- \longleftrightarrow MA^{(1-\delta)} + \delta e^- \tag{2.12}$$
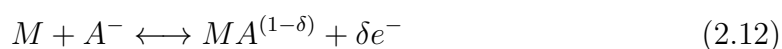
The electrosorption reaction of A^- anions occurs on the surface of an electrode with the quantity δe^- are related to the so-called valence electrosorption.

The second process of pseudocapacitor is an oxidation-reduction reactions, which is an exchange of charge across the DL, rather than a static separation of charge across a finite distance. The reaction indicated as

$$O_{ad} + ne^- \longrightarrow R_{ed} \tag{2.13}$$

The charge, ne^-, is exchanged in this reaction, and resulting the indirect and analogous energy storage to a battery.

The supercapacitor system concludes both of the two different storage mechanisms of EDLC and pseudocapacitance are, Generally, it was well known that one of the storage mechanisms occupies the leading position, and the other is relatively weak.

2.3.3 Hybrid electrochemical capacitors

In recent years, several types of an asymmetrical configuration capacitor, which so-called hybrid electrochemical capacitors (HECs). These type of the capacitors consisting of a DL carbon material and a pseudocapacitance material, have attracted significant attention (Kisacikoglu, Uzunoglu and Alam, 2009). Most of the HECs developed to date have used pseudocapacitive materials as the cathode.

The pseudocapacitance electrodes accumulate charge through redox reaction so-called faradic electrochemical process. This process can not only increase the specific capacitance of the capacitor, but also extends the working voltage of the energy storage mechanism. For the conventional EC, the working potential ranges from 0.8 to $2.7\,\mathrm{V}$ vs. $\mathrm{Li/L^+}$, whereas the potential range of an advanced HEC at the cathode is extended to the whole potential window of activated carbon (AC), specifically from 1.5 to $4.5\,\mathrm{V}$ vs. $\mathrm{Li/Li^+}$, which is wider potential range than the conventional EC.

2.4   Electrode materials

The well known materials used as supercapacitor electrode consist of three types, carbon-based materials, metal oxides, and conducting polymers.

2.4.1   Carbon based materials

Carbon-based materials are low cost materials and widely used in many applications. They can play very closely to ideal capacitor with nearly rectagular shape of cyclic voltammogram as shown in Figure 2.10 which presents cyclicvoltammograms for carbon materials in both, aqueous (Figure 2.10a) and organic electrolytes (Figure 2.10b).
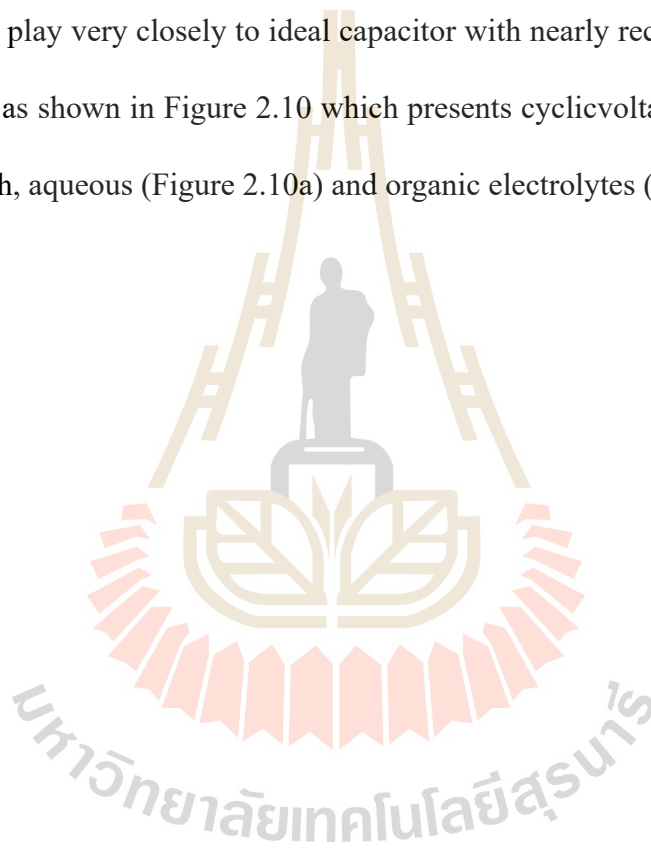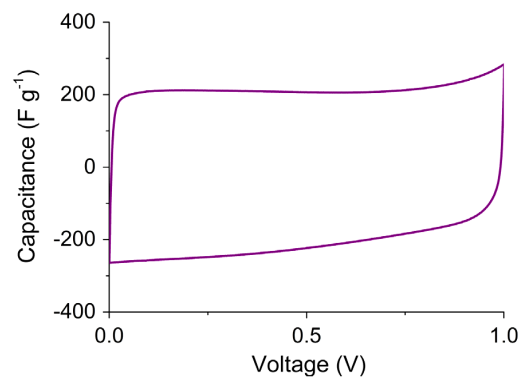
(a) Aqueous 6 MKOH
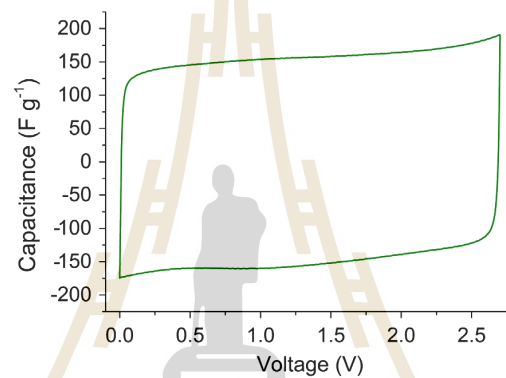
(b) Organic 1 M tetraethylammonium tetrafluoroborate electrolytes

Figure 2.10 Cyclic voltammogram of an EDLC cell at 5 mV/s in various electolytes

(González et al., 2016).

2.4.1.1   Activated carbon

Activated carbon is very low cost and has high surface area, and thus this material is the most widely used to fabricate the supercapacitors electrodes (Simon and Gogotsi, 2008). Activated carbon with high porosity can be prepared by carbonization process using heat treatment of carbon-rich organic precursors such as coconut shell wood, fossil fuels and their derivetives (pitch, coal or coke), and polymer under inert atmosphere (Simon and Gogotsi, 2008). The specific surface area of the different activated carbon precursors are shown in Table 2.4

Table 2.4 BET specific surface areas of different carbon precursors (adapted from Wei and Yushin, 2012).

Carbon precursor	Activation method	S_{BET} (m²/g)	Specific capacitance (F/g)
Furfurol	Steam	1040	111
Coconut shell	KOH	1660	79
Eucalyptus wood	KOH	2970	236
Fir wood	Steam	1130	142
Bamboo	KOH	1290	35
Cellulose	KOH	2460	185
Potato starch	KOH	2340	335
Starch	KOH	1510	194
Sucrose	CO_2	2100	163
Beer lees	KOH	3560	188
Banana fiber	$ZnCl_2$	1100	74
Corn grain	KOH	3200	257
Sugar cane bagasse	$ZnCl_2$	1790	300
Apricot shell	NaOH	2335	339
Sun flower seed shell	KOH	2510	311
Coffee ground	$ZnCl_2$	1020	368
Wheat straw	KOH	2316	251
Fish scale		2270	168

2.4.1.2 Carbon nanotubes (CNT)

Carbon nanotube (CNT) is one of carbon structure with fully accessible external surface area and high electric conductivity. It consists of two nanostructures, single walled carbon nanotubes (SWCNTs) and multi-walled carbon nanotubes (MWCNTs), depending on the diffrence of the catalytic decomposition of certain hydrocarbons. The different nanostructures of CNT formations depend on the manipulating different parameters. The purity and the morphology of the CNT can contol its specific capacitance. The surface of CNT electrodes is mainly mesoporous, associated to the external face of the tubes. Because of its high specific surface area and good electrical conductivity, this material can be developed to increase the specific capacitance by tuning the distance between tubes. Moreover, CNT has very high stability specific capacitace retaintion, it can be widely used in energy storage system application.

2.4.1.3 Graphene

Today the electrochemical energy storage devices are becoming less appropriate for the ever increasing range of high demand applications. The enegry storage technology becomes increasingly more advanced and powerful the requirements of the increasing of the energy storage systems. In order to produce energy storage devices that can sufficiently support demands of consumers are the exploration and exploitation of new electrode materials. One of new materials for energy storage system production is graphene, which is extremely attractive for energy storage applications due to its unique reported properties (L. L. Zhang, Zhou and Zhao, 2010).

A supercapacitor unit cell is usually comprised of two porous carbon electrodes that are isolated from electrical contact by a porous separator, the current collectors of metal

foil or carbon impregnated polymers are used to conduct electrical current from each electrode (Stoller and Ruoff, 2010). The separator and the electrodes are impregnated with an electrolyte, this allows ionic current to flow between the electrodes whilst preventing electronic current from discharging the cell (Stoller and Ruoff, 2010). In supercapacitors, energy is stored due to the formation of an electrical double layer at the interface of the electrode (electrical double layer capacitors) (Du, Guo, Song and Chen, 2010) or due to electron transfer between the electrolyte and the electrode through fast Faradiac redox reactions (pseudocapacitors) (Vivekchand, Rout, Subrahmanyam, Govindaraj and Rao, 2008), often the capacitance of a supercapacitor is dependent on its ability to utilise both of the previous energy storage capabilities with high efficiency, where these two mechanisms can function simultaneously depending on the nature of the electrode material (L. L. Zhang et al., 2010). To develop a supercapacitor device, an active electrode material with high capacity performance is indispensable (Yan, Wei, Shao et al., 2010), however, all of the components are important factors. Current research on electrochemical capacitors is aimed at increasing both power and energy densities as well as lowering fabrication costs - whilst using environmentally friendly materials. The core materials studied for supercapacitor electrodes are carbons, metal oxides, and conducting polymers (D.-W. Wang et al., 2009), with recent advancements having focused on CNTs. However, graphene-based materials have shown immense theoretical and practical advantages, such as a high surface area, excellent conductivity and capacitance, and relatively low production costs (mass production). The use of graphene as a supercapacitor material has been widely reported, with many studies reporting graphene as a far superior supercapacitor material than existing carbon and polymer based materials. According to the energy-storage mechanisms noted above, the key to enhancing specific capacitance is to enlarge the specific surface area and control the pore size,

layer stacking, and distribution of the electrode material, thus Du et al. (Du et al., 2010) investigated graphene as a potential electrode material. The authors reported mass-produced GNSs with a narrow mesopore distribution of ~ 4 nm from natural graphite via oxidation and rapid heating processes, and found the GNSs to maintain a stable specific capacitance of 150 F/g under the specific current of 0.1 A/g for 500 cycles of charge-discharge (Du et al., 2010). Wang et al. (Y. Wang et al., 2009) also investigated graphene as a potential supercapacitor electrode material, where a maximum specific capacitance of 205 F/g was measured with a power density of 10 kW/kg at an energy density of 28.5 W $\cdot$ h/kg, and excellent cyclic ability was obtained also with $\sim 90\%$ specific capacitance remaining after 1200 cycles. Interestingly, other work (Y. Chen, Zhang, Yu and Ma, 2010) has shown that using an electrophoretic deposition method to deposit GNSs onto nickel foams with three-dimensional porous structures; the high specific capacitance of 164 F/g is obtained from cyclic voltammetry (CV) measurement at a scan rate of 10 mV/s, and it was noted that after 4700 cycles the specific capacitance remains 61% of the maximum capacitance, work encompassing the deposition of silver nanoparticles onto graphene sheets has shown that increased specific capacitance and improved charge transfer occur with evidence of a reduced resistance. Yet further exciting prospects emerge when considering work by Vivekchand et al (Vivekchand et al., 2008). who have shown graphene prepared via graphitic oxide whilst utilising an ionic liquid, thus enabling the operating voltage to be extended up to 3.5 V, exhibits a specific capacitance and energy density of ~ 75 F/g and 31.9 W $\cdot$ h/kg respectively, surpassing those of both SWCNT and MWCNTs, 64 and 14 F/g respectively; the authors claim that the energy density is one of the highest values reported to-date of this kind, inferring that the performance characteristics of graphene are directly related to its quality in terms of numbers of graphene layers and the inherent sur-

face area. It is likely however that the highest energy value claimed in this case will most probably be surpassed in coming months given the intense research in this area. These comparable results suggest potential for GNS based electrochemical capacitors to be fabricated, but scalability might be an issue. However, it is evident that the general specific capacitance of graphene is not as high as expected, and thus it is notable that many researchers have turned to the incorporation and fabrication of graphene based hybrid materials in the pursuit for improved capacitance performance. Wang et al. (D.-W. Wang et al., 2009) report a novel high performance electrode material based upon fibrillar polyaniline (PANI) doped with graphene oxide sheets. The authors obtained a nanocomposite with a mass ratio of PANI/graphene, $100 : 1$, which exhibited a high specific capacitance of $531\,\mathrm{F/g}$, obtained by charge-discharge analysis, and when compared to individual PANI ($216\,\mathrm{F/g}$) it was clear that doping (and the ratio of graphene oxide) has a profound effect on the electrochemical capacitance performance of nanocomposites; graphene exhibits great potential for application in supercapacitors and other power source systems of the future.

Having overviewed the application of graphene as a supercapacitor, it is clear that it has already made a significant impact and revealed itself to be a promising material for future research within this area. With the possibility of hybrid graphene materials emerging in the near future, we may witness the fabrication of a supercapacitor composite that is able to acquire currently unachievable capacitance levels and greatly improved cyclic abilities; of course a major limitation is the current cost of graphene, reproducibility, scalability, and characterisation, where drawing from the latter many reports are emerging where claims of the utilisation of graphene aremadewithout adequate characterization being performed and in such cases perhaps graphene is not present, rather multiple layer or greater – thus appropriate control experiments need to be performed where results are compared to other

appropriate carbon forms such as graphite or activated carbons. This is an issue evident throughout each aspect of graphene's utilization within energy related applications, and consequently should be borne-in-mind when considering each topic covered below.

2.4.2 Metal oxides

Metal oxides have high specific capacitance and conductivity. Therefore, they are suitable to use as electrode materials for high energy and high power supercapacitors (Sharma and Bhatti, 2010). The widely used metal oxide in supercapacitor application are RuO_2 (Ahn, Song, Jo, Park and Kim, 2006; Patake, Lokhande and Joo, 2009), IrO_2 (Hu, Huang and Chang, 2002), MnO_2 (Yan, Wei, Cheng, Fan and Zhang, 2010; Yu, Zhai, Liu and Li, 2016), NiO (Nelson and Owen, 2003; Patil, Salunkhe, Gurav and Lokhande, 2008), Co_3O_4 (Kandalkar, Dhawale, Kim and Lokhande, 2010; Kandalkar, Gunjakar and Lokhande, 2008), NiO (Hu, Huang and Chang, 2008; Lai et al., 2012), and MoO (Babakhani and Ivey, 2010; Nakayama, Tanaka, Sato, Tonosaki and Ogura, 2005). Table 2.5 summarizes potential metal oxide materials used for electrode materials in supercapacitors.

Table 2.5 Summary of metal oxide materials of electrode material investigation.

Electrode material	Electrolyte	Working voltage (V)	Specific capacitance (F/g)
RuO$_2$ (Ahn et al., 2006)	0.5 M H$_2$SO$_4$	1.2	534
RuO$_2$ (Patake et al., 2009)	0.5 M H$_2$SO$_4$	1.2	650
MnO$_2$ (Yan, Wei, Cheng et al., 2010)	2.0 mol/l (NH$_4$)$_2$SO$_4$	1.0	241
Co$_3$O$_4$ (Kandalkar et al., 2008)	1.0 M KOH	1.0	165
Ni(OH)$_2$	3% KOH	0.8	578
Mo$_2$N/Ta$_2$O$_5$	3.5 mol/l H$_2$SO$_4$	0.8	106
MnFe$_2$O$_4$ (Kuo and Wu, 2007)	1.0 M LiPF$_6$ +EC/EMC	2.5	126
NiO (Lao et al., 2006)	2.0 M KCl	0.7	262

2.4.3 Conductive polymers

Polymers electrodes have high electric conductivity, upto 104 S/cm for doped polyacetylene, high electroactivity, which is the ability of an electrode coated with a polymer film to reversibly change its oxidation-reduction state in a solution under the applica-

tion of an external electric field, the ability to form passive layers on metal surfaces, and the semiconductor band structure. Table 2.6 summarizes conductive polymers used for electrode materials in supercapacitor applications.

Table 2.6 Summary of conductive polymer materials of electrode material investigation.

Electrode material	Electrolyte	Working voltage (V)	Specific capacitance (F/g)
Poly(3-methylthiophene) (Ahn et al., 2006)	$PYR_{14}TFSI$	3.6	25
Poly(3-methylthiophene) /MnO_2 (Patake et al., 2009)	$1.0\,mol/l\,Na_2SO_4$	1.0	381
PANI/MNO_2 (Yan, Wei, Cheng et al., 2010)	$0.1\,M\,Na_2SO_4$	1.2	715
PANI/AC (Kandalkar et al., 2008)	$6\,M\,KOH$	0.9	588

The typical cyclic voltammogram of a polymer electrode is not rectangular, as expected for a capacitor, but exhibits a current peak at redox potential of the polymer, while metal oxide electrode scan exhibits a series of redox reactions, giving an almost rectangular cyclic voltammogram shape. Regarding charge and discharge kinetics studied by cyclicvoltammetry, devices made of these materials are battery-like. As a result the shape of a galvanostatic test is not triangular anymore, as expected for capacitors. Figure 2.11 shows an example of pseudocapacitor cycling along with the shape obtainable from a

supercapacitor.
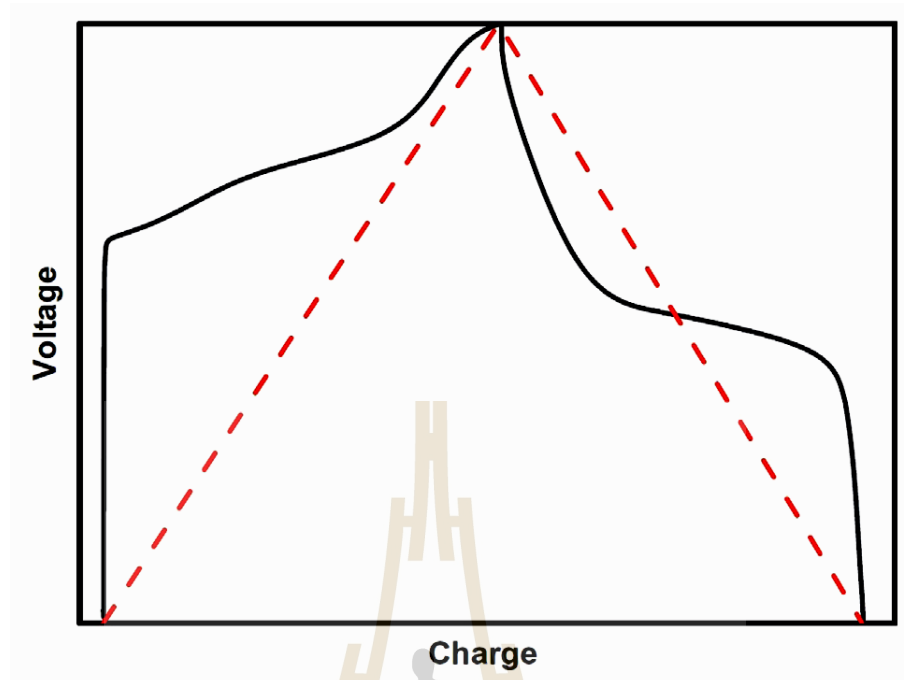
Figure 2.11 Galvanostatic cycling with potential limitation of an ideal pseudocapacitor cell and a cell based on conducting polymers. Cells using conducting polymers in black, ideal pseudocapacitor in dashed red (K. Chen and Xue, 2014).

2.5 Electrolytes

The electrolyte is very important for the supercapacitor performance. Its concentration has to be high so as to avoid depletion problems during the charge of the supercapacitor, especially for organic electrolyte(Pell and Conway, 2001). The performance of a supercapacitor cell will be decreased, if the electrolyte reservoir is too small as compared to the large electrode surface the performance of a supercapacitor cell. The normally sufficient concentration of electrolyte are higher than $0.2\,\mathrm{M}$ (Kötz and Carlen, 2000).

2.5.1 Aqueous and organic electrolytes

Electrolytes widely used in supercapacitors can be classified as aqueous and organic. Aqueous electrolytes have limited their cell voltage typically to $1\,V$ due to the water decomposition at $1.23\,V$, whereas cells based on organic electrolytes can reach voltages of $2.7\,V$ and higher (G. Wang et al., 2012).

2.5.2 Ionic electrolytes

Ionic liquids (ILs) are resistant to the reduction and the oxidation in a wide voltage potential window, which depends on the counter ion, providing a cell voltage of around 4.5 volt, with some of them being able to reach $6\,V$ (Galiński, Lewandowski and Stępniak, 2006). Since ILs are solvent free, as shown in Figure 2.12, there is no solvation shell, therefore the ion size is better known (Largeot et al., 2008). The most important properties of ionic liquids from the point of view of the electrochemistry are, conductivity, viscosity, and the potential range of electrochemical stability. The main draw back of ILs electrolytes is their low electrical conductivity, which is typically less than $10\,mS/cm$ (Galiński et al., 2006), and is significantly lower compared to aqueous electrolytes. The conductivity of ionic liquids is strongly correlated to their viscosity, with strong temperature dependence (H. Liu, Liu and Li, 2010). In order to overcome the low conductivity, a dilution with organic solvents is sometimes applied (G. Wang et al., 2012). Some ILs have a reasonably good ionic conductivity, comparable to the best organic solvent electrolytes (H. Liu et al., 2010).

CONVENTIONAL IONIC SOLUTION   IONIC LIQUID
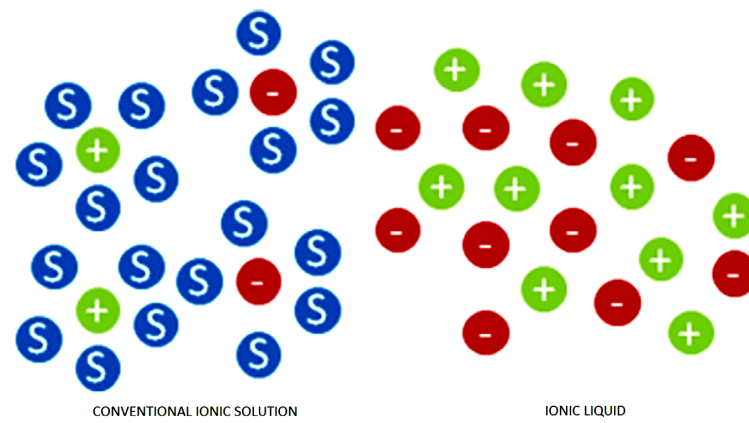
Figure 2.12 Schematic difference between ionic liquids and conventional electrolytes

based on dissolved salts (Díaz et al., 2014).

CHAPTER III

EXPERIMENTAL PROCEDURE

This chapter describes the experimental method for the preparation of rGO-based nanocomposites. GO was synthesized by a modified Hummers method and nanocomposite materials were synthesized by a hydrothermal method. The physical properties of synthesized products were characterized by X-ray diffraction (XRD), Transmission electron microscope (TEM), Fourier transform infrared (FTIR). The Raman spectroscopy, and elecrochemical properties were evaluated by cyclic voltammetry (CV), galvanostatic charge-discharge (GCD), and electrochemical impedance spectroscopy (EIS).

3.1 Powder preparation

3.1.1 Graphite oxide preparation

In this study, GO powder was synthesized by a modified Hummers method, rGO and rGO-based (Co, Mn) nanocomposites were synthesized by a hydrothermal method. The materials used in this research are shown in Table 3.1

Table 3.1 List of raw materials used for rGO-based nanocomposites and working electrodes preparation, quoting their source and purity.

Material	Manufacture	Purity
Graphite powder	Aldrich	99%
Sodium hydroxide (NaOH)	MERCK kGaA	99%
Sodium nitrate (NaNO$_3$)	BDH	99%
Iron (III) nitrate enneahydrate (Fe(NO$_3$)$_3 \cdot$ 9H$_2$O)	Kento chemical	99.9%
Co (II) nitrate hexahydrate (Co(NO$_3$)$_2 \cdot$ 6H$_2$O)	Kento chemical	99.95%
Mn (II) nitrate hexahydrate (Mn(NO$_3$)$_2 \cdot$ 6H$_2$O)	Kento chemical	99.95%
Sulphuric acid (H$_2$SO$_4$)	Ajax	98%
Hydrochloric acid (HCl)	Ajax	36%
Potassium hydroxide (KOH)	Aldrich	90%
Potassium permanganate (KMnO$_4$)	Aldrich	99%
Hydrogen peroxide (H$_2$O$_2$)	Fisher	30%
Poly (vinylidene fluoride) (PVDF)	Aldrich	99%
N-Methyl-2-pyrrolidone (NMP)	Aldrich	99%
Sodium borohydride (NaBH$_4$)	Fluka	99%

3.1.2 Synthesis of graphite oxide (GO)

Graphite oxide (GO) with some of function group as shown in Figure 3.1 was prepared from graphite powder by a modified Hummers method (Hummers Jr and Offeman, 1958) as shown in Figure 3.2. A typical procedure, 5.0 g of graphite powder and 2.5 g of NaNO$_3$ were first added into 115.0 ml of 98% H$_2$SO$_4$. The mixture was then cooled down

in ice-bath under continuous stirring for 0.5 h. After that, 15.0 g of $KMnO_4$ was slowly added at the temperature lower than 10°C. The mixture was removed from the ice-bath and was then continuously stirred at 356 °C for 24 h. Next, 230 ml of de-ionized water was slowly added to dilute the reaction mixture obtained with the temperature lower than 60 °C. The mixture was continuously stirred for 0.5 h and the reaction was maintained at 98 °C for 15 min. After that, it was diluted with 400 ml de-ionized water and stirred until the temperature was about 60 °C. The reaction was terminated by adding 20 ml of 30% H_2O_2, filtered, and washed with 10% HCl. The as-prepared GO was washed and dried for the further application.
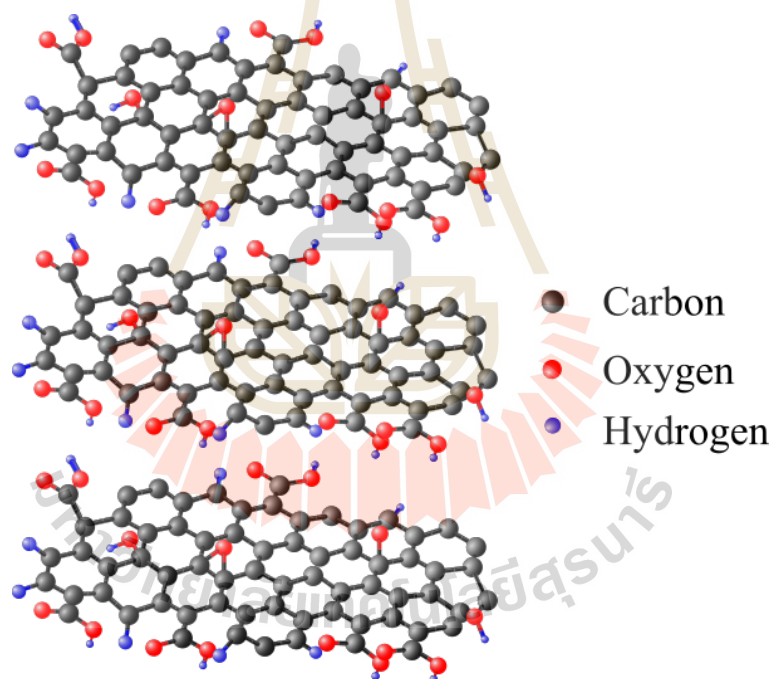
Figure 3.1 Graphite oxide structure (adapted from Joshi et al., 2014).
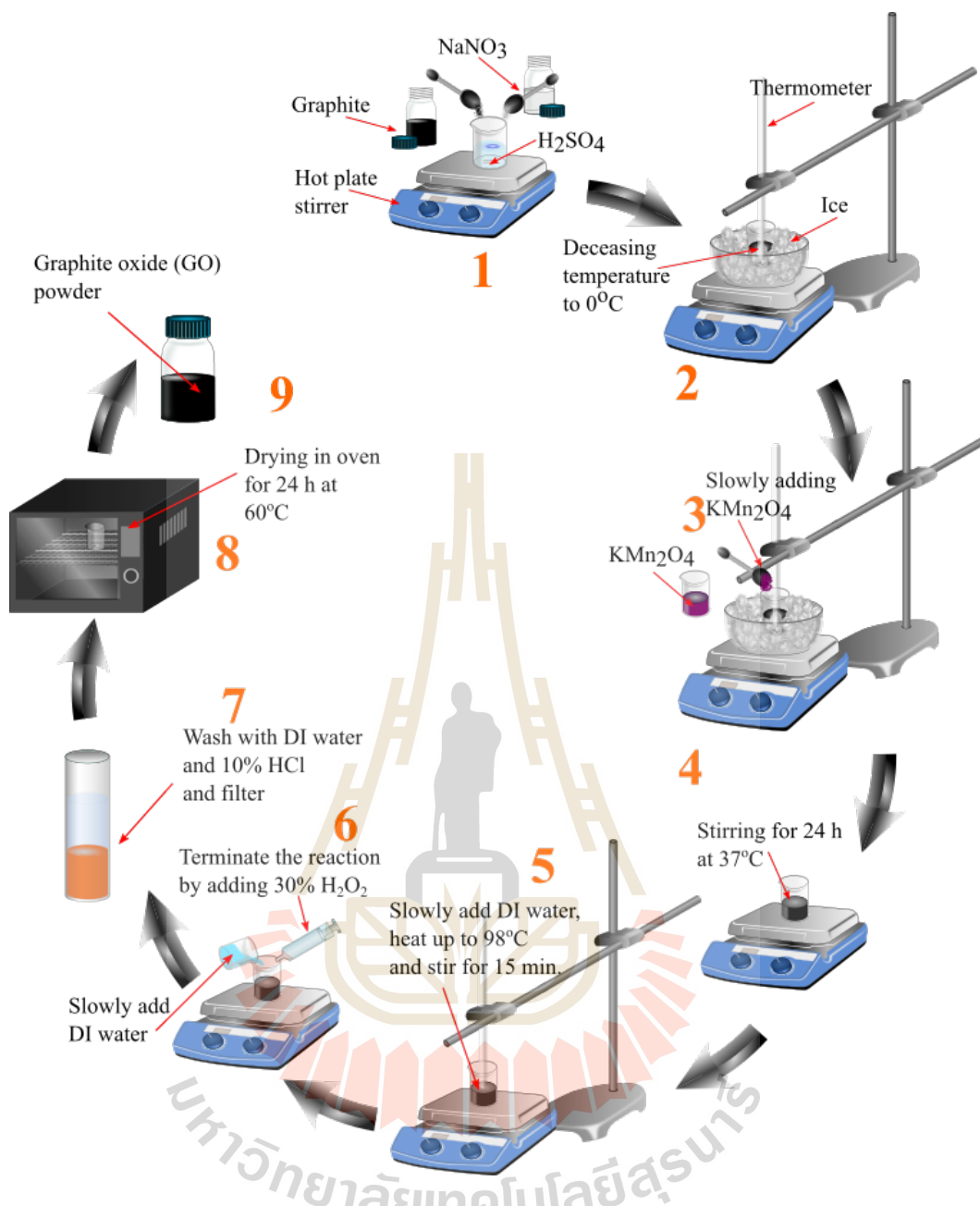
Figure 3.2 A schematic diagram of graphite oxide (GO) preparation.

3.1.3 Synthesis of rGO

rGO as shown in Figure 3.3 was prepared by a one-pot hydrothermal approach as shown in Figure 3.4. GO solution was prepared by dispersion of GO powder in deionized water (DI). Then, $1.0\,\mathrm{M}$ NaOH solution was added to the mixture to control pH value to be about 12 and followed by adding $6.0\,\mathrm{ml}$ of hydrazine monohydrate solution. The obtained mixture was transferred into a Teflon line and the reaction was maintained at

$200\,^{\circ}\mathrm{C}$ for 24 h. Finally, the as-prepared rGO nanosheet was washed and dried for further

characterization and used as a precursor for preparation of rGO-based nanocomposites.
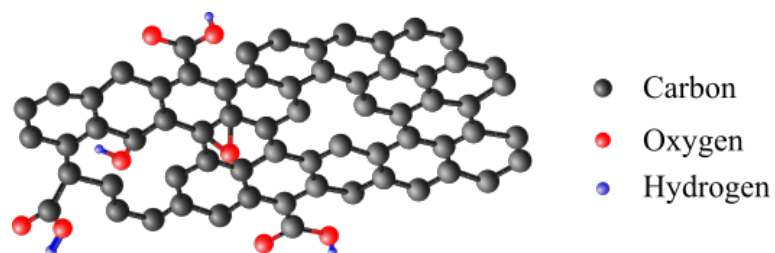
Figure 3.3 Reduced graphene oxide structure (adapted from Joshi et al., 2014).
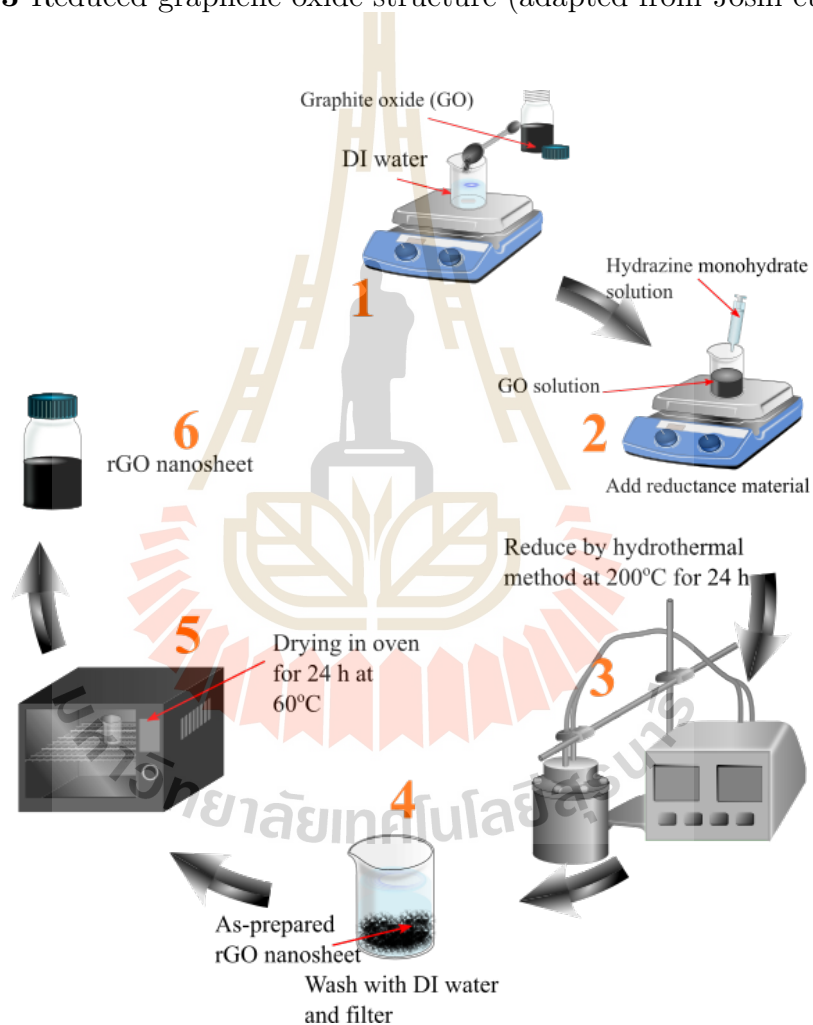
Figure 3.4 A schematic diagram of rGO nanosheet preparation.

3.1.4 Synthesis of rGO/MnFe₂O₄ nanocomposite

$\mathrm{rGO/MnFe_2O_4}$ nanocomposite were prepared by a one-pot hydrothermal approach

as shown in Figure 3.5. Typically, $\mathrm{Fe(NO_3)_3 \cdot 9H_2O}$ and $\mathrm{Mn(NO_3)_2 \cdot 6H_2O}$ with ratio

$1:1$ by mole were dissolved in 20 ml of ethylene glycol (EG) under stirring and followed by adding 3.0 ml of 25% ammonia solution. The mixture was added into 150 ml of 0.5 mg/ml exfoliated GO prepared by dispersion of GO powder in de-ionized water (DI). Then, 1.0 M NaOH solution was added to the mixture to control pH value to be about 12 and followed by adding 6.0 ml of hydrazine monohydrate ($H_4N_2 \cdot H_2O$) solution. The obtained mixture was transferred into a Teflon line and the reaction was maintained at $200\,^\circ$C for 24 h. Finally, the as-prepared rGO/MnFe$_2$O$_4$ nanocomposite was washed and dried for further characterization. The rGO-based nanocomposites were also prepared with different concentrations of MnFe$_2$O$_4$ nanoparticles decorated on rGO nanosheet. rGO and MnFe$_2$O$_4$ were also prepared using the same process except no MnFe$_2$O$_4$ solution was added for the preparation of bare rGO whereas no exfoliated was added for the preparation of bare MnFe$_2$O$_4$ nanoparticles. The abbreviations rGO, rGO/MFO05, and rGO/MFO10 are used for the prepared samples composed of 0.0, 0.5, and 1.0 mmol of MnFe$_2$O$_4$, respectively.
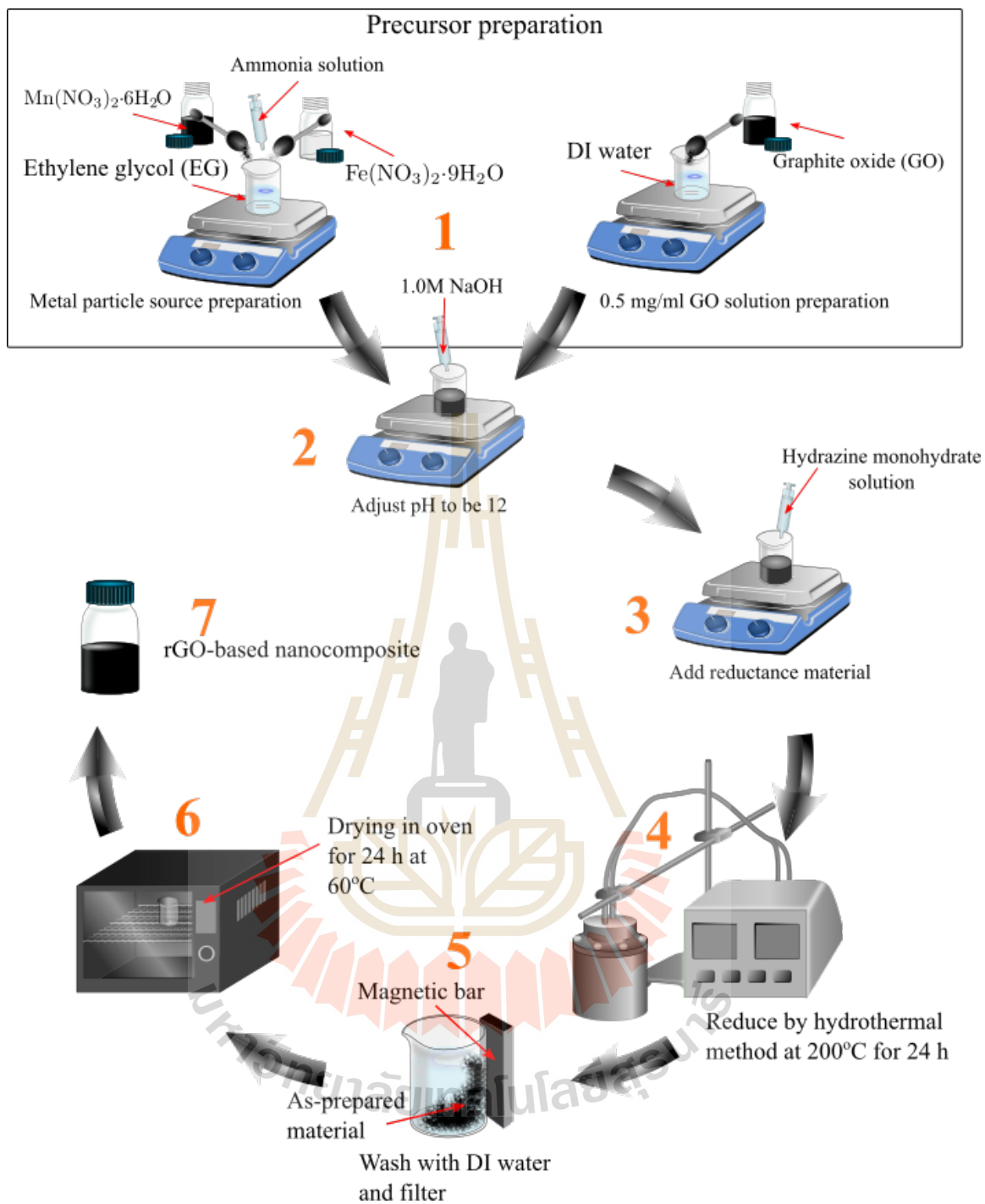
Figure 3.5 A schematic diagram of rGO/MnFe$_2$O$_4$ nanocomposite preparation.

3.1.5 Synthesis of rGO/MnFe$_2$O$_4$ nanocomposite

rGO/CoFe$_2$O$_4$ nanocomposite were prepared by a one-pot hydrothermal approach. Typically, Fe(NO$_3$)$_3 \cdot$ 9H$_2$O and Co(NO$_3$)$_2 \cdot$ 6H$_2$O with ratio 1 : 1 by mole were dissolved in 20 ml of ethylene glycol (EG) under stirring and followed by adding 3.0 ml of 25% ammonia solution. The mixture was added into 150 ml of 0.5 mg/ml exfoliated GO prepared by dispersion of GO powder in de-ionized water (DI). Then, 1.0M NaOH solution was added to the mixture to control pH value to be about 12 and followed by adding 6.0 ml of hydrazine monohydrate solution (NaBH$_4$). The obtained mixture was transferred into a Teflon line and the reaction was maintained at 200 °C for 24 h. Finally, the as-prepared rGO/CoFe$_2$O$_4$ nanocomposite was washed and dried for further characterization. The rGO-based nanocomposites were also prepared with different concentrations of CoFe$_2$O$_4$ nanoparticles decorated on rGO nanosheet. rGO and CoFe$_2$O$_4$ were also prepared using the same process except no rGO/CoFe$_2$O$_4$ solution was added for the preparation of bare rGO whereas no exfoliated was added for the preparation of bare CoFe$_2$O$_4$ nanoparticles. The abbreviations as rGO, and rGO/CFO05 are used for the prepared samples composted of 0.0 and 0.5 mmol of CoFe$_2$O$_4$, respectively.
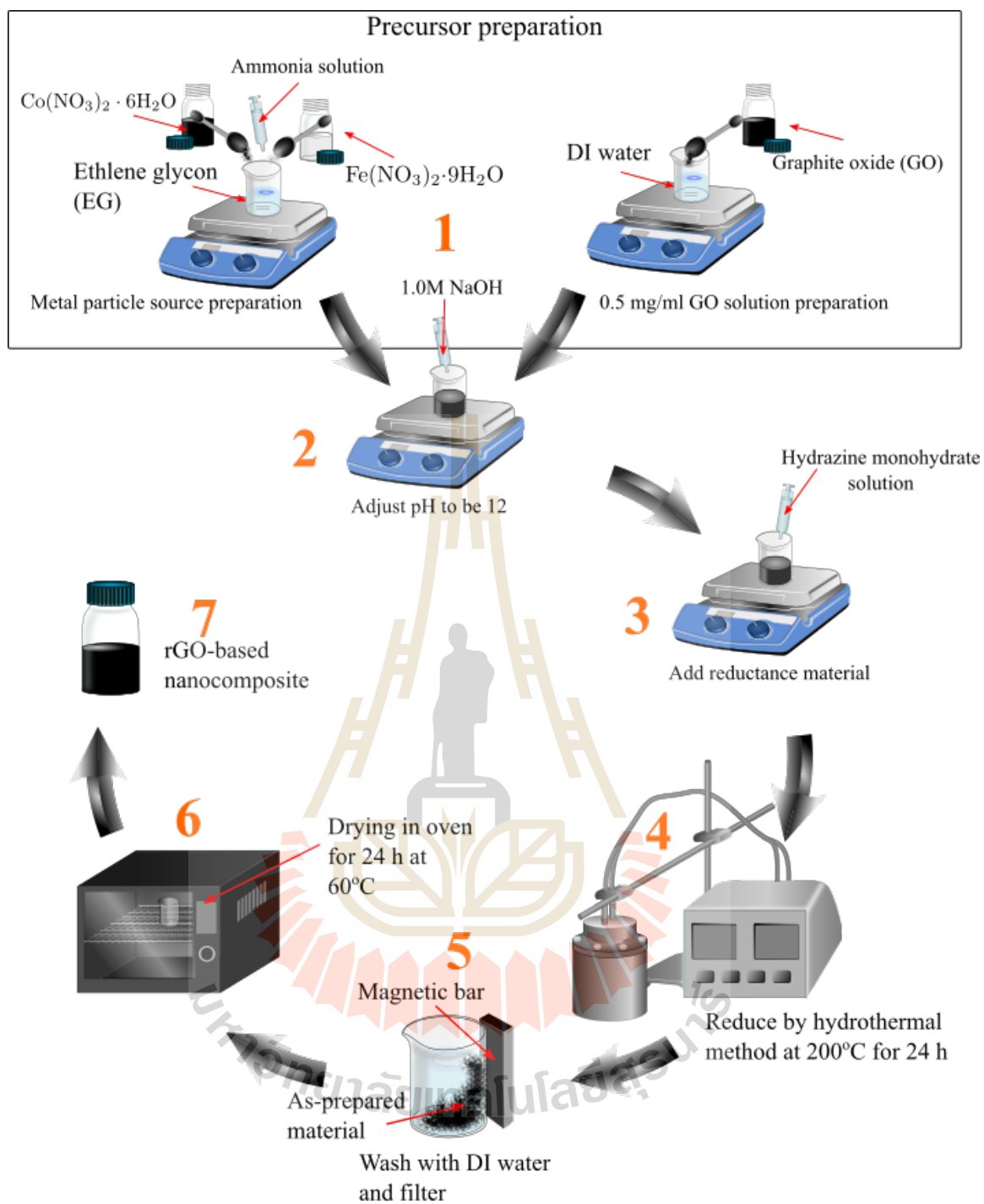
Figure 3.6 A schematic diagram of rGO/CoFe$_2$O$_4$ nanocomposite preparation.

3.2   Physical characterization

Crystallographic structures of as-prepared rGO, rGO-based nanocomposites were characterized by X-ray diffraction (XRD). The functional groups of as-prepared products were investigated by using Fourier transform infrared spectroscopy (FTIR). Raman spectroscopy was used to investigate Raman vibration of as-prepared product, whereas the surface morphology was studied by using (TEM). The specific surface area and pore size distribution of the as-prepared material were investigated by N_2 adsorption-desorption isotherm using Brunauer-Emmett-Teller (BET) and Barrett-Joyner-Halenda (BJH) technique.

3.2.1   X-ray diffraction (XRD)

The prepared GO, rGO, and rGO-based nanocomposites were characterized for identification of a crystallite size by using the XRD using a CuK_α radiation with $\lambda = 0.154060$ nm by using Bruker D2, Germany as shown in Figure 3.7a. In the XRD pattern as shown in Figure 3.7b, a collimated beam of X-ray is incident on a specimen and is diffracted by the crystalline phases in the specimen according to Bragg's law as shown in equation (3.1)
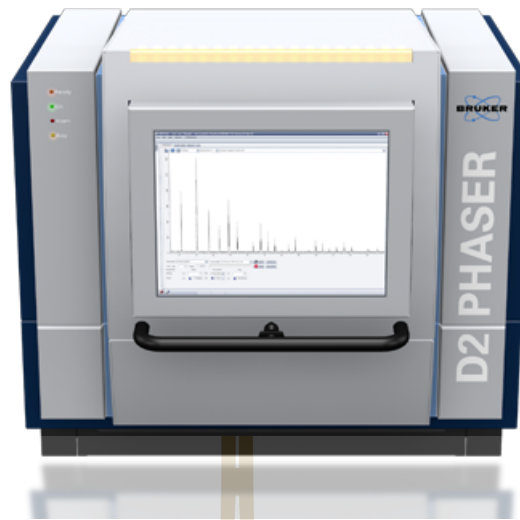
(a) Bruker D2, Germany (D2phaser.com)
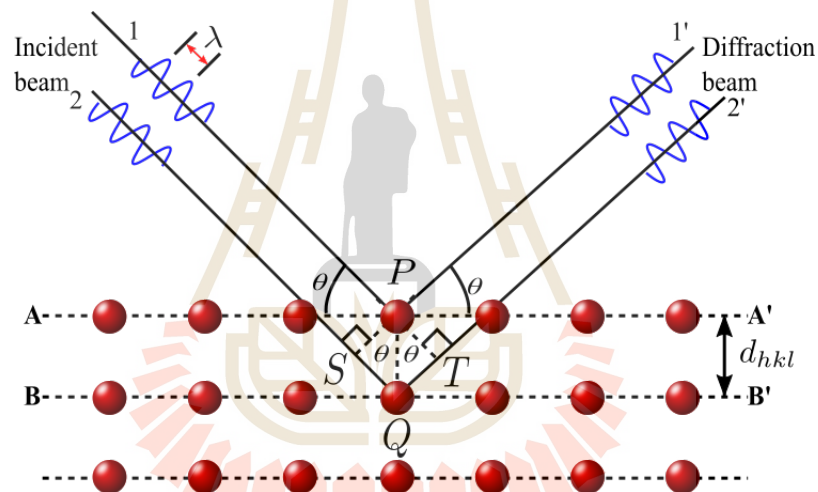
(b) Bragg diffraction by crystal planes (Leng, 2008).

Figure 3.7 XRD pattern study using Bragg's law.

$$2d \sin \theta = n\lambda \qquad (3.1)$$

where, d is the spacing between atomic planes in the crystal phase, n is a positive

integer, λ is the wavelength of the X-ray radiation, and θ is the diffraction angle of incident

beam made with the crystal plane. The path differences between the two beams in Figure

3.7 can be simply calculated by using Bragg's law. This parameter depends on incident

angle (2θ) and spacing between the parallel crystal planes. In order to keep these beams in phase, their path difference ($SQ + QT = 2d\sin\theta$) has to equal one or multiple X-ray wavelength (λ).

The intensity of the diffracted X-ray is measured as a function of the diffraction angle and orientation of a specimen. In this thesis, the XRD pattern were recorded within a $5° - 80°$ angle range of 2θ; the scan step was 0.02 °/s. The crystalline phase identification was carried out by comparison with the Jiont Committee on Powder Diffraction Standards (JCPDS) diffraction files. The Rietveld refinement of X-ray diffraction pattern for as-prepared materials at room temperature was performed using X'Pert Plus program to determine the average crystallite size in this thesis.

The estimated crystalline size of the samples were calculated from X-ray line broadening of the diffraction peak by using Scherrer's equation as given by equation (3.2)

$$D = \frac{K}{\beta\theta} \tag{3.2}$$

where K is a constant depending on the XRD equipment and has been determined to vary between $0.89 - 1.39$, but is usually taken as close to unity. For this study, $K = 0.90$, λ is the wavelength of the X-ray radiation, θ is the diffraction angle, and β is the full-width at half maximum (FWHM) of XRD peak.

3.2.2 Transmission electron microscope (TEM)

Transmission electron microscope (TEM) is an electron microscopy technique used to examine the powder structure, phase composition or properties in submicroscopic detail. Zeiss CEM 902 as shown in Figure 3.8 was used in this work. A beam of electrons is transmitted through an ultra-thin specimen, interacting with the specimen as it passes through. An image is formed from the interaction of the electrons transmitted through the

specimen; the image is magnified and focused onto an imaging device, such as a fluorescent

screen, on a layer of photographic film, or to be detected by a sensor such as a CCD camera.

Figure 3.8 Zeiss CEM 902 TEM (University of Puket Sound)

A diffraction pattern is formed on the back focal plane of the objective lens when

an electron beam passes through a crystalline specimen in a TEM. In the diffraction mode, a

pattern of selected area electron diffraction (SAED) can be further enlarged on the screen or

recorded by a camera. The diffraction angle in the TEM is very small (commonly $\theta < 1°$),

because the reflecting lattice planes are nearly parallel to the primary beam. Using the

approximation $\sin\theta \approx \theta$ for a small angle, we can rewrite Bragg's Law as the following.

$$\lambda = 2d\theta \tag{3.3}$$

$$\lambda L = Rd \tag{3.4}$$

where L is the camera length of a TEM, whitch is a distance between the crystal

and photographic plate of camera. This parameter is an equivalent camera length for cal-

culating the spacing of the lattice plane. L (equation (3.3)) is called as the camera constant

of the TEM. equation (3.4) is the basic equation for calculation of the crystallographic spacing planes by measuring the distance from the central spot of the transmitted beam to diffraction spot (R) in diffraction pattern image using equation (3.4) L can be changed in a TEM.

In this work, the specimens of rGO-based nanocomposites were prepared by dispersing the as-synthesized samples in ethanol, ultrasonication for $15\,\mathrm{min}$ and followed by drop-casting onto a copper grid. TEM also provided selected area electron diffraction (SAED) patterns of the samples, which were used to compliment XRD results.

3.2.3 Fourier transform infrared spectroscopy (FTIR)

In this research, the prepared rGO-based nanocomposites were mixed with KBr and grinding together and then collected into a circular tablet mould and pressed with a pressure of $1\,\mathrm{MPa}$. The as-prepared sample was placed onto the holder of Bruker Vertex 70 spectrophotometer (Figure 3.9) for obtaining an infrared spectrum in the wavenumber of $4,000 - 400\,\mathrm{cm}^{-1}$ range.

Figure 3.9 Bruker Vertex 70 spectrophotometer at SUT.

The key component in the FTIR system is the Michelson interferometer, the in-

frared radiation from a source enters the Michelson interferometer and composed of one beam-splitter and two mirrors. The beam-splitter transmits of the infrared (IR) beam from the source and reflects the other half. The two split beams strike a fixed mirror and moving mirror, respectively. After reflecting from the mirrors, the two split beams combine at the beam splitter again in order to the irradiation of the sample before the beam are received by the detector.

3.2.4   Raman Spectroscopy

In this work, JOBIN YVON HORIBAT64000 Raman spectroscopy system Figure (3.10) was used to study mophology of rGO and rGO–based nanocomposites. Raman spectroscopy (Ferrari et al., 2006) is one of the most powerful characterization techniques for carbon materials. Graphite and graphene can be identified by Raman scattering spectra. As shown in Figure 3.11, graphite has three most intense Raman, G-band, which is due to doubly degenerate E_{2g} mode at the Brillouin zone centre, is located at ~ 1580 cm^{-1}, D-band, which arises from defect mediated zone-edge (near K-point) phonons, is located at ~ 1350 cm^{-1}, and $2D$-band, which originates from second order double resonant Raman scattering from zone boundary, is located at ~ 2700 cm^{-1}

(a) JOBIN YVON HORIBAT64000 Raman spectroscopy system at Chiang Mai University.
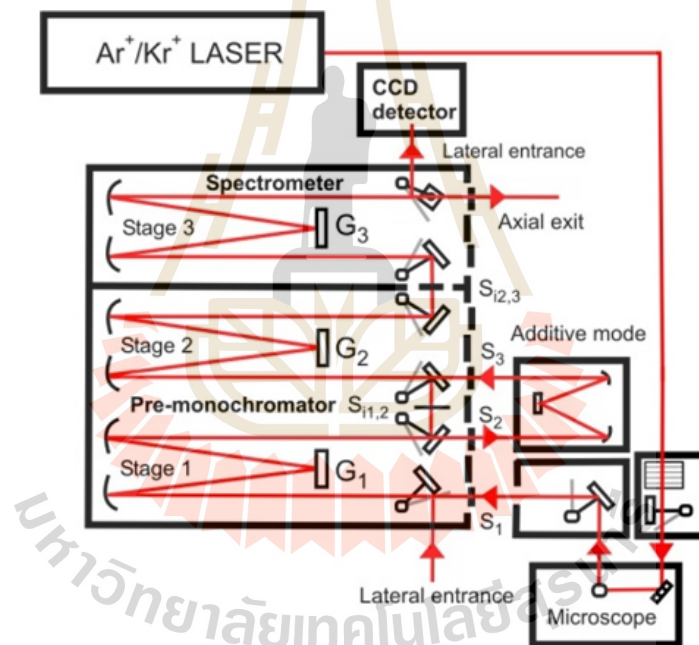
(b) T64000 Optical functional diagram

Figure 3.10 JOBIN YVON HORIBAT64000 Raman spectroscopy system at Chiang

Mai University.
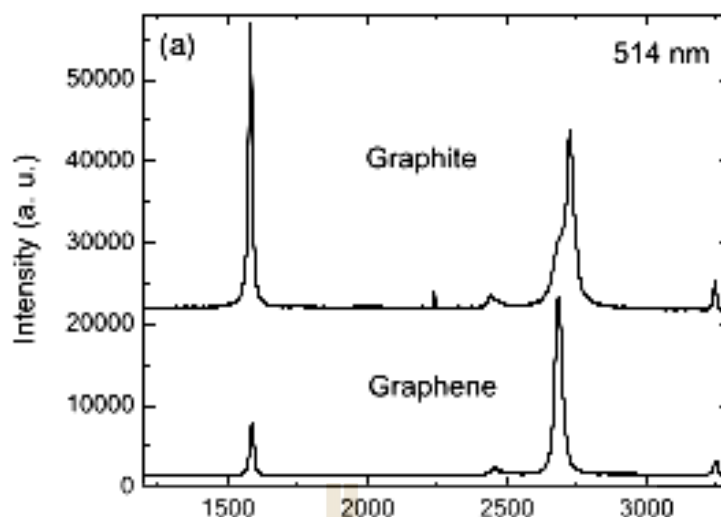
Figure 3.11 Raman spectra of graphite and graphene (Ferrari et al., 2006).

3.2.5 Brunauer–Emmett–Teller (BET)

Stephen Brunauer, Paul Hugh Emmett, and Edward Teller published the first article about the BET theory in 1938 (Brunauer, Emmett and Teller, 1938). Brunauer–Emmett–Teller (BET) theory (Figure 3.12) can be used to explain the physical adsorption of gas molecules on a solid surface and this technigue is very important for the specific surface area measurement of a material. A surface area data can be determined by measure the adsorption of were studied by nitrogen isothermal adsorption as shown in Figure 3.12a. The pore size distribution of materials was further verified by BJH technigue as shown in Figure 3.12b. The specific surface area of rGO-based nanocomposite were investigated by using Bel Sorp mini II as shown in Figure 3.13.
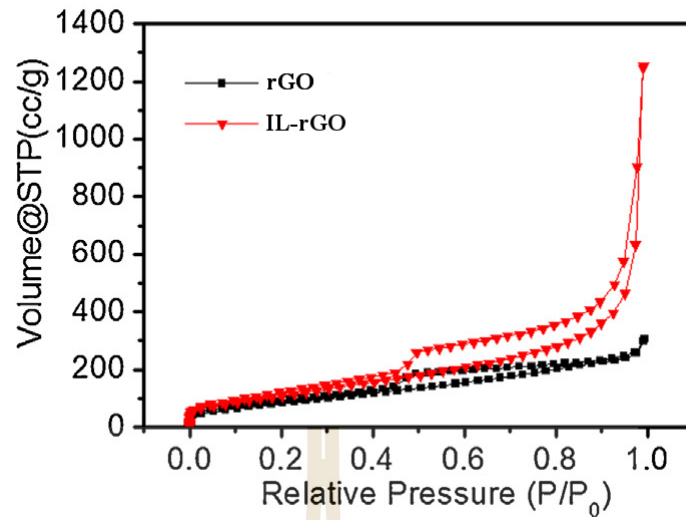
(a) Nitrogen adsorption isotherms
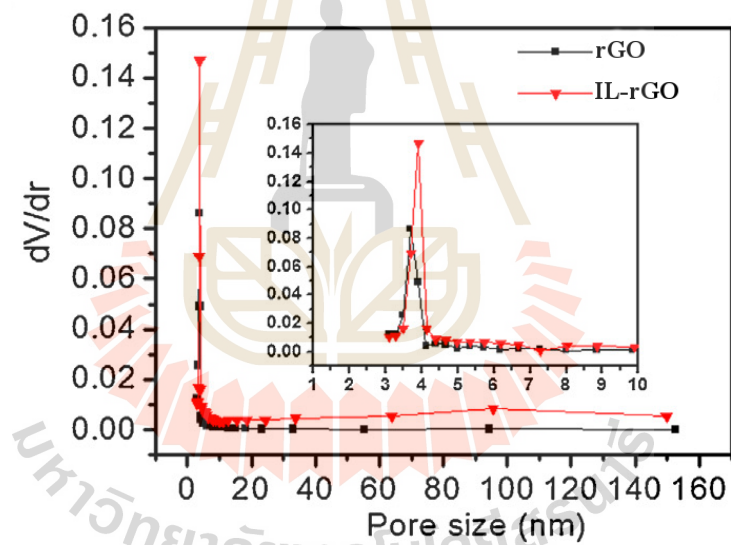
(b) BJH desorption pore size distribution curves in the pore size distribution plot is a little larger than that of rGO, which further confirms the 3D structure with more separated graphene sheets

Figure 3.12 The specific surface area (SSA) and the pore structure of rGO and IL − rGO (Q. Shao et al., 2015).

Figure 3.13 Bel Sorp mini II (sut.ac.th)

3.3 Electrical properties measurement

The electrochemical properties of the prepared electrodes were carried out using three-electrode cell system in which an Ag/AgCl in $3.0\,\mathrm{M}$ HCl and a platinum wire ($0.5\,\mathrm{mm}$ of diameter) were used as reference and counter electrodes, respectively. Cyclic voltammetry (CV), galvanostatic charge-discharge (GCD) and electrochemical impedance spectroscopy (EIS) were carried out in a three-electrode cell system in $6.0\mathrm{M}$ KOH aqueous electrolyte. The electrochemical properties were performed on Metrohm Autolab PGSTAT 302N (Figure 3.14) and the data information was analyzed by using NOVA 1.11 software.
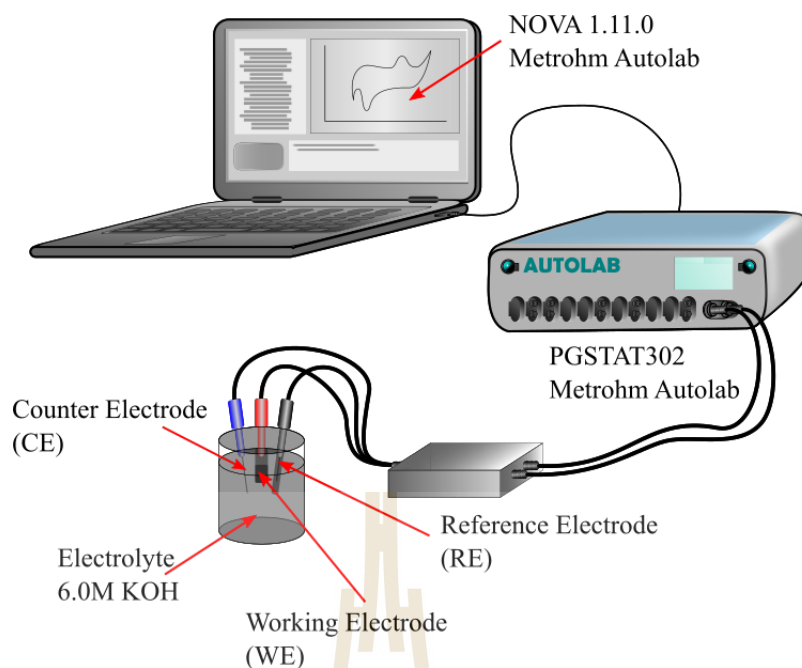
Figure 3.14 Metrohm Autolab PGSTAT 302N

3.3.1 Electrolyte preparation

The electrolyte solutions in this work was 6.0 M KOH aqueous solution, which was prepared by dissolving the KOH powder in distilled water. The concentration in molar (M) was calculated by following the equation:

$$\text{Molar concentration (M)} = \frac{\text{Amount of KOH in mole (mol)}}{\text{Volume of KOH solution of 1000 ml}} \quad (3.5)$$

KOH powder of 84.1590 gram was added into DI water of 150 ml in volumetric flask and sonicated until the powder was well dissolved. After that, DI water was added into the flask untill volume of the solution was 250 ml and sonicated to form 6.0 M KOH electrolyte solution for electrochemical measurement of the working electrode.

3.3.2 Working electrode preparation

Active materials, were mixed with acetylene black (AC) and polyvinylidene fluoride (PVDF) at the ratio of 80 : 10 : 10%w. Then, the mixture was made more homo-

geneous by adding with a small amount of N-Methyl-2-pyrrolidone (NMP). The working electrodes were fabricated by pressing the mixture onto a nickel foam sheet of $1.0 \text{ cm} \times 1.0 \text{ cm}$ as shown in Figure 3.15 and dried at $120°C$ for 5 h and soaked into $6.0M$ KOH for 6 h before performing an electrochemical measurement.
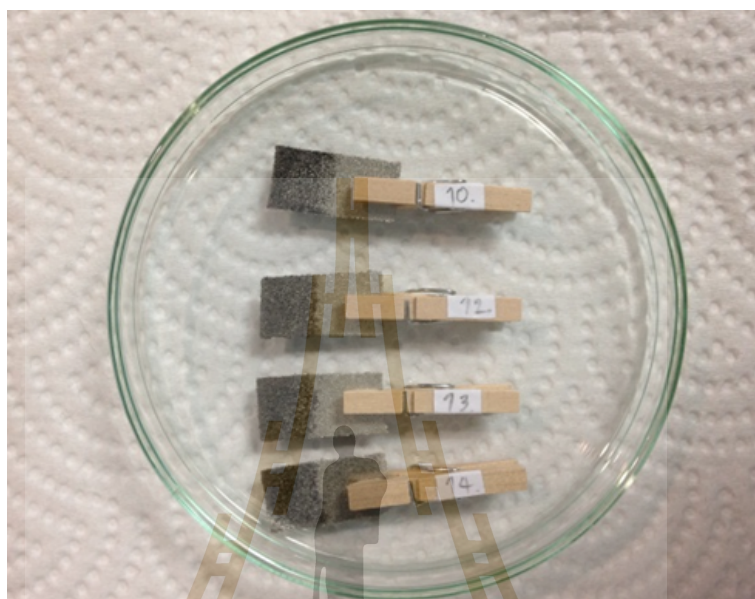
Figure 3.15 rGO-based material were fabricated onto Ni foam substrate.

3.3.3 Electrochemical properties measurement

Cyclic voltammetry (CV), Galvanostatic charge-discharge (GCD) and Electrochemical Impedance Spectroscopy (EIS) methods are the widely known important techniques for analyzation of the electrochemical properties of the fabricated supercapacitor electrodes.

3.3.4 Cyclic voltammetry

In this study, the pseudocapacitance of metal oxides and conducting polymers has been evaluated by cyclic voltammetry (CV) method. One of electrode system measurement is three-electrode system consisting of working electrode, counter electrode and reference electrode in appropriate supporting electrolytes at various scan rates. The CV was measured

within potential windows of $-1 - 0$ V to avoid the oxygen and hydrogen evolution at scan rates of 10, 20, 50, 100, and 200 mV/s within 6.0 M KOH. The effect of voltage potential windows on specific capacitance was also studied by the following equation (3.6).

$$C_s = \frac{1}{m\Delta V} \int I dt \qquad (3.6)$$

where, I is the discharge current, m is the weight of electrode, and ΔV is the potential window.

3.3.5 Galvanostatic charge-discharge (GCD)

The galvanostatic charge-discharge (GCD) or by chronopotentiometry method was carried out over the same potential windows and electrolyte solution as CV measurement at 2, 5, 10, 15, and 20 ampere/g . The average specific capacitance of the working electrodes can be evaluated from the following equation (3.7)

$$C_s = i\frac{\Delta t}{\Delta V} \qquad (3.7)$$

where, i is the current density, ΔV is the potential window, and Δt is the discharge time (Yan, Liu, Fan, Wei and Zhang, 2012).

The stability measurement was observed by using GCD method for 1000 cycles of charge-discharge process at current density of 10 A/g.

3.3.6 Electrochemical impedance spectroscopy (EIS)

Electrochemical impedance spectroscopy is one of the technique, which has been used to evaluate the specific capacitance value. In this study the EIS was monitored over the frequency range of 10 mHz to 100 kHz at 0.1 V.

CHAPTER IV

RESULTS AND DISCUSSION

This chapter presents the experimental results and discussion for rGO-based nanocomposite and its electrochemical properties. The physical properties of the as-prepared products are shown in the result of XRD, TEM, FTIR, and BET. The electrochemical properties of working electrode are measured by using CV, GCD and EIS. In addition, the specific capacitance retention have been investigated and discussed.

4.1 Reduced graphene oxide (rGO) preparation

As following rGO preparation process in Sec. 3.1.3, Figure 4.1 shows the preparation of rGO using hydrothermal method at 200 °C for 24 h. After oxidized by KMnO$_4$ in strong acid 98% of H$_2$SO$_4$ by a modified Hummers method. A d-spacing of 0.33 nm of graphite was expanded to 0.83 nm to form GO powder with functional groups of oxygen. GO powder dispersed in DI water with concentration of 0.5 mg/ml by ultrasonication for 30 min. After dispersion, GO was form graphene oxide with random orientation of monolayer of GO. A solution of graphene oxide was reduced by hydrothermal method using hydrazine monohydrate (H$_4$N$_2$ · H$_2$O) as a reducing agent at 200 °C for 24 h. Finally, some of oxygen-containing groups was removed, it formed rGO nanosheets with some disorder and functional group. The formation of rGO could be confirmed by XRD, TEM and Raman spectroscopy.
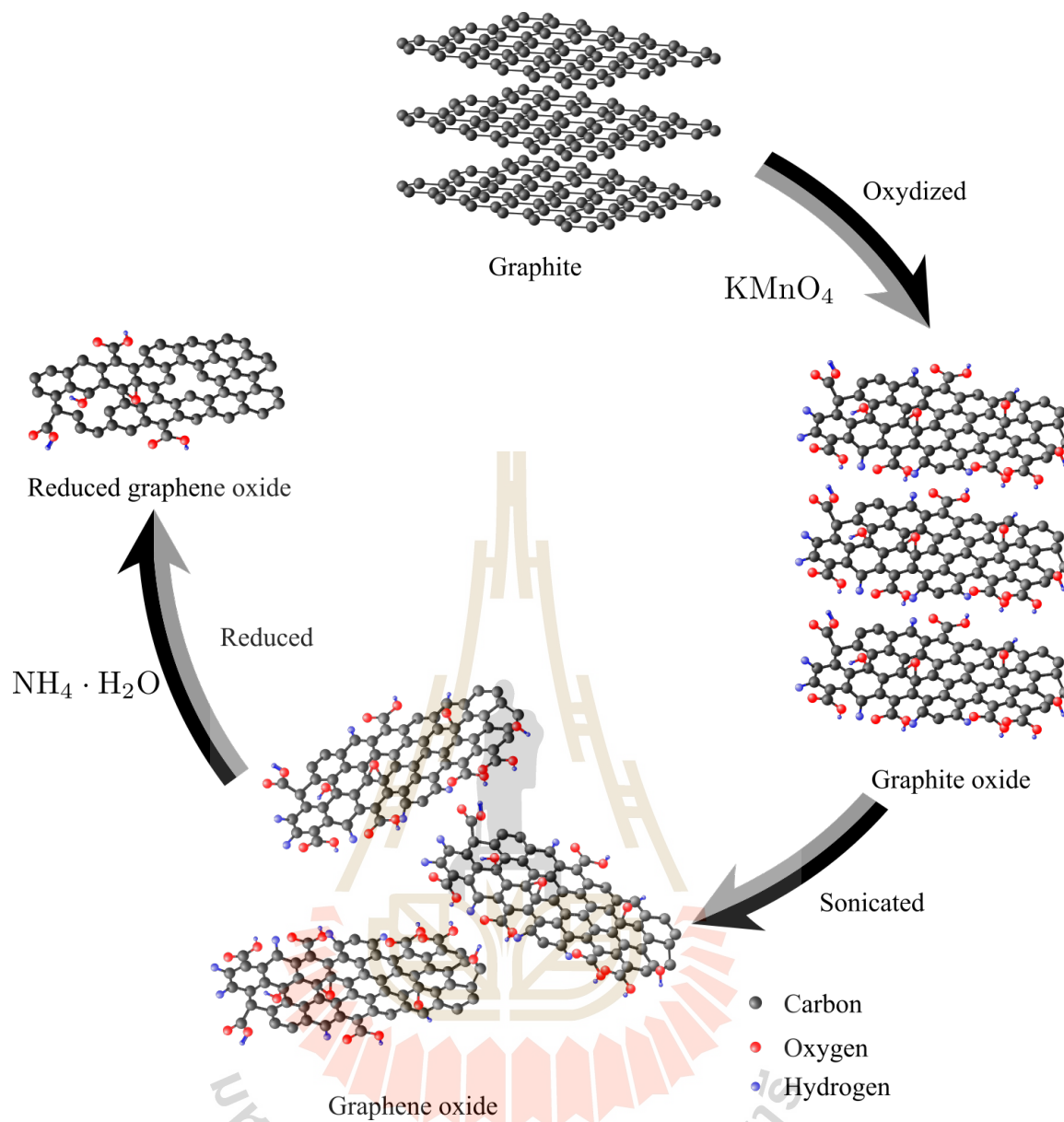
Figure 4.1 Reduced graphene oxide (rGO) preparation by reduction of grahite oxide

(GO) with hydrazine monohydrate ($H_4N_2 \cdot H_2O$) as reagent material by

using graphite powder as raw material (adapted from Joshi et al., 2014).

Figure 4.2 shows bright-field TEM images of the objects typically observed, which

generally fall into monolayer rGO nanosheets. The normal-incidence electron diffraction

pattern of the flake in Figure 4.2 shows the typical sixfold symmetry expected for graphite/

graphene allowing us to label the peaks with the Miller–Bravias (hkil) indices. The result

shows that the inner peaks, (0110) and (1010), are more intense than the outer ones, (1210) and (2110), confirming that both the flake in Figure 4.2 are monolayers (Hernandez et al., 2008).
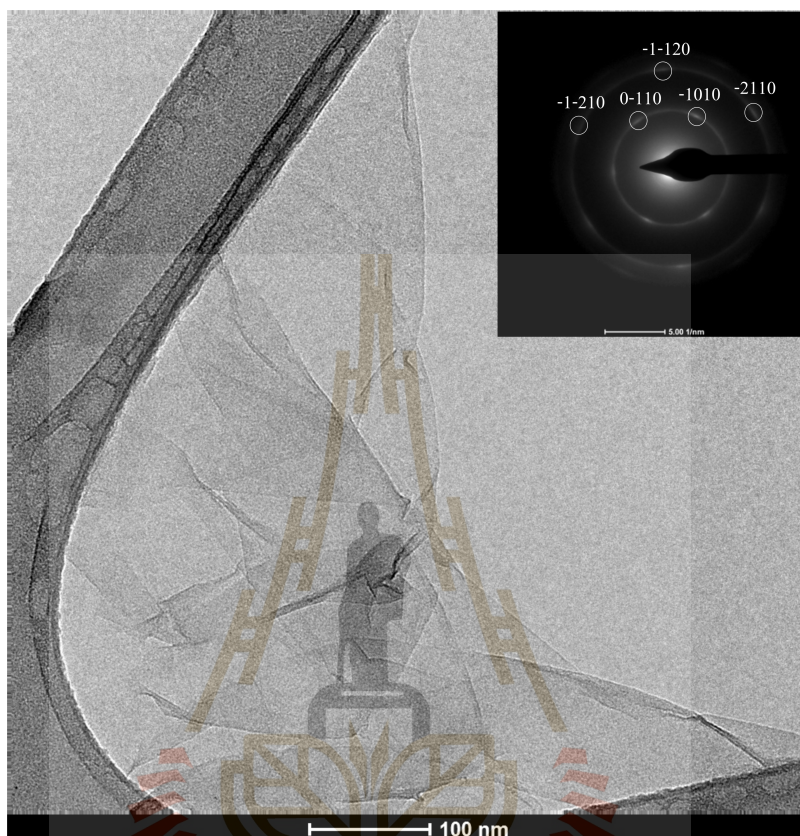
Figure 4.2 TEM images of as-prepared reduced graphene oxide (rGO).

The formation of rGO is confirmed by Raman spectroscopy in Figure 4.3. The Raman spectrum of rGO shows the two provident peaks at 1337 cm^{-1} and 1580 cm^{-1} of $D-$peak and $G-$peak, respectively. The $D-$peak is associated with the defects and disorder in lattice structure of graphitic material, whereas the $G-$peak peak is corresponded to the vibrations of sp^2-bond of C. To obtain the information of defects and degree of graphitization, the I_D/I_G ratio was evaluated using the intensity values of $D-$peak and $G-$peak. In case of rGO, the I_D/I_G ratio is 1.50, which is higher than the value of 0.91 for GO. It can be suggested that the degree of defects of rGO is higher than that of GO.

After adding $MnFe_2O_4$ nanoparticles onto the rGO nanosheets, the sp^2 domains of graphitic structure is decreased.
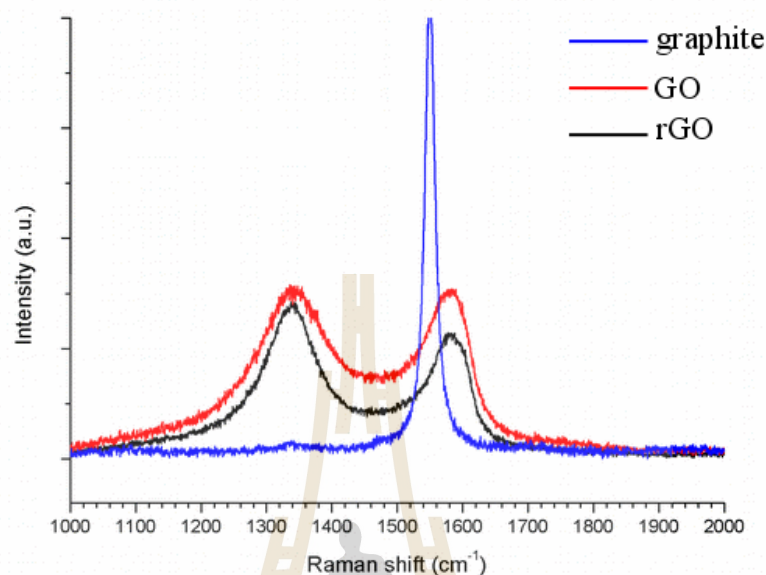
Figure 4.3 Raman spectroscopy of graphite, graphite oxide (GO), and reduced graphene oxide (rGO).

After oxydation of graphite powder by $KMnO_4$ in strong acid of 98% H_2SO_4, graphite powder was formed into graphite oxide. A characteristic peak of graphite at 26.8° with 0.33 nm of d-spacing was shifted to 10.70° with 0.83 nm d-spacing. GO powder was dissolved in DI water with 0.5 mg/ml by sonicate with ultrasonic for 30 min. After reduction, A characteristic peak of rGO shows as an amophous carbon structure due to the random orientation of rGO sheet at 25.5°.

4.2 rgo/MnFe$_2$O$_4$ nanocomposites

4.2.1 Physical properties

Figure 4.4 shows the XRD patterns of the as-prepared rGO, MnFe$_2$O$_4$, rGO/MFO05 and rGO/MFO10. It can be seen that the XRD patterns of rGO exhibit two weak and broad diffraction peaks at 2θ values of about $25.02°$ and $43.00°$, which relate to a poorly crystallized compound originating from the small particle size and approximately amorphous nature of the sample. The peak at a 2θ value of about $25.02°$ with d-spacing of 0.356 nm corresponds to the (002) plane of rGO. This peak is shifted from a 2θ value of $10.27°$ (d-spacing 0.824 nm) after reduction of GO. This phenomenon occurrs because of the removal of some oxygen-containing functional groups, indicating the reduction of GO and the exfoliation of the layered rGO nanosheet. Broad peaks relate to a poorly crystallized compound originating from the small particle size and approximately amorphous nature of the sample. The peak at a 2θ value of about $43.00°$ with d-spacing of 0.210 nm corresponds to the (100) crystal plane of graphene (Yan, Wei, Fan et al., 2010). In the case of MnFe$_2$O$_4$, rGO/MFO05, and rGO/MFO10, the diffraction peaks corresponding to (111), (220), (311), (400), (422), (511), (440), and (533) planes, which can be indexed to the FCC structure of MnFe$_2$O$_4$ (JCPDS-10-0319) (K. Zhang et al., 2010). Additionally, for rGO/MFO05 and rGO/MFO10 nanocomposites, the rGO characteristic diffraction peak at a 2θ value of about $25.02°$ with low intensity was also observed. It is seen from the XRD results that the FWHM of the MnFe$_2$O$_4$ peak in rGO/MFO05 is broader than that of the rGO/MFO10. This is due to the MnFe$_2$O$_4$ size effect. To confirm this we have calculated the crystallite size of MnFe$_2$O$_4$ in the samples using Scherrer's equation (Yan, Wei, Fan et al., 2010) ($D = 0.89\lambda/\beta\cos\theta$, where λ is the wavelength of $X-ray$ radiation, θ is the

diffraction angle, and β is the line broadening at half the maximum intensity (FWHM), after subtracting the instrumental line broadening, of the most intense peak corresponds to the (311) plane measured in radians), and the crystallite sizes of the as-prepared samples are obtained to be 27.37, 12.15, and 21.15 nm for the $MnFe_2O_4$, rGO/MFO05 and rGO/MFO10, respectively.
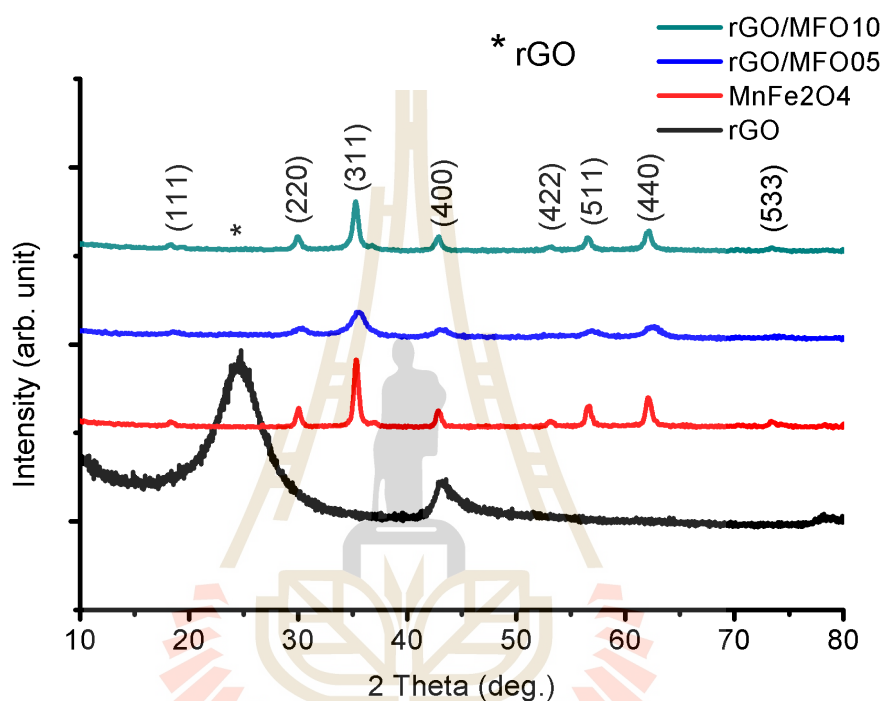
Figure 4.4 XRD patterns of rGO, $MnFe_2O_4$, rGO/MFO05, and rGO/MFO10.

Figure 4.5 shows TEM images of rGO, $MnFe_2O_4$, and rGO/MFO05 nano- composite prepared by hydrothermal approach. The bare $MnFe_2O_4$ nanoparticles show a spherical shape with agglomeration, having average particle size of about 25.2 nm, whereas the rGO/MFO05 nanocomposite shows thin rGO sheet decorated with well dispersed $MnFe_2O_4$ nanoparticles with smaller average particle size of about 15.3 nm. This is possibly ascribed to the intimate interaction between bare rGO/MFO05 nanoparticles and graphene nanosheets, which limits the agglomeration of rGO/MFO05 nanoparticles to some extents. The results of electron diffraction patterns of rGO/MFO05 and

rGO/MnFe$_2$O$_4$ are in good agreement with the XRD results.
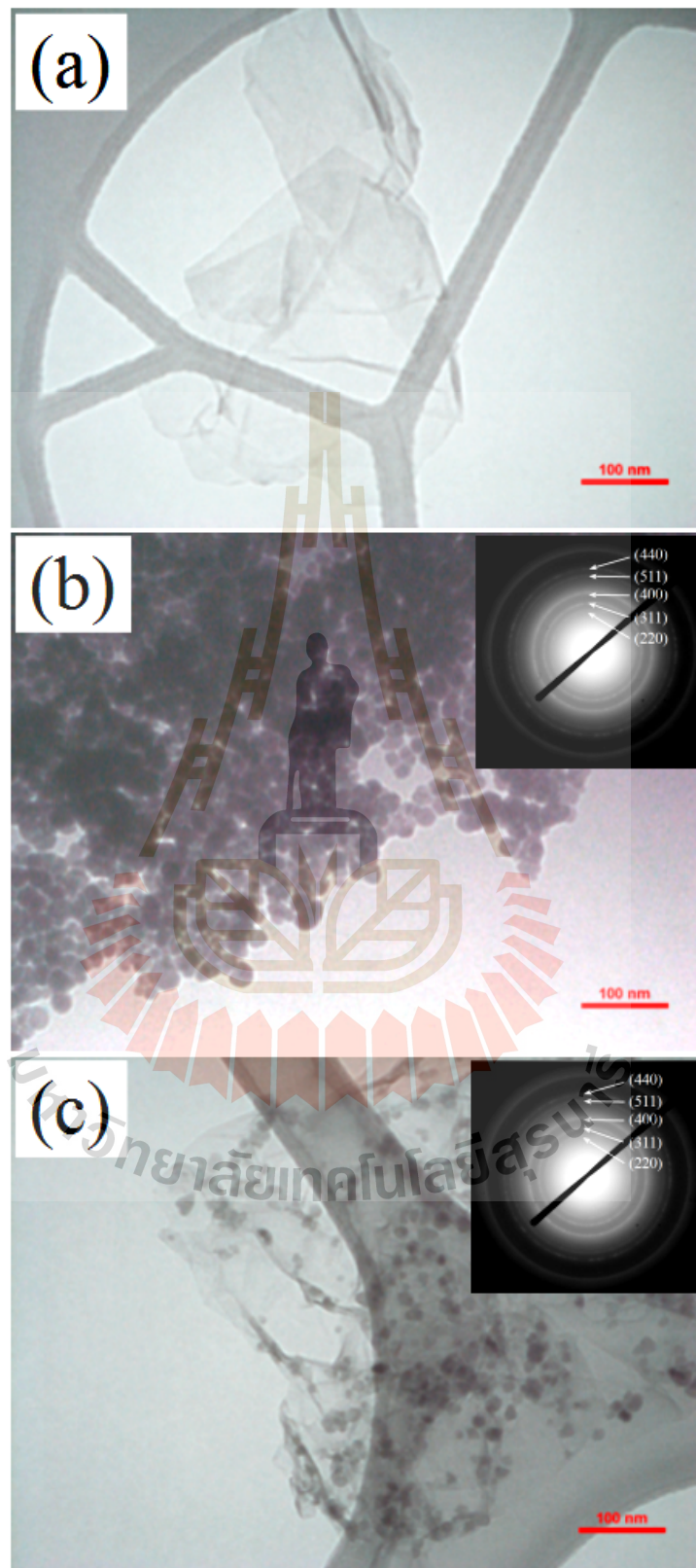
Figure 4.5 TEM images of (a) rGO, (b) MnFe$_2$O$_4$, and (c) rGO/MnFe$_2$O$_4$.

Figure 4.6 shows the FTIR spectra of GO, rGO, and rGO/MFO05 nanocomposite. The typical peaks of GO at $3385\,\text{cm}^{-1}$ can be attributed to $O-H$ stretching vibration of absorbed water molecules and structural OH groups, the presence of the carboxylic $(C=O)$ functional groups can also be observed at $1725\,\text{cm}^{-1}$. The peak at $1622\,\text{cm}^{-1}$ is ascribed to the $O-H$ bending vibration and the peak at $1226\,\text{cm}^{-1}$ and $1057\,\text{cm}^{-1}$ indicate the presence of epoxide groups $(C-O-C)$. After the reduction to form rGO and $\text{rGO/MnFe}_2\text{O}_4$ nanocomposite, the peaks at $1725\,\text{cm}^{-1}$ disappears and the peaks at $1622\,\text{cm}^{-1}$, $1226\,\text{cm}^{-1}$ and $1057\,\text{cm}^{-1}$ gradually decrease while a new peak is appeared at $1558\,\text{cm}^{-1}$ reflecting the skeletal vibration of graphene sheets (Y. Zhu, James and Tour, 2012). These evidences confirm that the rGO and rGO–based nanocomposite can be prepared by the reduction of graphite oxide and manganese iron oxide precursor.
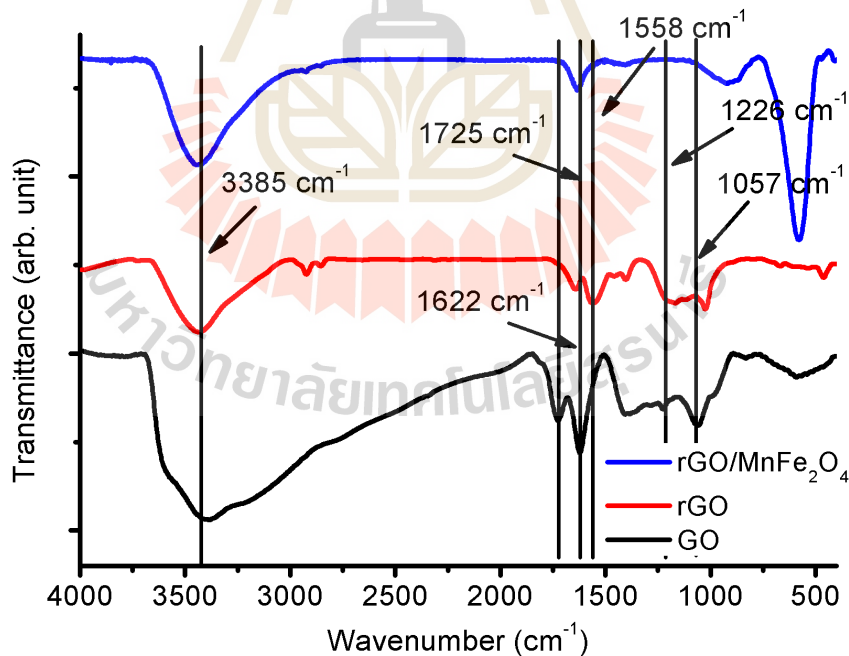
Figure 4.6 FTIR spectra of GO, rGO, and rGO/MFO05.

The specific surface area and pore structure of the prepared samples were investigated by N_2 adsorption-desorption isotherms and the results are shown in Figure 4.7. The specific surface area values of the as-prepared rGO and $MnFe_2O_4$ measured by BET technique are $414.38\,m^2/g$ and $47.83\,m^2/g$, respectively. After decoration by $MnFe_2O_4$, the specific surface area of $rGO/MnFe_2O_4$ nanocomposite decreases to $294.24\,m^2/g$ with mean mesopore size of $4.11\,nm$ obtained by the mean of BJH equation. The large specific surface area and large mean pore size of the material are very important for allowing the electrolyte ions to penetrate pore surface of the electrode for providing a high specific capacitance.
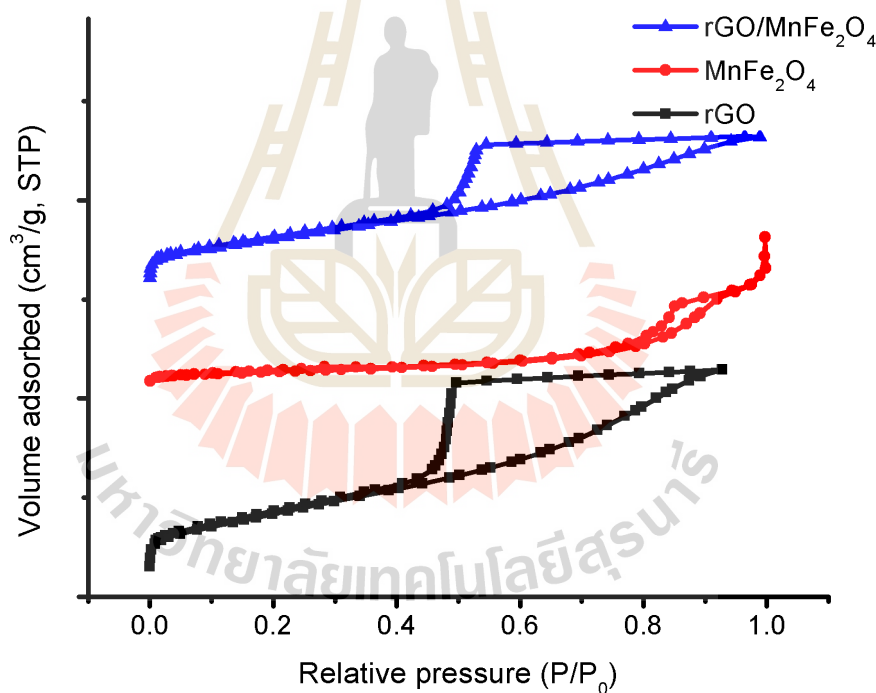
Figure 4.7 Nitrogen adsorption-desorption isotherm of rGO, $MnFe_2O_4$, and $rGO/MnFe_2O_4$.

Figure 4.8 shows Raman spectra of as-prepared samples, which are operated at 100 to $4000\,cm^{-1}$. The Raman spectrum of rGO shows the two provident peaks at $1337\,cm^{-1}$ and $1580\,cm^{-1}$ of $D-peak$ and $G-peak$, respectively. The $D-peak$ is associated with

the defects and disorder in lattice structure of graphitic material, whereas the $G-peak$ corresponds to the vibrations of sp^2-bonded of C (Casiraghi, Pisana, Novoselov, Geim and Ferrari, 2007; Eda and Chhowalla, 2010). To obtain the information of defects and degree of graphitization, the I_D/I_G ratio is evaluated using the intensity values of $D-peak$ and $G-peak$. In case of rGO, the I_D/I_G ratio is 1.50, which is higher than the value of 0.91 for GO. It can be suggested that the degree of defects of rGO is higher than that of GO. After adding $MnFe_2O_4$ nanoparticles onto the rGO nanosheets, the sp^2 domains of graphitic structure is decreased. Therefore, it can be found that the I_D/I_G ratio of $MnFe_2O_4$ is lower than rGO and the $D-peak$ and $G-peak$ are blue-shifted to 1338, and $1381\,cm^{-1}$ compared to those of rGO, respectively. Moreover, the vibrational modes of $MnFe_2O_4$ can be observed at the wavenumber lower than $700\,cm^{-1}$.
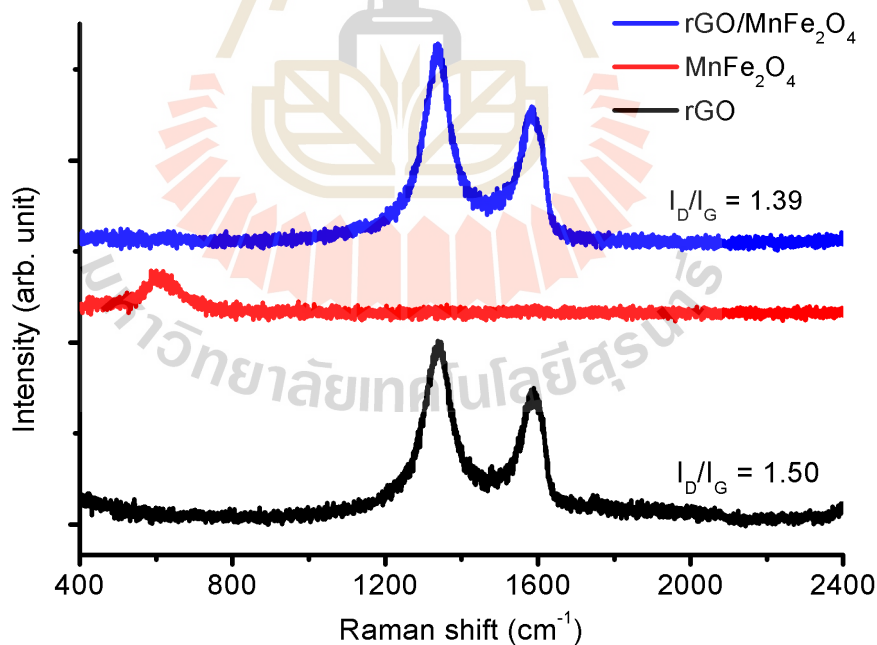
Figure 4.8 Raman spectra of rGO, $MnFe_2O_4$, and $rGO/MnFe_2O_4$.

4.2.2 Electrochemical performance

The cyclic voltammetry measurements (CV) were performed within the potential range of -1.0 to $0.0\,$V at room temperature over a scan rate of $10, 20, 50, 100,$ and $200\,$mV/s and the galvanostatic charge-discharge (GCD) were used to study a capacitive behavior of the working electrodes at a current density of $2.0, 5.0, 10.0, 15.0,$ and $20.0\,$A/g. Figure 4.9 - 4.14 shows the CV and GCD curves of rGO, rGO/MFO05, and rGO/MFO10 within $6.0\,$M KOH aqueous electrolyte. These results indicate that the specific capacitance (Cs) of electrodes are increased when the scan rate and current density, which are applied to the electrode increase.
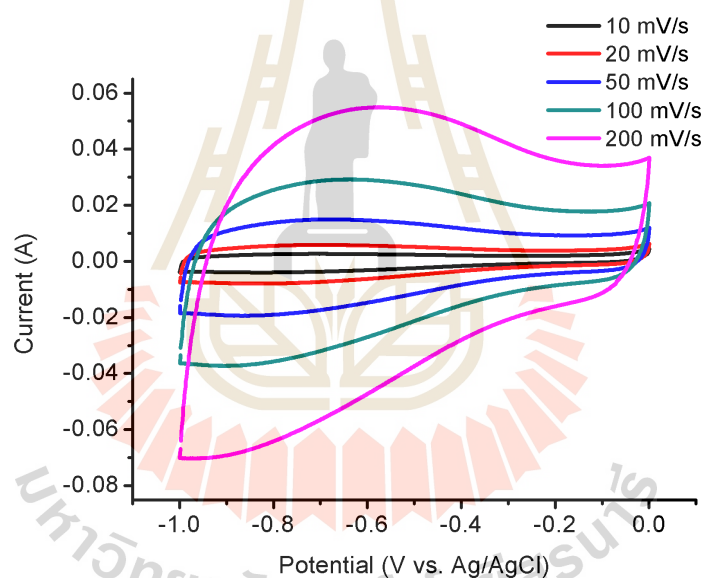
Figure 4.9 Cyclic voltammograms of rGO in $6.0\,$M KOH aqueous electrolyte at scan rate of $10\,$mV/s.
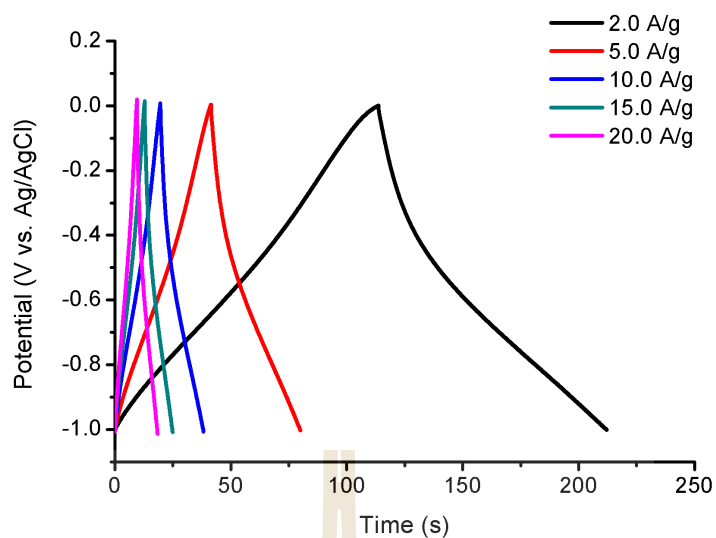
Figure 4.10 Galvanostatic charge-discharge of rGO in $6.0\,\mathrm{M}$ KOH aqueous electrolyte at current density of $5.0\,\mathrm{A/g}$.
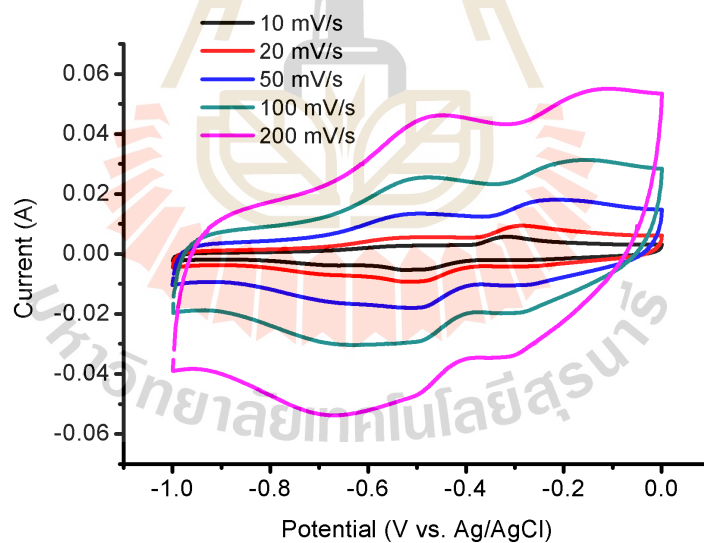
Figure 4.11 Cyclic voltammograms of rGO/MFO05 in $6.0\,\mathrm{M}$ KOH aqueous electrolyte at scan rate of $10\,\mathrm{mV/s}$.
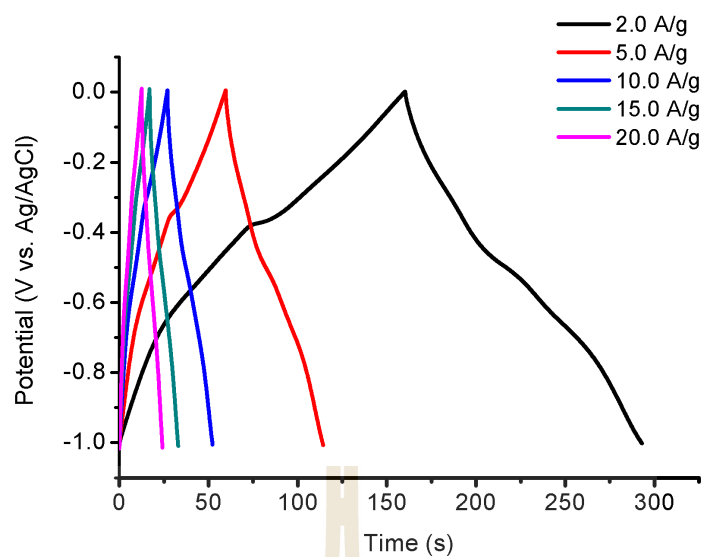
Figure 4.12 Galvanostatic charge-discharge of rGO/MFO05 in 6.0 M KOH aqueous

electrolyte at current density of 5.0 A/g.
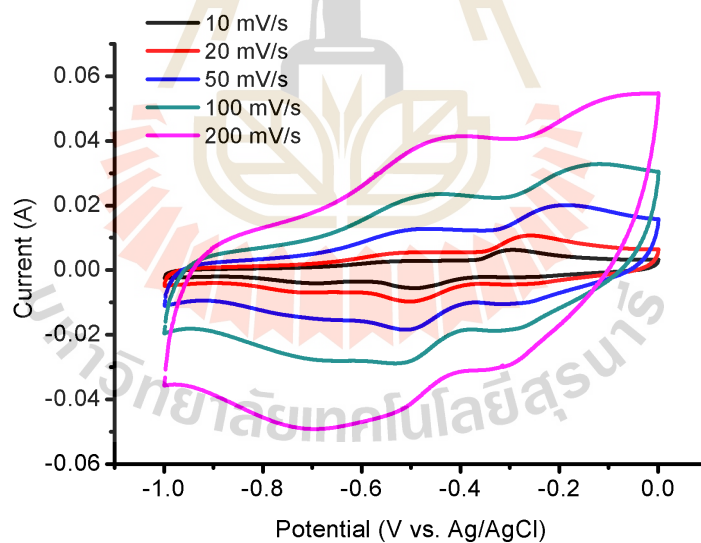
Figure 4.13 Cyclic voltammograms of rGO/MFO10 in 6.0 M KOH aqueous electrolyte at scan rate of 10 mV/s.
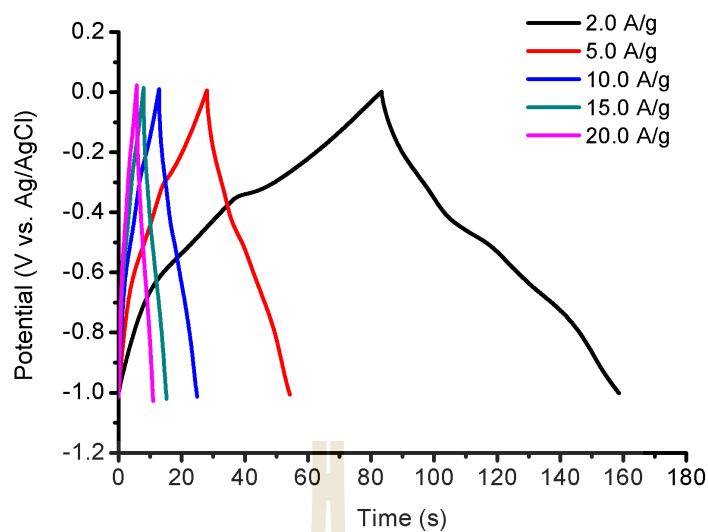
Figure 4.14 Galvanostatic charge-discharge of rGO/MFO10 in 6.0 M KOH aqueous

electrolyte at current density of 5.0 A/g.

Figure 4.15 shows comparison of the C_s obtained from cyclic voltammograms at a

scan rate of 10 mV/s. The measured C_s values of the rGO, rGO/MFO05, and rGO/MFO10

are obtained to be 190.3, 276.9, and 144.5 F/g, respectively. These values, respectively,

correspond to the values of 194.9, 274.6, and 134.4 F/g obtained from GCD measurement

at a current density of 5.0 A/g as shown in Figure 4.16.
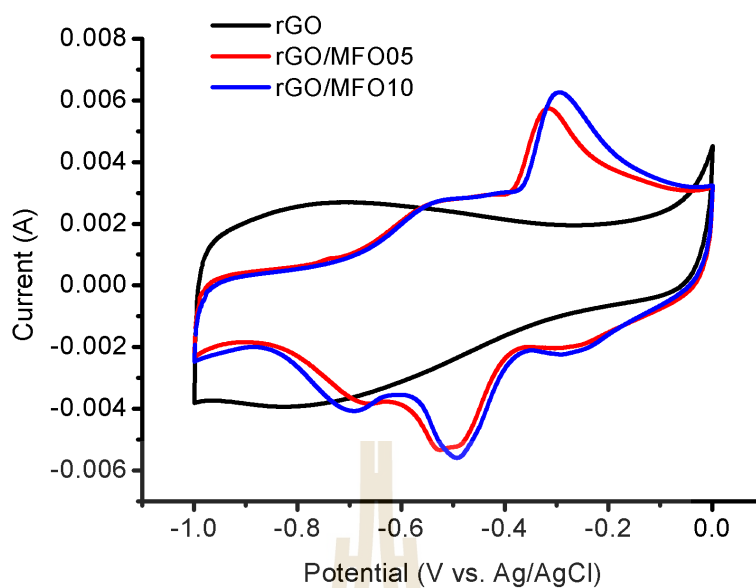
Figure 4.15 Cyclic voltammograms and galvanostatic charge-discharge of rGO, rGO/MFO05, and rGO/MFO10 in 6.0 M KOH aqueous electrolyte at scan rate of 10 mV/s.
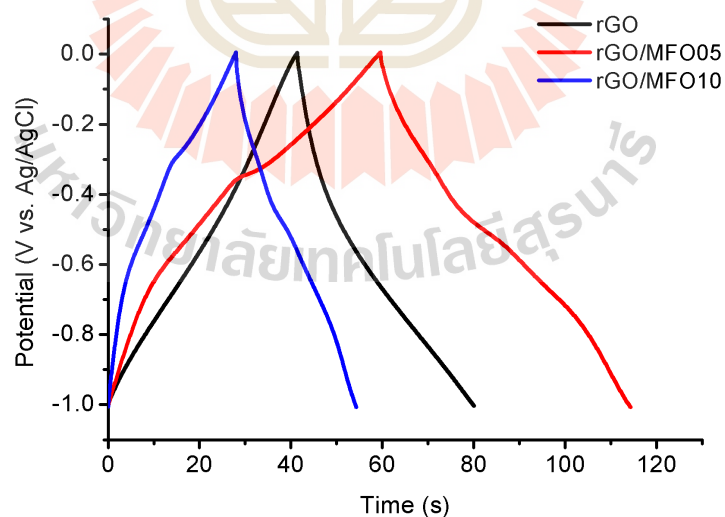
Figure 4.16 Galvanostatic charge-discharge (GCD) of rGO, rGO/MFO05, and rGO/MFO10 at scan rate of $10\,\mathrm{mV \cdot s}$ in 6.0 M KOH aqueous electrolyte at current density of 5.0 A/g.

Figure 4.17 shows the specific capacitance plots of rGO, rGO/MFO05, and rGO/MFO10 at different applied current densities. It can be found that the frabricated electrode of rGO/MFO05, has the highest capacitance than those of the rGO, and rGO/MFO10 at all applied current densities. This can be seen that decoration of $MnFe_2O_4$ nanoparticle on rGO nanosheet can improve the capacitive behavior of rGO, but for rGO/MFO10, the decrease of specific surface area, mean pore size and large number of oxygen-containing groups on the working electrode is possibly due to the poor rate capability. Consequently, these results are evidence of the increasing diffusion resistance towards the ions transfer into the electrode pores and thus causing a decrease of a specific capacitance (Stoller, Park, Zhu, An and Ruoff, 2008).
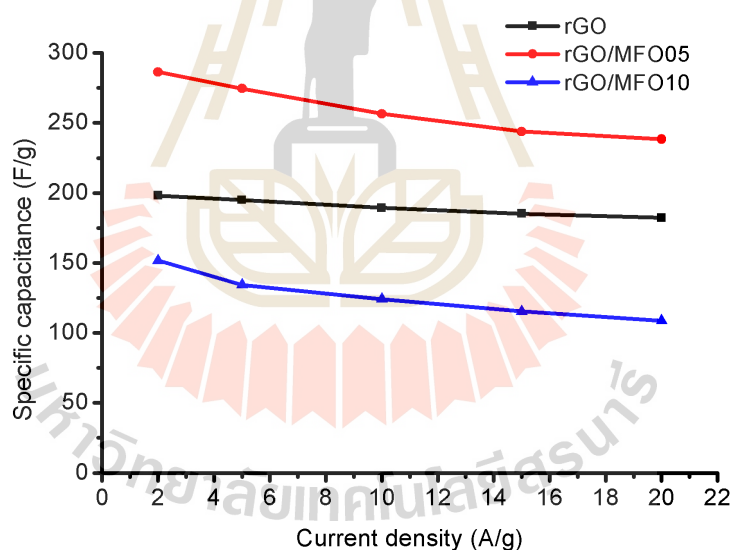
Figure 4.17 The specific capacitance plots of rGO, rGO/MFO05, and rGO/MFO10 at different current densities.

Figure 4.18 shows the Ragone plot, which shows a relation curve of the energy density and power density. It can be seen that, as the power density of rGO/MFO05 increases from $2.28\,kW/kg$ to $9.15\,kW/kg$, the energy density decreases from $37.7\,kW \cdot h/kg$

to $31.64\,\mathrm{kW\cdot h/kg}$. While, the power density of $\mathrm{rGO/MFO10}$ increases from $2.23\,\mathrm{kW/kg}$ to $8.40\,\mathrm{kW/kg}$, the energy density decreases from $20.7\,\mathrm{kW\cdot h/kg}$ to $13.3\,\mathrm{kW\cdot h/kg}$. These results indicate that the energy loss of the $\mathrm{rGO/MFO10}$ is less than that of the $\mathrm{rGO/MFO05}$.
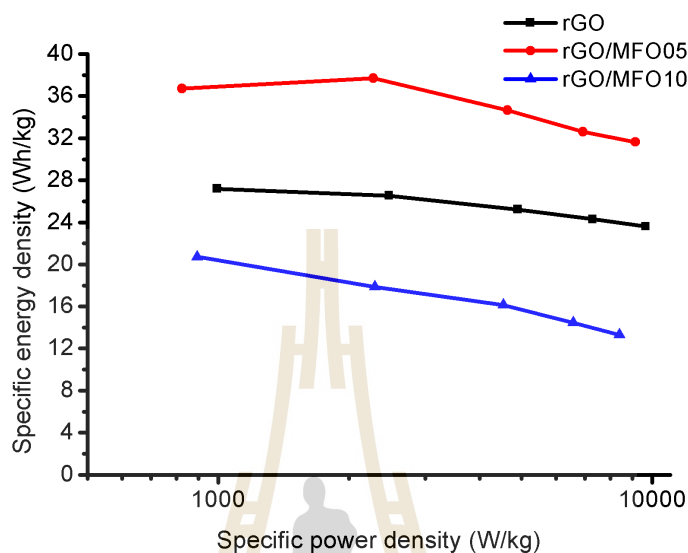
Figure 4.18 Ragone plot of the specific energy and specific power densities of rGO, rGO/MFO05, and rGO/MFO10.

The EIS analysis was also used to investigate the electrochemical behavior of the working electrode within the frequency range of $100\,\mathrm{kHz}-0.1\,\mathrm{Hz}$ and amplitude of $0.01\,\mathrm{V}$. The Nyquist plots of the electrodes and electrochemical equivalent circuit are shown in Figure 4.19. The solution resistance (ESR) is referred to the resistance of the electrolyte, which is obtained from the intersection of the high frequency region at x-axis, and known as equivalent series resistance (ESR) (Lu et al., 2010). The total resistance at the interface between the electrode and electrolyte and charge-transfer resistance (R_{ct}) corresponds to the total resistance at the interface between the electrode and electrolyte. rGO has ESR of $0.375\,\Omega$ and R_{ct} of $0.047\,\Omega$ which is lower than that of $\mathrm{rGO/MFO05}$ (ESR $= 0.457\,\Omega$, and $R_{ct} = 0.069\,\Omega$). Therefore, the $\mathrm{rGO/MFO05}$ has higher specific capacitance than rGO and

rGO/MFO05. The Warburg resistance, considered at the portion of the with slope of $45°$, is caused by the ions diffusion or transport in the electrolyte in the surface of the electrode and was depended on the frequency (Stoller et al., 2008). At the low frequency region, the oblique of the vertical line is shown the ideal capacitor. The knee frequencies, which are the lowest value with a slope of $45°$ before behaving an ideal capacitor are 3.29 and $2.31\,\text{Hz}$ for the rGO/MFO05, and rGO/MFO10, respectively. This suggests that rGO/MFO05 has higher knee frequency and more vertical than rGO/MFO10. This can demonstrate that rGO/MFO05 behaves more closely to ideal capacitor than rGO/MFO10. The Q_1 or CPE, is referred to a phase constant device. The n value of CPE depends on the behavior of the electrode. The rGO/MFO05 and rGO/MFO10 has 0.995 and 0.992 of the n, respectively. This indicates that both of electrodes imply the ideal capacitor (L. Chen, Gu, Ding, Qi and Wang, 2013).
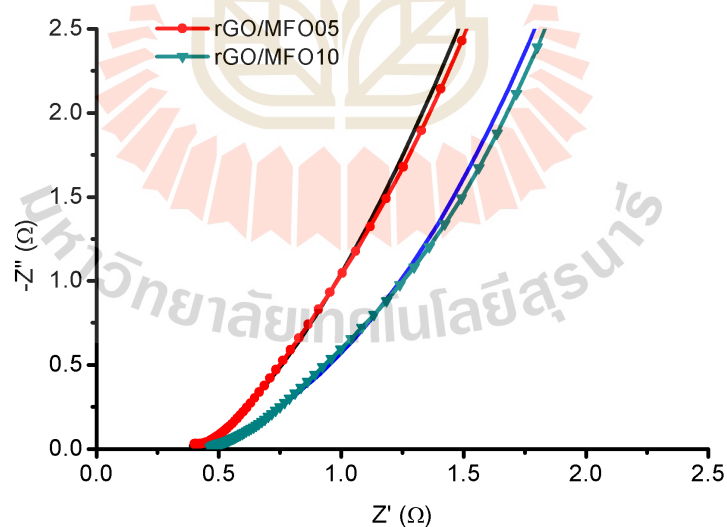
Figure 4.19 Nyquist impedance plots of rGO/MFO05, and rGO/MFO10 electrodes.
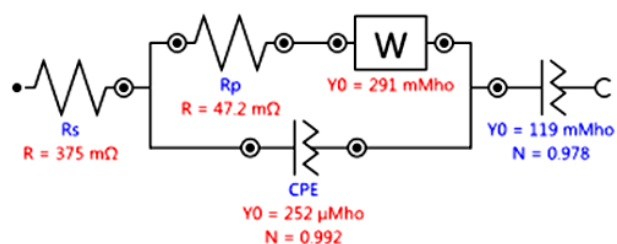
(a)
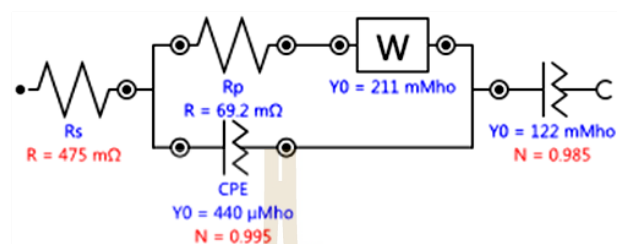
(b)

Figure 4.20 Equivalent circuit of 4.20a rGO/MFO05, and 4.20b rGO/MFO05 electrodes.

Moreover, to study the long-term cycle stability of the fabricated electrodes, the specific capacitance retention was evaluated by galvanostatic charge-discharge at $10.0\,\mathrm{A/g}$ for 1000 cycles. Figure 4.21 shows the relation between specific capacitance retention and cycle number of the 1000 cycles charge-discharge process. It can be found that all electrodes provide the excellent cycling stability. The rGO working electrode has the highest retention. Before 500 cycles of the charge-discharge, The capacitance of rGO/MFO05 decreases more quickly than rGO/MFO10, but after 500 cycles it becomes more stable than rGO/MFO05
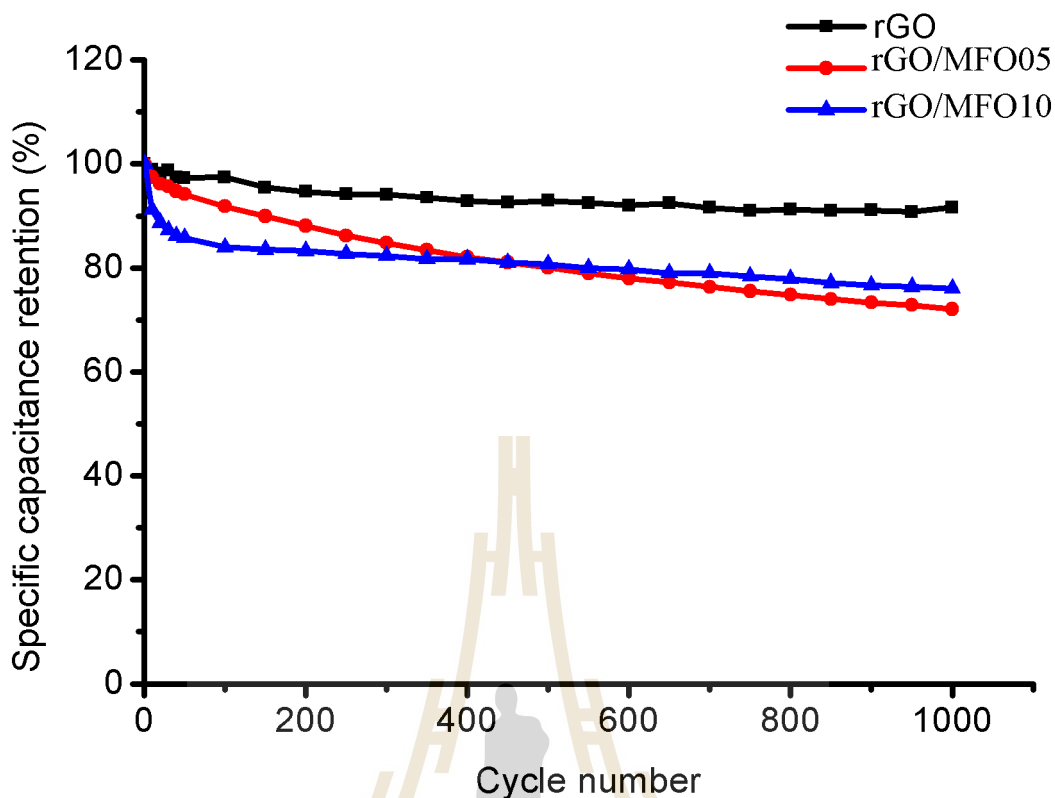
Figure 4.21 Cycling stability of rGO, rGO/MFO05, and rGO/MFO10 using galvanostatic charge-discharge at current density of $10\,\mathrm{A/g}$.

4.3 rGO/CoFe$_2$O$_4$ nanocomposites

4.3.1 Physical properties

Figure 4.22 shows the XRD patterns of the as-prepared rGO, CoFe$_2$O$_4$, and rGO/CFO05. It can be seen that the XRD patterns of rGO exhibit two weak and broad diffraction peaks at 2θ values of about $25.02°$ and $43.00°$, which relate to a poorly crystallized compound originating from the small particle size and approximately amorphous nature of the sample. The peak at a 2θ value of about $25.02°$ with d-spacing of $0.356\,\mathrm{nm}$ corresponded to the (002) plane of rGO. This peak shifted from a 2θ value of $10.27°$

(d-spacing $0.824\,\text{nm}$) after reduction of GO. This phenomenon occurred because of the removal of some oxygen-containing functional groups, indicating the reduction of GO and the exfoliation of the layered rGO nanosheet. Broad peaks relate to a poorly crystallized compound originating from the small particle size and approximately amorphous nature of the sample. The peak at a 2θ value of about $43.00°$ with d-spacing of $0.210\,\text{nm}$ corresponds to the (100) crystal plane of graphene (Yan, Wei, Shao et al., 2010). In the case of $CoFe_2O_4$, and rGO/CFO05, the diffraction peaks corresponding to (111), (220), (311), (400), (422), (511), (440), and (533) planes, which can be indexed to the FCC structure of $CoFe_2O_4$ (JCPDS card no. 01-077-0426) (Houshiar, Zebhi, Razi, Alidoust and Askari, 2014). Additionally, for rGO/CFO05 nanocomposites, the rGO characteristic diffraction peak at a 2θ value of about $25.02°$ with low intensity was also observed. It is seen from the XRD results that the FWHM of the $CoFe_2O_4$ peak in rGO/CFO05. This is due to the $CoFe_2O_4$ size effect. To confirm this we calculated the crystallite size of $CoFe_2O_4$ in the samples using Scherrer's equation (Yan, Wei, Fan et al., 2010) ($D = 0.89\lambda/\beta\cos\theta$, where λ is the wavelength of X-ray radiation, θ is the diffraction angle, and β is the line broadening at half the maximum intensity (FWHM), after subtracting the instrumental line broadening, of the most intense peak corresponds to the (311) plane measured in radians), and the crystallite sizes of the as-prepared samples were obtained to be 27.37, 12.15, and $21.15\,\text{nm}$ for the $CoFe_2O_4$, and rGO/CFO05, respectively.
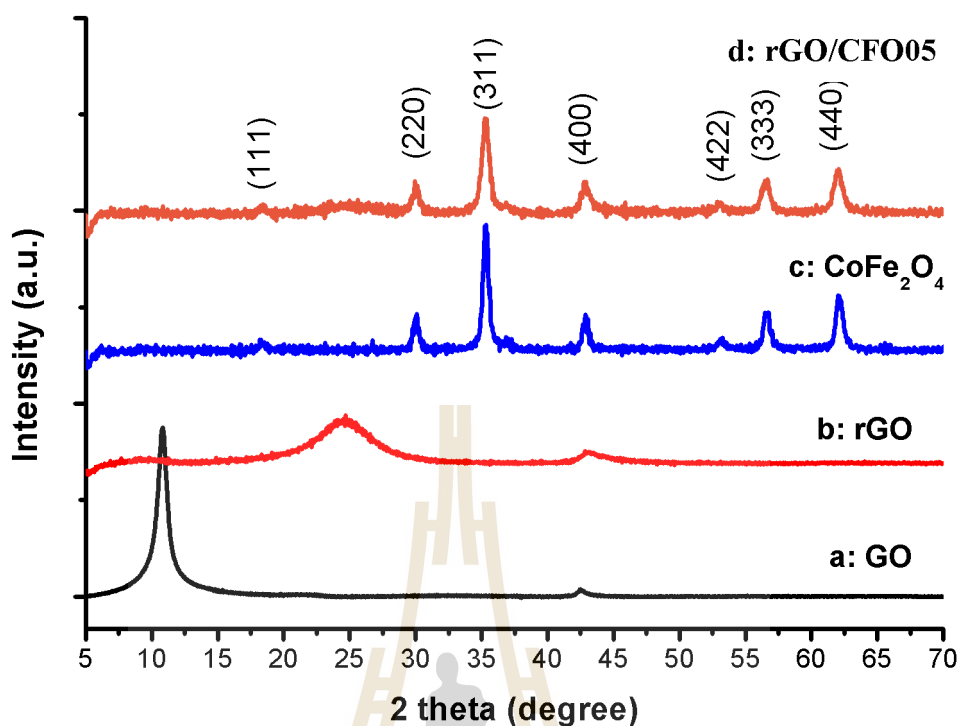
Figure 4.22 XRD patterns of (a) rGO, (b) $CoFe_2O_4$, and (c) rGO/CFO05.

As shown in Figure 4.23, TEM images of rGO, $CoFe_2O_4$, and rGO/CFO05 nanocomposite prepared by hydrothermal approach. The bare $CoFe_2O_4$ nanoparticles showed in spherical particles with aggregation, having average particle size of about 27.3 nm, whereas the rGO/CFO05 nanocomposite shown that rGO sheet decorated with well dispersed $CoFe_2O_4$ nanoparticles with smaller average particle size of about 22.4 nm. This is possibly ascribed to the intimate interaction between bare $CoFe_2O_4$ nanoparticles and graphene sheets, which limits the agglomeration of $CoFe_2O_4$ nanoparticles to some extents. The results of electron diffraction patterns of $CoFe_2O_4$ and rGO/CFO05 are in good agreement with the XRD results.
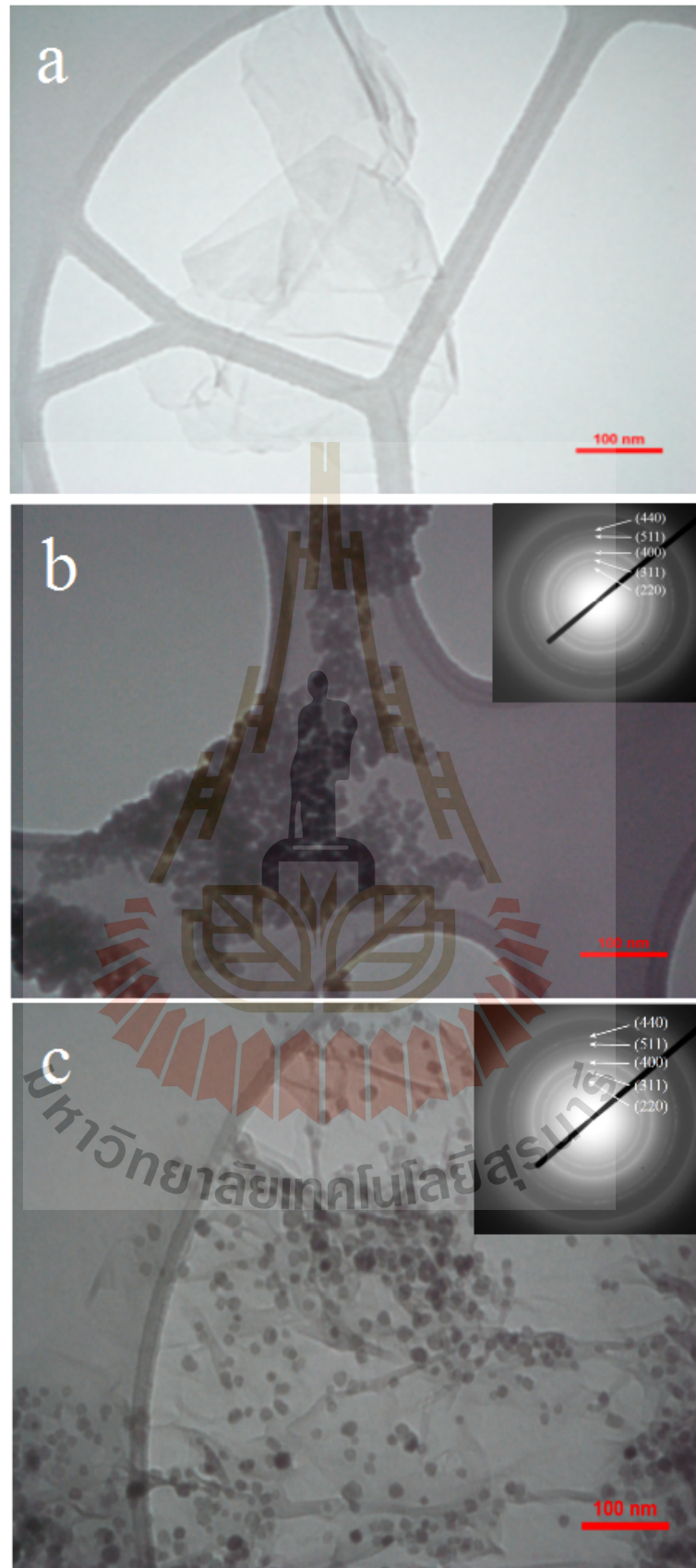
Figure 4.23 TEM images of (a) rGO, (b) CoFe$_2$O$_4$, and (c) rGO/CFO05.

The FTIR spectra of GO, rGO, and rGO/CFO05 are shown in Figure 4.24. The typical peaks of GO at $3385\,\mathrm{cm}^{-1}$ can be attributed to $\mathrm{O-H}$ stretching vibration of absorbed water molecules and structural $\mathrm{O-H}$ groups. The presence ofthe carboxylic $(\mathrm{C=O})$ functional groups can also be observed at $1725\,\mathrm{cm}^{-1}$. The peak at $1622\,\mathrm{cm}^{-1}$ is ascribed to the $\mathrm{O-H}$ bending vibration and the peaks at 1226 and $1057\,\mathrm{cm}^{-1}$ indicate the presence of epoxide groups $(\mathrm{C-O-C})$. After the reduction to form rGO and rGO/CFO05 nanocomposite, the peaks at $1725\,\mathrm{cm}^{-1}$ disappears and the peaks at 1622, 1226, and $1057\,\mathrm{cm}^{-1}$ gradually decrease while a new peak is appeared at $1558\,\mathrm{cm}^{-1}$ reflecting the skeletal vibration of graphene sheets. This evidence confirms that the rGO and rGO-based nanocomposite can be prepared by the reduction of graphite oxide and cobalt iron oxide precursor.
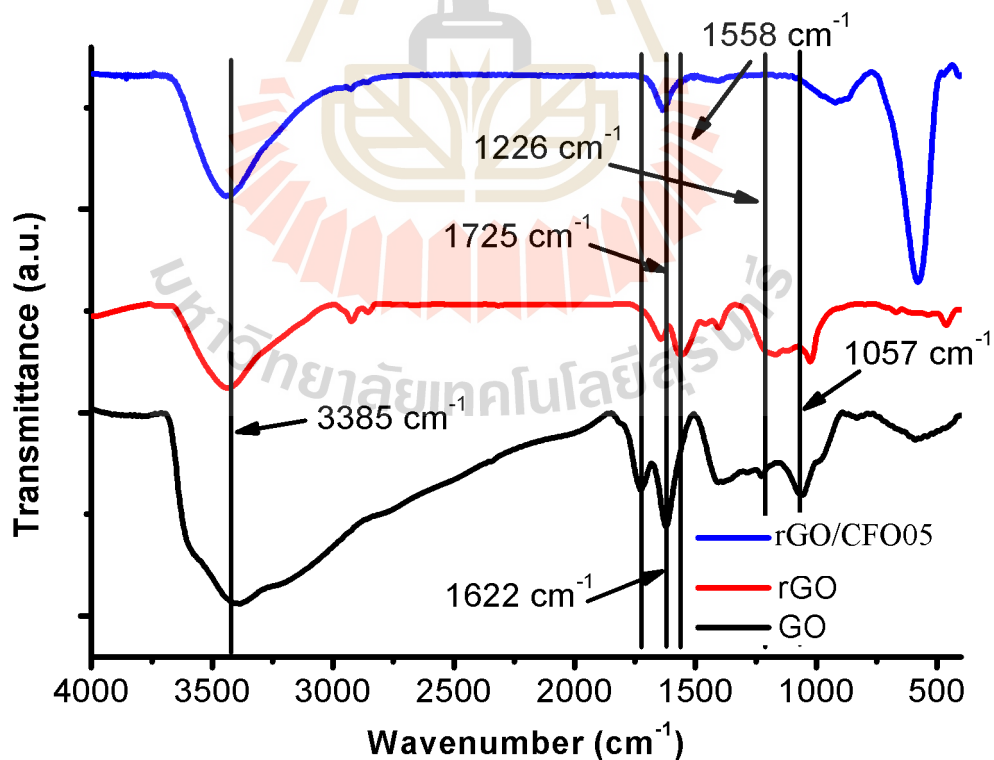
Figure 4.24 FTIR spectra of GO, rGO, and rGO/CFO05.

The specific surface area and pore structure of the prepared samples were investigated by N_2 adsorption-desorption isotherms and the results are shown in Figure 4.25. The specific surface area values of the as-prepared rGO and $CoFe_2O_4$ measured by BET technique are $414.38\,\mathrm{m^2/g}$ and $68.31\,\mathrm{m^2/g}$, respectively. After decoration by $CoFe_2O_4$, the specific surface area of rGO/CFO05 nanocomposite decreases to $302.17\,\mathrm{m^2/g}$ with mean mesopore size of $5.04\,\mathrm{nm}$ obtained by the mean of BJH equation. The large specific surface area and large mean pore size of the material are very important for allowing the electrolyte ions to penetrate pore surface of the electrode for providing a high specific capacitance.
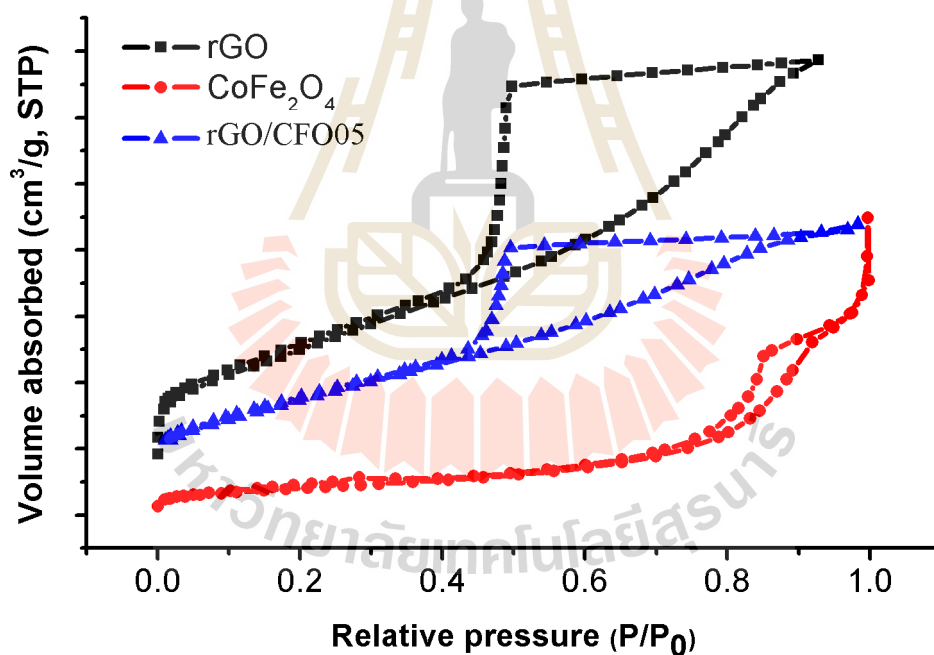
Figure 4.25 Nitrogen adsorption-desorption isotherm of rGO, $CoFe_2O_4$, and rGO/CFO05.

Raman spectra of rGO and rGO/CFO05, which operated at 100 to 4000 $\mathrm{cm^{-1}}$ are shown in Figure 4.26. Two provident peaks of the Raman spectrum of rGO show

at $1337\,\mathrm{cm}^{-1}$ and $1580\,\mathrm{cm}^{-1}$ of $\mathrm{D-peak}$ and $\mathrm{G-peak}$, respectively. The $\mathrm{D-peak}$ is associated with the defects and disorder in lattice structure of graphitic material, whereas the $\mathrm{G-peak}$ is corresponded to the vibrations of sp^2-bonded of carbon. To obtain the information of defects and degree of graphitization, the $\mathrm{I_D/I_G}$ ratio was evaluated using the intensity values of $\mathrm{D-peak}$ and $\mathrm{G-peak}$. In case of rGO, the $\mathrm{I_D/I_G}$ ratio was 1.50, which is higher the value of 0.91 for GO. It can be suggested that the degree of defects of rGO is higher than than that of GO. After adding $\mathrm{CoFe_2O_4}$ nanoparticles onto the rGO nanosheets, the sp^2 domains of graphitic structure was decreased. Therefore, it can be found that the $\mathrm{I_D/I_G}$ ratio of $\mathrm{rGO/CFO05}$ was 1.38 which lower than rGO and GO the $\mathrm{D-peak}$ and $\mathrm{G-peak}$ were blue-shifted to 1338, and $1381\,\mathrm{cm}^{-1}$ compared to those of rGO, respectively.
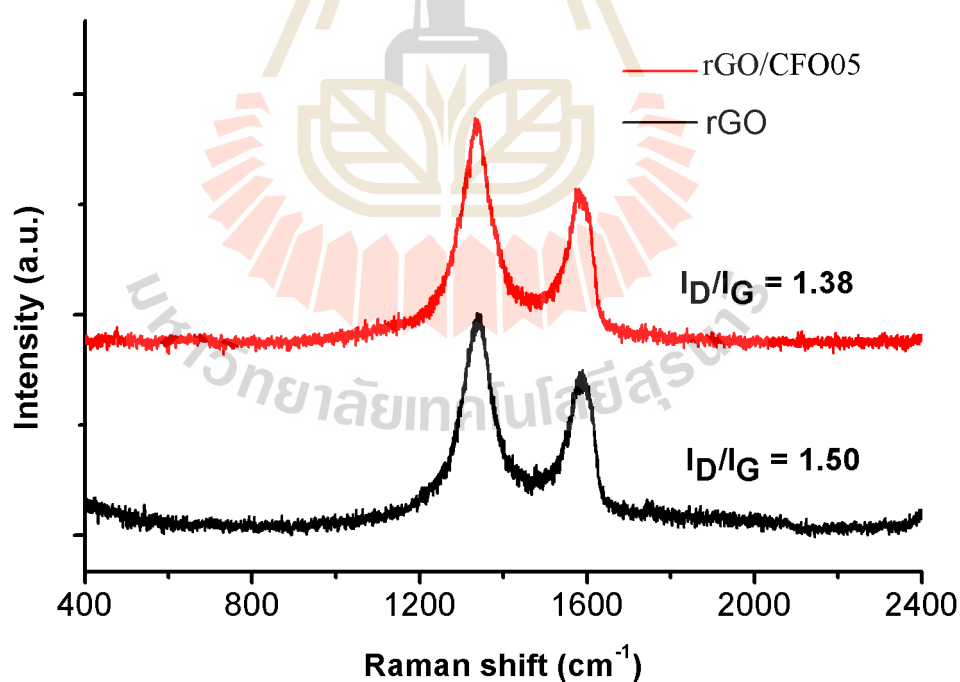
Figure 4.26 Raman spectra of rGO, $\mathrm{CoFe_2O_4}$, and $\mathrm{rGO/CFO05}$.

4.3.2 Electrochemical performance

Figure 4.27a shows comparison of the Cs obtained from cyclic voltammograms at a scan rate of $10 \, \text{mV/s}$. The measured Cs values of the rGO, and rGO/CFO05 were obtained to be 190.3, and $203.5 \, \text{F/g}$, respectively. These values, respectively, correspond to the values of 194.9, and $223.1 \, \text{F/g}$ obtained from GCD measurementat a current density of $5.0 \, \text{A/g}$ as shown in Figure 4.27.
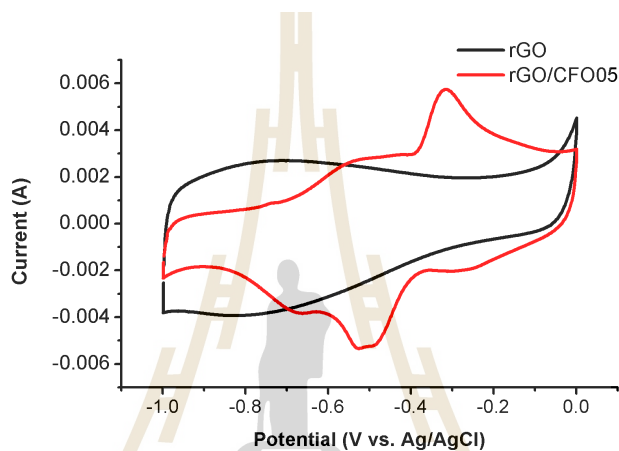
(a) Cyclic voltammograms at scan rate of $10 \, \text{mV/s}$
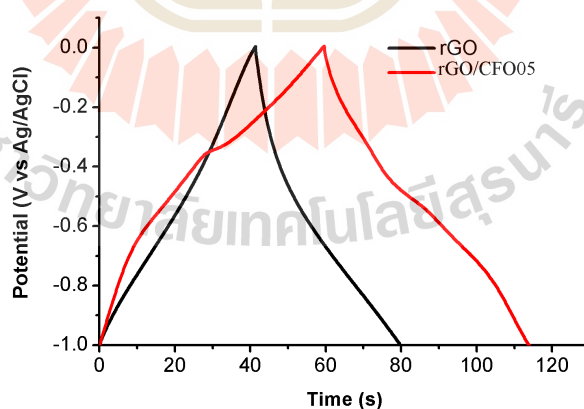
(b) Galvanostatic charge-discharge at current density of $5.0 \, \text{A/g}$

Figure 4.27 Cyclic voltammograms at scan rate of $10 \, \text{mV/s}$, and galvanostatic charge-discharge at current density of $5.0 \, \text{A/g}$ of rGO, and rGO/CFO05 in $6.0 \, \text{M}$ KOH aqueous electrolyte.

Figure 4.28 shows the specific capacitance plots of $5.0\,\text{A/g}$ of rGO, and rGO/CFO05 in $6.0\,\text{M}$ KOH aqueous electrolyte at different applied current densities. It can be found that rGO/CFO05 has highest capacitance than rGO and at all applied current densities. This can be seen that decoration of CoFe_2O_4 nanoparticles on rGO nanosheet can improve the capacitive behavior of rGO. Consequently, these results are evidence of the increasing diffusion resistance towards the ions transfer into the electrode pores and thus causing a decrease of a specific capacitance (Stoller et al., 2008).
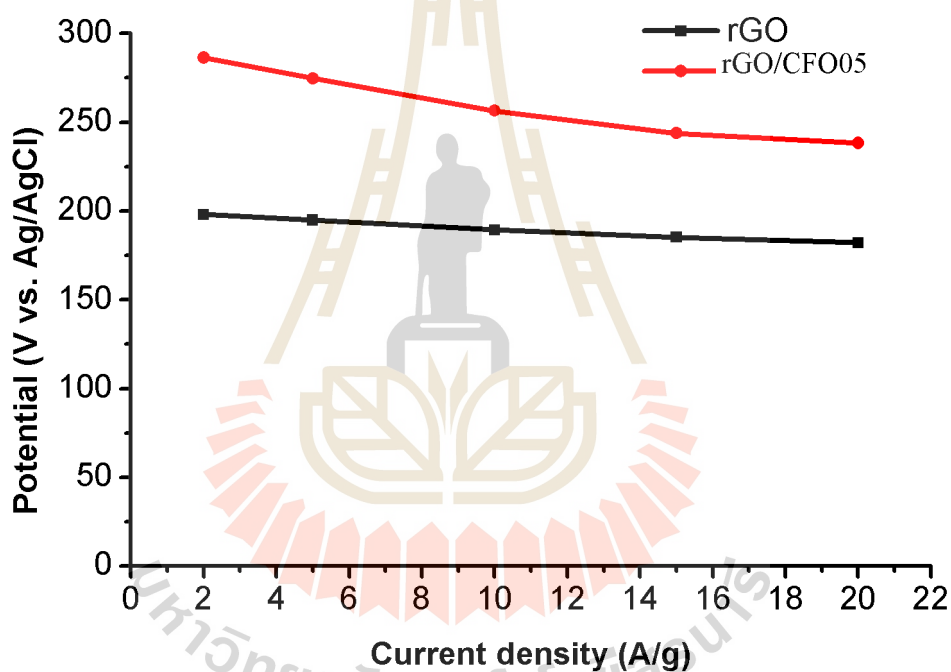
Figure 4.28 The specific capacitance plots of rGO, and rGO/CFO05 at different current densities.

Figure 4.29 shows the EIS analysis was also used to investigate the electrochemical behavior of the working electrode within the frequency range of $100\,\text{kHz} - 0.1\,\text{Hz}$ at an amplitude of $0.01\,\text{V}$. The solution resistance (E_s) or the equivalent series resistance (ESR) (Lu et al., 2010), which is obtained from the intersection of the high frequency region at the

x-axis. rGO/CFO05 has an ESR of $0.435\,\Omega$ and an R_{ct} of $0.115\,\Omega$, which is lower than those of $CoFe_2O_4$ with ESR $= 0.62\,\Omega$. This result show that, the decoration of $CoFe_2O_4$ nanoparticles on to rGO nanosheet can improve conductive performance of the materials by reducing agglomeration (Guan et al., 2014). The total resistance at the interface between the electrode and the electrolyte with the charge-transfer resistance (Rct) corresponds to the total resistance at the interface between the electrode and the electrolyte. For the charge-transfer resistance (Rct) of electrode, which is considered as the semi-circle capacitive arc high frequency region. This resistance occur between electrolyte and active material based on reaction kinetics control process. The Rct for $CoFe_2O_4$ and rGO/CFO05 are $0.67\,\Omega$ and $0.23\,\Omega$, respectively. The semi-circle of Nyquist plot show that the conductivity of $CoFe_2O_4$ is lower than rGO/CFO05 nanocomposites. The Warburg resistance, considered at the portion of the width slope of $45°$, is caused by the diffusion or transport of ions in the electrolyte on the surface of the electrode and depends on the frequency (Stoller et al., 2008). The knee frequencies of the rGO/CFO05 which is the lowest values with a slope of $45°$ before behaving as an ideal capacitor is $1.48\,Hz$. $Q1$ or CPE indicates a phase constant device. The n value of CPE depends on the behavior of the electrode is 0.998, and this can indicate that rGO/CFO05 working electrodes imply an ideal capacitor (L. Chen et al., 2013).
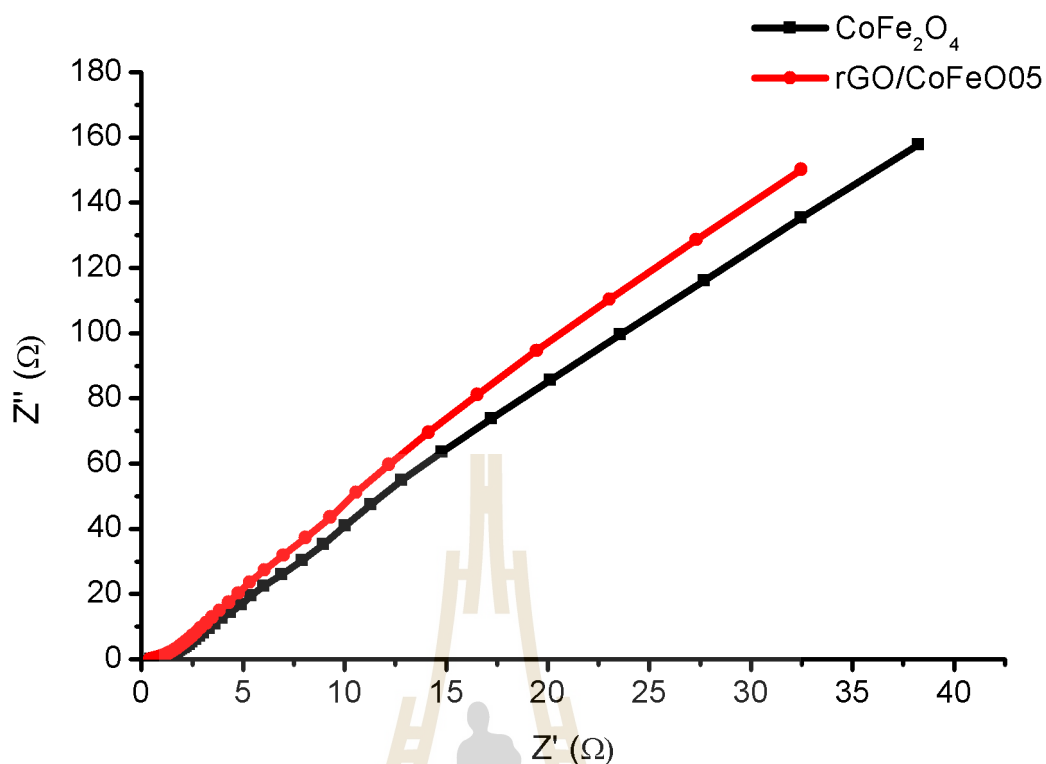
Figure 4.29 Nyquist plot of CoFe$_2$O$_4$ and rGO/CFO05 electrodes.

Moreover, to study the long-term cycle stability of the fabricated electrodes, the specific capacitance retention was evaluated by galvanostatic charge-discharge at 10.0 A/g for 1000 cycles. Figure 4.30 shows the relation between specific capacitance retention and cycle number of the charge-discharge process. After 1000 cycles of charge discharge process, the Cs of rGO/CFO05 remains 64.5% of initial capacity. It can be found that all electrodes provided the excellent cycling stability.
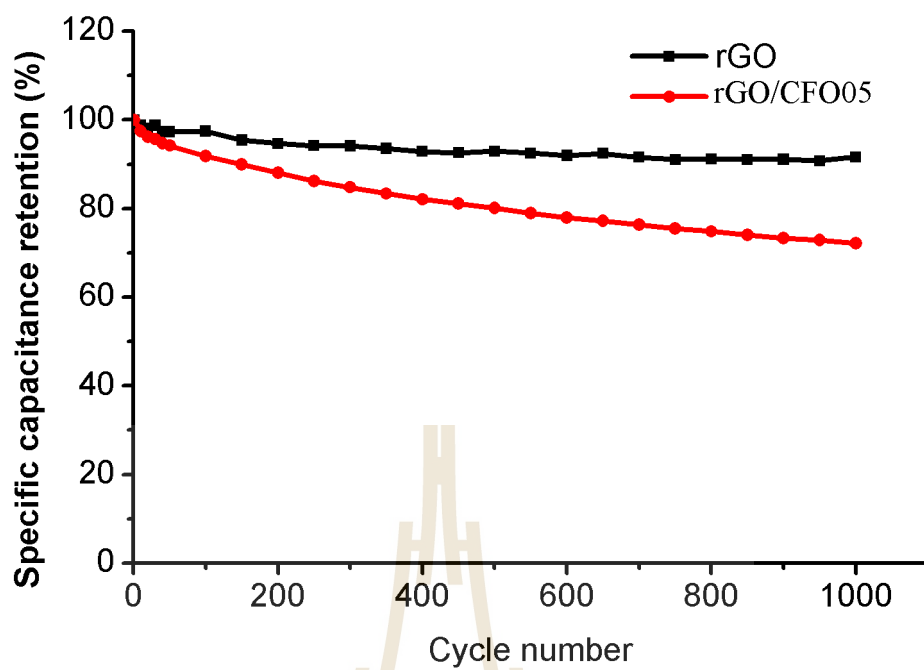
Figure 4.30 Cycling stability of rGO, and rGO/CFO05 using galvanostatic charge-

discharge at current density of 10 A/g.

CHAPTER V

CONCLUSIONS AND SUGGESTIONS

5.1 Conclusions

5.1.1 Reduced graphene oxide (rGO) preparation

We have demonstrated the synthesis of rGO, and rGO-based nanocomposite by a simple facile hydrothermal method. As following rGO preparation process, graphite oxide (GO) was prepared by oxydized graphite powder with $KMnO_4$ in 98% H_2SO_4. A characteristic peak of graphite at 26.8 °C with 0.33 nm of d-spacing was shifted to 10.70 °C with 0.83 nm d-spacing. GO powder was used as the precursor for 0.5 mg/ml graphene oxide solution by dispersion GO powder in DI water with ultrasonication for 30 min. Reduced graphene oxide (rGO) was synthesized by reduction of graphene oxide using hydrazine monohydrate ($H_4N_2 \cdot H_2O$) as a reducing agent at 200 °C for 24 h. The formation of rGO could be confirmed by XRD, TEM and Raman spectroscopy. After reduction, A characteristic peak of rGO was shown as amophous carbon dueto the random orientation of rGO sheet at 25.5 °C.

5.1.2 rGO-based nanocoposites preparation

The formation of the nanocomposite can be confirmed by the results of XRD and TEM. For rGO-based nanocomposites, its surface area is significantly higher than the surface area of metal ferrite ($MnFe_2O_4$, and $CoFe_2O_4$) nanoparticle but lower than pure

rGO. Interestingly, the specific capacitance values of 190.3, 276.9, and 144.5 F/g at a scan rate of 10 mV/s and 194.9, 274.6, and 134.4 F/g at current density of 5 A/g were obtained for the, rGO, rGO/MFO05 and rGO/MFO10, respectively.

rGO/$CoFe_2O_4$ nanocomposite were succesfully prepared by a hydrothermal method. The surface area of as-prepared material is significantly higher than the surface area of $CoFe_2O_4$ nanoparticle but lower than pure rGO, and this result is similar to the result of rGO/$MnFe_2O_4$ nanocomposite. The specific capacitance values of 190.3 and 240.5 F/g at a scan rate of 10 mV/s and 194.9, and 224.8 F/g at current density of 5.0 A/g were obtained for the rGO, and rGO/CFO05, respectively.

The addition of $MnFe_2O_4$ and $CoFe_2O_4$ nanoparticles onto rGO nanosheet can improve the electrochemical properties of rGO electrode, and the retainsion specific capacitance more than 80% after contibuous charge-discharge process for 1000 cycles. However, the specific capacitance of rGO-based nanocomposite will be lower than pure rGO electrode effected from the metal oxide concentration.

After decoration rGO nansheets by ferrite material, it can be found that the frabricated electrode of rGO-based nanocomposites, has the highest capacitance than those of the rGO. This can be seen that decoration of ferrite nanoparticles on rGO nanosheet can improve the capacitive behavior of rGO, but for moreover quantities of nanocmposites, the specificapacitance is decreased. The decreases of specific surface area, mean pore size, and large number of oxygen-containing groups on the working electrode are possibly due to the poor rate capability. Consequently, these results are evidence of the increasing diffusion resistance towards the transfer of ions into the electrode pores, and thus causing a decrease in specific capacitance.

5.2   Suggestions

From the results obtained in this study, there are some important points that are not well understood and further study is needed. These include the following issues:

5.2.1 Investigation of local structures of rGO-based nanocomposite is needed to confirm the formation of nanometal oxide onto the rGO-based nanocomposite system.

5.2.2 Investigation of electrochemical properties measurement of the working electrodes using various electrolyte in any concentration is required to confirm the suitable for fabrication of supercapacitor electrodes.

5.2.3 Investigation of the substrate material effect to the electrochemical prperties is needed to confirm the result.

All these issues would allow more understanding on the structure and properties of rGO-based nanocomposite material.
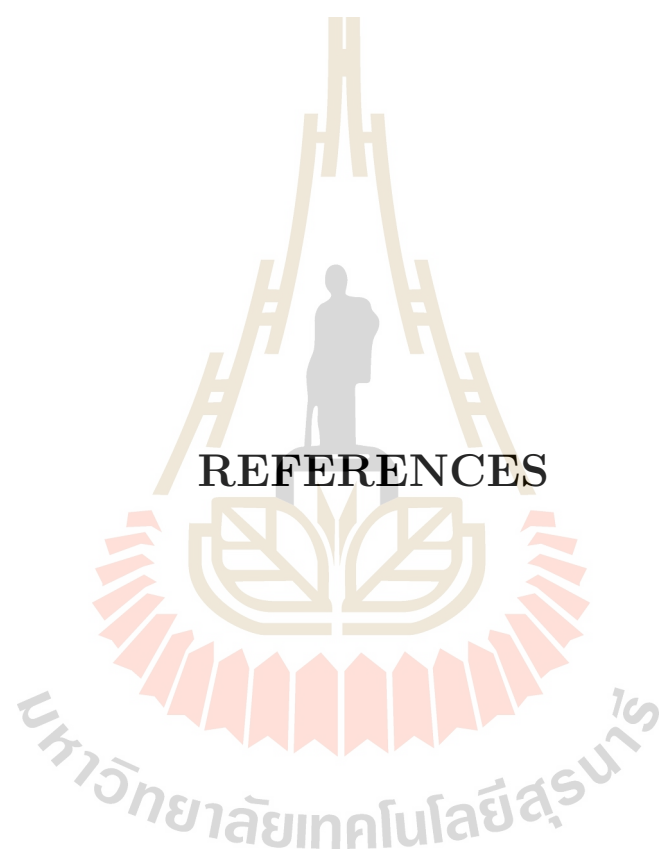
REFERENCES

REFERENCES

Ahn, Y. R., Song, M. Y., Jo, S. M., Park, C. R. and Kim, D. Y. (2006). Electrochemical capacitors based on electrodeposited ruthenium oxide on nanofibre substrates. **Nanotechnology**. 17, 2865–2869.

An, S. J., Zhu, Y., Lee, S. H., Stoller, M. D., Emilsson, T., Park, S., Velamakanni, A., An, J. and Ruoff, R. S. (2010). Thin film fabrication and simultaneous anodic reduction of deposited graphene oxide platelets by electrophoretic deposition. **Journal of Physical Chemistry Letters**. 1, 1259–1263.

Babakhani, B. and Ivey, D. G. (2010). Anodic deposition of manganese oxide electrodes with rod-like structures for application as electrochemical capacitors. **Journal of Power Sources**. 195, 2110–2117.

Balandin, A. A., Ghosh, S., Bao, W., Calizo, I., Teweldebrhan, D., Miao, F. and Lau, C. N. (2008). Superior thermal conductivity of single-layer graphene. **Nano Letters**. 8, 902–907.

Béguin, F., Presser, V., Balducci, A. and Frackowiak, E. (2014). Carbons and electrolytes for advanced supercapacitors. **Advanced Materials**. 26, 2219–2251.

Bolotin, K. I., Sikes, K. J., Jiang, Z., Klima, M., Fudenberg, G., Hone, J., Kim, P. and Stormer, H. L. (2008). Ultrahigh electron mobility in suspended graphene. **Solid State Communications**. 146, 351-355.

Brunauer, S., Emmett, P. H. and Teller, E. (1938). Adsorption of gases in multimolecular layers. **Journal of the American Chemical Society**. 60, 309–319.

Cai, W., Piner, R. D., Stadermann, F. J., Park, S., Shaibat, M. A., Ishii, Y., Yang, D., Velamakanni, A., An, S. J., Stoller, M., An, J., Chen, D. and Ruoff, R. S. (2008). Synthesis and solid-state nmr structural characterization of $^{13}C-$labeled graphite oxide. **Science**. 321, 1815-1817.

Cai, W., Zhu, Y., Li, X., Piner, R. D. and Ruoff, R. S. (2009). Large area few-layer graphene/graphite films as transparent thin conducting electrodes. **Applied Physics Letters**. 95, 123115/1–123115/3.

Casiraghi, C., Pisana, S., Novoselov, K., Geim, A. and Ferrari, A. (2007). Raman fingerprint of charged impurities in graphene. **Applied Physics Letters**. 91, 233108–233110.

Chakrabarti, M., Low, C., Brandon, N., Yufit, V., Hashim, M., Irfan, M., Akhtar, J., Ruiz-Trejo, E. and Hussain, M. (2013). Progress in the electrochemical modification of graphene-based materials and their applications. **Electrochimica Acta**. 107, 425–440.

Chen, K. and Xue, D. (2014). Water-soluble inorganic salt with ultrahigh specific capacitance: $Ce(NO_3)_3$ can be designed as excellent pseudocapacitor electrode. **Journal of colloid and interface science**. 416, 172–176.

Chen, L., Gu, N., Ding, R., Qi, L. and Wang, H. (2013). Facile fabrication of mesoporous manganese oxides as advanced electrode materials for supercapacitors. **Journal of Solid State Electrochemistry**. 17, 2579–2588.

Chen, S., Zhu, J., Wu, X., Han, Q. and Wang, X. (2010). Graphene oxide$-$ MnO_2 nanocomposites for supercapacitors. **ACS Nano**. 4, 2822-2830.

Chen, W. and Yan, L. (2010). Preparation of graphene by a low-temperature thermal reduction at atmosphere pressure. **Nanoscale**. 2, 559–563.

Chen, X.-m., Wu, G.-h., Jiang, Y.-q., Wang, Y.-r. and Chen, X. (2011). Graphene and graphene-based nanomaterials: the promising materials for bright future of electroanalytical chemistry. **Analyst**. 136, 4631–4640.

Chen, Y., Zhang, X., Yu, P. and Ma, Y. (2010). Electrophoretic deposition of graphene nanosheets on nickel foams for electrochemical capacitors. **Journal of Power Sources**. 195, 3031-3035.

Dai, B., Fu, L., Liao, L., Liu, N., Yan, K., Chen, Y. and Liu, Z. (2011). High-quality single-layer graphene via reparative reduction of graphene oxide. **Nano Research**. 4, 434–439.

Danaee, I., Jafarian, M., Forouzandeh, F., Gobal, F. and Mahjani, M. (2009). Electrochemical impedance studies of methanol oxidation on GC/Ni and GC/NiCu electrode. **International Journal of Hydrogen Energy**. 34, 859-869.

Díaz, M., Ortiz, A. and Ortiz, I. (2014). Progress in the use of ionic liquids as electrolyte membranes in fuel cells. **Journal of Membrane Science**. 469, 379–396.

Du, X., Guo, P., Song, H. and Chen, X. (2010). Graphene nanosheets as electrode material for electric double-layer capacitors. **Electrochimica Acta**. 55, 4812-4819.

Eda, G. and Chhowalla, M. (2010). Chemically derived graphene oxide: towards large-area thin-film electronics and optoelectronics. **Adv Mater**. 22, 2392-415.

Fan, Z., Zhao, Q., Li, T., Yan, J., Ren, Y., Feng, J. and Wei, T. (2012). Easy synthesis of porous graphene nanosheets and their use in supercapacitors. **Carbon**. 50, 1699-1703.

Fan, Z.-J., Kai, W., Yan, J., Wei, T., Zhi, L.-J., Feng, J., Ren, Y.-m., Song, L.-P. and Wei, F. (2010). Facile synthesis of graphene nanosheets via fe reduction of exfoliated graphite oxide. **ACS Nano**. 5, 191-198.

Feng, G., Qiao, R., Huang, J., Sumpter, B. G. and Meunier, V. (2010). Ion distribution in electrified micropores and its role in the anomalous enhancement of capacitance. **ACS Nano**. 4, 2382–2390.

Ferrari, A., Meyer, J., Scardaci, V., Casiraghi, C., Lazzeri, M., Mauri, F., Piscanec, S., Jiang, D., Novoselov, K. and Roth, S. (2006). Raman spectrum of graphene and graphene layers. **Physical Review Letters**. 97, 187401-1–187401-4.

Galiński, M., Lewandowski, A. and Stępniak, I. (2006). Ionic liquids as electrolytes. **Electrochimica Acta**. 51, 5567–5580.

Gao, W., Alemany, L. B., Ci, L. and Ajayan, P. M. (2009). New insights into the structure and reduction of graphite oxide. **Nature Chemistry**. 1, 403-408.

Geim, A. K. and Novoselov, K. S. (2007). The rise of graphene. **Nature Materials**. 6, 183-191.

Gómez-Navarro, C., Weitz, R. T., Bittner, A. M., Scolari, M., Mews, A., Burghard, M. and Kern, K. (2007). Electronic transport properties of individual chemically reduced graphene oxide sheets. **Nano Letters**. 7, 3499-3503.

Gogotsi, Y. (2011). Controlling graphene properties through chemistry. **Journal of Physical Chemistry Letters**. 2, 2509–2510.

González, A., Goikolea, E., Barrena, J. A. and Mysyk, R. (2016). Review on supercapacitors: Technologies and materials. **Renewable and Sustainable Energy Reviews**. 58, 1189–1206.

Guan, Q., Cheng, J., Wang, B., Ni, W., Gu, G., Li, X., Huang, L., Yang, G. and Nie, F. (2014). Needle-like Co_3O_4 anchored on the graphene with enhanced electrochemical performance for aqueous supercapacitors. **ACS Applied Materials & Interfaces**. 6, 7626–7632.

Hernandez, Y., Nicolosi, V., Lotya, M., Blighe, F. M., Sun, Z., De, S., McGovern, I., Holland, B., Byrne, M., Gun'Ko, Y. K. et al. (2008). High-yield production of graphene by liquid-phase exfoliation of graphite. **Nature Nanotechnology**. 3, 563–568.

Houshiar, M., Zebhi, F., Razi, Z. J., Alidoust, A. and Askari, Z. (2014). Synthesis of cobalt ferrite ($CoFe_2O_4$) nanoparticles using combustion, coprecipitation, and precipitation methods: a comparison study of size, structural, and magnetic properties. **Journal of Magnetism and Magnetic Materials**. 371, 43–48.

Hu, C.-C., Huang, C.-M. and Chang, K.-H. (2008). Anodic deposition of porous vanadium oxide network with high power characteristics for pseudocapacitors. **Journal of Power Sources**. 185, 1594–1597.

Hu, C.-C., Huang, Y.-H. and Chang, K.-H. (2002). Annealing effects on the physicochemical characteristics of hydrous ruthenium and ruthenium-iridium oxides for electrochemical supercapacitors. **Journal of Power Sources**. 108, 117–127.

Huang, J., Sumpter, B. G. and Meunier, V. (2008). Theoretical model for nanoporous carbon supercapacitors. **Angewandte Chemie International Edition**. 47, 520–524.

Huang, X., Zeng, Z., Fan, Z., Liu, J. and Zhang, H. (2012). Graphene-based electrodes. **Advanced Materials**. 24, 5979–6004.

Huang, Y., Dong, X., Shi, Y., Li, C. M., Li, L. J. and Chen, P. (2010). Nanoelectronic biosensors based on CVD grown graphene. **Nanoscale**. 2, 1485–1488.

Hummers Jr, W. S. and Offeman, R. E. (1958). Preparation of graphitic oxide. **Journal of the American Chemical Society**. 80, 1339–1339.

Jagannadham, K. (2012). Thermal conductivity of copper-graphene composite films syn-

thesized by electrochemical deposition with exfoliated graphene platelets. **Met-allurgical and Materials Transactions B**. 43, 316–324.

Jiang, J., Li, Y., Liu, J., Huang, X., Yuan, C. and Lou, X. W. D. (2012). Recent advances in metal oxide-based electrode architecture design for electrochemical energy storage. **Advanced Materials**. 24, 5166–5180.

Joshi, R., Carbone, P., Wang, F.-C., Kravets, V. G., Su, Y., Grigorieva, I. V., Wu, H., Geim, A. K. and Nair, R. R. (2014). Precise and ultrafast molecular sieving through graphene oxide membranes. **Science**. 343, 752–754.

Kandalkar, S., Dhawale, D., Kim, C.-K. and Lokhande, C. (2010). Chemical synthesis of cobalt oxide thin film electrode for supercapacitor application. **Synthetic Metals**. 160, 1299–1302.

Kandalkar, S., Gunjakar, J. and Lokhande, C. (2008). Preparation of cobalt oxide thin films and its use in supercapacitor application. **Applied Surface Science**. 254, 5540–5544.

Kim, K. S., Zhao, Y., Jang, H., Lee, S. Y., Kim, J. M., Kim, K. S., Ahn, J. H., Kim, P., Choi, J. Y. and Hong, B. H. (2009). Large-scale pattern growth of graphene films for stretchable transparent electrodes. **Nature**. 457, 706-710.

Kisacikoglu, M., Uzunoglu, M. and Alam, M. (2009). Load sharing using fuzzy logic control in a fuel cell/ultracapacitor hybrid vehicle. **International Journal of Hydrogen Energy**. 34, 1497-1507.

Kötz, R. and Carlen, M. (2000). Principles and applications of electrochemical capacitors. **Electrochimica Acta**. 45, 2483–2498.

Kötz, R. and Carlen, M. (2000). Principles and applications of electrochemical capacitors. **Electrochimica Acta**. 45, 2483-2498.

Kuo, S.-L. and Wu, N.-L. (2007). Electrochemical capacitor of $MnFe_2O_4$ with organic li-ion electrolyte. **Electrochemical and Solid-state Letters**. 10, A171–A175.

Lai, C.-H., Lin, C.-K., Lee, S.-W., Li, H.-Y., Chang, J.-K. and Deng, M.-J. (2012). Nanostructured na-doped vanadium oxide synthesized using an anodic deposition technique for supercapacitor applications. **Journal of Alloys and Compounds**. 536, S428–S431.

Lao, Z. J., Konstantinov, K., Tournaire, Y., Ng, S. H., Wang, G. and Liu, H.-K. (2006). Synthesis of vanadium pentoxide powders with enhanced surface-area for electrochemical capacitors. **Journal of power sources**. 162, 1451–1454.

Largeot, C., Portet, C., Chmiola, J., Taberna, P.-L., Gogotsi, Y. and Simon, P. (2008). Relation between the ion size and pore size for an electric double-layer capacitor. **Journal of the American Chemical Society**. 130, 2730–2731.

Lee, C., Wei, X., Kysar, J. W. and Hone, J. (2008). Measurement of the elastic properties and intrinsic strength of monolayer graphene. **Science**. 321, 385-388.

Li, D., Mueller, M. B., Gilje, S., Kaner, R. B. and Wallace, G. G. (2008). Processable aqueous dispersions of graphene nanosheets. **Nature Nanotechnology**. 3, 101–105.

Li, J., Xu, Q., Peng, Q., Pang, M., He, S. and Zhu, C. (2006). Supercritical CO_2-assisted synthesis of polystyrene/clay nanocomposites via in situ intercalative polymerization. **Journal of Applied Polymer Science**. 100, 671–676.

Li, X., Magnuson, C. W., Venugopal, A., Tromp, R. M., Hannon, J. B., Vogel, E. M., Colombo, L. and Ruoff, R. S. (2011). Large-area graphene single crystals grown by low-pressure chemical vapor deposition of methane on copper. **Journal of the American Chemical Society**. 133, 2816–2819.

Li, X.-H., Kurasch, S., Kaiser, U. and Antonietti, M. (2012). Synthesis of monolayer-patched graphene from glucose. **Angewandte Chemie International Edition**. 51, 9689–9692.

Liu, C., Li, F., Ma, L.-P. and Cheng, H.-M. (2010). Advanced materials for energy storage. **Advanced Materials**. 22 .

Liu, H., Liu, Y. and Li, J. (2010). Ionic liquids in surface electrochemistry. **Physical Chemistry Chemical Physics**. 12, 1685–1697.

Lu, T., Zhang, Y., Li, H., Pan, L., Li, Y. and Sun, Z. (2010). Electrochemical behaviors of graphene–zno and graphene–sno 2 composite films for supercapacitors. **Electrochimica Acta**. 55, 4170–4173.

Miller, J. R. and Simon, P. (2008). Materials science. electrochemical capacitors for energy management. **Science**. 321, 651-652.

Nakayama, M., Tanaka, A., Sato, Y., Tonosaki, T. and Ogura, K. (2005). Electrodeposition of manganese and molybdenum mixed oxide thin films and their charge storage properties. **Langmuir**. 21, 5907–5913.

Nelson, P. A. and Owen, J. R. (2003). A high-performance supercapacitor/battery hybrid incorporating templated mesoporous electrodes. **Journal of The Electrochemical Society**. 150, A1313–A1317.

Novoselov, K. S., Geim, A. K., Morozov, S., Jiang, D., Zhang, Y., Dubonos, S., Grigorieva, I. and Firsov, A. (2004). Electric field effect in atomically thin carbon films. **Science**. 306, 666-669.

Pandolfo, A. and Hollenkamp, A. (2006). Carbon properties and their role in supercapacitors. **Journal of Power Sources**. 157, 11-27.

Park, S. and Ruoff, R. S. (2009). Chemical methods for the production of graphenes.

Nature Nanotechnology. 4, 217-224.

Patake, V., Lokhande, C. and Joo, O. S. (2009). Electrodeposited ruthenium oxide thin films for supercapacitor: Effect of surface treatments. **Applied Surface Science**. 255, 4192–4196.

Patil, U., Salunkhe, R., Gurav, K. and Lokhande, C. (2008). Chemically deposited nanocrystalline NiO thin films for supercapacitor application. **Applied Surface Science**. 255, 2603–2607.

Pei, S. and Cheng, H.-M. (2012). The reduction of graphene oxide. **Carbon**. 50, 3210-3228.

Pell, W. and Conway, B. (2001). Voltammetry at a de levie brush electrode as a model for electrochemical supercapacitor behaviour. **Journal of Electroanalytical Chemistry**. 500, 121–133.

Portet, C., Taberna, P. L., Simon, P. and Laberty-Robert, C. (2004). Modification of al current collector surface by sol–gel deposit for carbon–carbon supercapacitor applications. **Electrochimica Acta**. 49, 905-912.

Shao, G., Lu, Y., Wu, F., Yang, C., Zeng, F. and Wu, Q. (2012). Graphene oxide: the mechanisms of oxidation and exfoliation. **Journal of Materials Science**. 47, 4400–4409.

Shao, Q., Tang, J., Lin, Y., Li, J., Qin, F., Zhang, K., Yuan, J. and Qin, L.-C. (2015). Ionic liquid modified graphene for supercapacitors with high rate capability. **Electrochimica Acta**. 176, 1441-1446.

Sharma, P. and Bhatti, T. (2010). A review on electrochemical double-layer capacitors. **Energy Conversion and Management**. 51, 2901–2912.

Shin, H.-J., Kim, K. K., Benayad, A., Yoon, S.-M., Park, H. K., Jung, I.-S., Jin, M. H.,

Jeong, H.-K., Kim, J. M., Choi, J.-Y. and Lee, Y. H. (2009). Efficient reduction of graphite oxide by sodium borohydride and its effect on electrical conductance. **Advanced Functional Materials**. 19, 1987-1992.

Simon, P. and Gogotsi, Y. (2008). Materials for electrochemical capacitors. **Nature Materials**. 7, 845-854.

Stankovich, S., Dikin, D. A., Dommett, G. H., Kohlhaas, K. M., Zimney, E. J., Stach, E. A., Piner, R. D., Nguyen, S. T. and Ruoff, R. S. (2006a). Graphene-based composite materials. **Nature**. 442, 282–286.

Stankovich, S., Dikin, D. A., Dommett, G. H., Kohlhaas, K. M., Zimney, E. J., Stach, E. A., Piner, R. D., Nguyen, S. T. and Ruoff, R. S. (2006b). Graphene-based composite materials. **Nature**. 442, 282–286.

Stoller, M. D., Park, S., Zhu, Y., An, J. and Ruoff, R. S. (2008). Graphene-based ultracapacitors. **Nano letters**. 8, 3498–3502.

Stoller, M. D. and Ruoff, R. S. (2010). Best practice methods for determining an electrode material's performance for ultracapacitors. **Energy** $\&$ **Environmental Science**. 3, 1294–1301.

Sugimoto, W., Iwata, H., Murakami, Y. and Takasu, Y. (2004). Electrochemical capacitor behavior of layered ruthenic acid hydrate. **Journal of The electrochemical society**. 151, A1181–A1187.

Tang, H., Gao, P., Xing, A., Tian, S. and Bao, Z. (2014). One-pot low-temperature synthesis of a $MnFe_2O_4 - -$graphene composite for lithium ion battery applications. **RSC Advances**. 4, 28421–28425.

Thakur, S. and Karak, N. (2012). Green reduction of graphene oxide by aqueous phytoextracts. **Carbon**. 50, 5331–5339.

Vivekchand, S., Rout, C. S., Subrahmanyam, K., Govindaraj, A. and Rao, C. (2008). Graphene-based electrochemical supercapacitors. **Journal of Chemical Sciences**. 120, 9-13.

Wang, D.-W., Li, F., Zhao, J., Ren, W., Chen, Z.-G., Tan, J., Wu, Z.-S., Gentle, I., Lu, G. Q. and Cheng, H.-M. (2009). Fabrication of graphene/polyaniline composite paper via in situ anodic electropolymerization for high-performance flexible electrode. **Acs Nano**. 3, 1745-1752.

Wang, G., Zhang, L. and Zhang, J. (2012). A review of electrode materials for electrochemical supercapacitors. **Chemical Society Reviews**. 41, 797–828.

Wang, H. and Hu, Y. H. (2011). Effect of oxygen content on structures of graphite oxides. **Industrial** & **Engineering Chemistry Research**. 50, 6132–6137.

Wang, Y., Shi, Z., Huang, Y., Ma, Y., Wang, C., Chen, M. and Chen, Y. (2009). Supercapacitor devices based on graphene materials. **Journal of Physical Chemistry C**. 113, 13103-13107.

Wei, L. and Yushin, G. (2012). Nanostructured activated carbons from natural precursors for electrical double layer capacitors. **Nano Energy**. 1, 552–565.

Yan, J., Liu, J., Fan, Z., Wei, T. and Zhang, L. (2012). High-performance supercapacitor electrodes based on highly corrugated graphene sheets. **Carbon**. 50, 2179-2188.

Yan, J., Wei, T., Cheng, J., Fan, Z. and Zhang, M. (2010). Preparation and electrochemical properties of lamellar MnO_2 for supercapacitors. **Materials Research Bulletin**. 45, 210–215.

Yan, J., Wei, T., Fan, Z., Qian, W., Zhang, M., Shen, X. and Wei, F. (2010). Preparation of graphene nanosheet/carbon nanotube/polyaniline composite as electrode material for supercapacitors. **Journal of Power Sources**. 195, 3041-3045.

Yan, J., Wei, T., Shao, B., Fan, Z., Qian, W., Zhang, M. and Wei, F. (2010). Preparation of a graphene nanosheet/polyaniline composite with high specific capacitance. **Carbon**. 48, 487-493.

Yu, Y., Zhai, Y., Liu, H. and Li, L. (2016). Single-layer MnO_2 nanosheets: From controllable synthesis to free-standing film for flexible supercapacitors. **Materials Letters**. 176, 33–37.

Zhang, K., Zhang, L. L., Zhao, X. S. and Wu, J. (2010). Graphene/polyaniline nanofiber composites as supercapacitor electrodes. **Chemistry of Materials**. 22, 1392-1401.

Zhang, L. L., Zhou, R. and Zhao, X. S. (2010). Graphene-based materials as supercapacitor electrodes. **Journal of Materials Chemistry**. 20, 5983-5992.

Zhang, M., Jia, M., Jin, Y., Wen, Q. and Chen, C. (2013). Reduced graphene oxide/$CoFe_2O_4Co$ nanocomposite as high performance anode for lithium ion batteries. **Journal of Alloys and Compounds**. 566, 131-136.

Zhou, X., Zhang, J., Wu, H., Yang, H., Zhang, J. and Guo, S. (2011). Reducing graphene oxide via hydroxylamine: a simple and efficient route to graphene. **Journal of Physical Chemistry C**. 115, 11957-11961.

Zhu, C., Guo, S., Fang, Y. and Dong, S. (2010). Reducing sugar: new functional molecules for the green synthesis of graphene nanosheets. **ACS Nano**. 4, 2429-2437.

Zhu, J. and He, J. (2012). Facile synthesis of graphene-wrapped honeycomb MnO_2 nanospheres and their application in supercapacitors. **ACS Applied Materials** & **Interfaces**. 4, 1770-1776.

Zhu, X., Liu, Q., Zhu, X., Li, C., Xu, M. and Liang, Y. (2012). Reduction of graphene oxide via ascorbic acid and its application for simultaneous detection of dopamine and

ascorbic acid. **Int. J. Electrochem. Sci**. 7, 5172–5184.

Zhu, Y., James, D. K. and Tour, J. M. (2012). New routes to graphene, graphene oxide and their related applications. **Advanced Materials**. 24, 4924-4955.
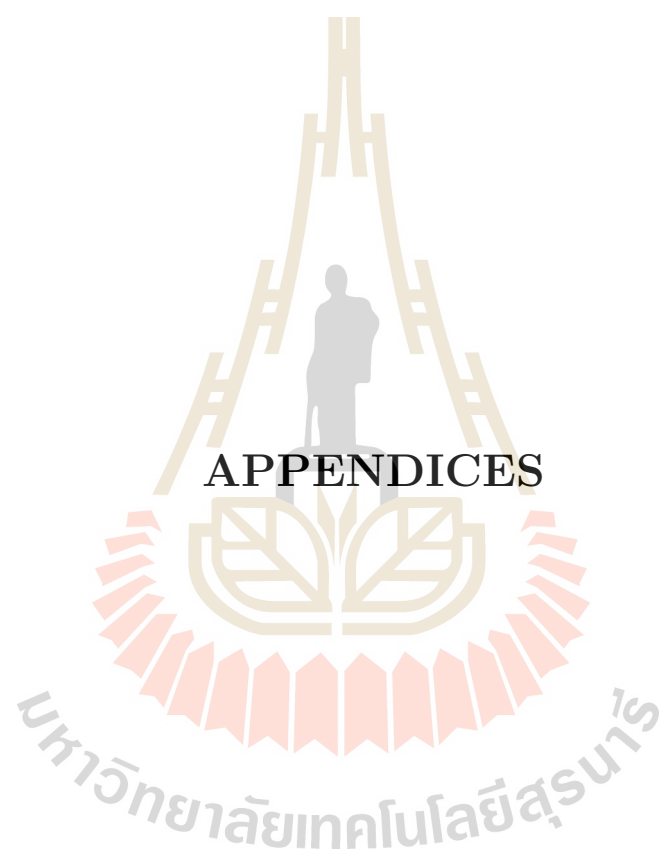
APPENDICES

APPENDIX A

PAPER PUBLICATIONS

1. Kotutha I, Swatsitang E, Meewassana W, and Maensiri S. One-pot hydrothermal synthesis, characterization, and electrochemical properties of $rGO/MnFe_2O_4$ nanocomposites. Jpn. Journal of Apply Physics, 54, 06FH10 (2015).

2. Kotutha I, Swatsitang E, Meewassana W, and Maensiri S. Synthesis of $rGO/CoFe_2O_4$ composites and its electrochemical properties for energy storage application. (Manuscript, submitted to Ceramics International).

APPENDIX B

PRESENTATIONS

1. Kotutha I, Swatsitang E, Meewassana W, and Maensiri S. Hydrothermal Synthesis, Characterization, and Electrochemical Properties of rGO/MFe_2O_4 (M = Co, Mn) Nanocomposite. RGJ-Ph.D. Congress XVI "ASEAN: Emerging Research Opportunities"; June 11-13, 2015, Jomtien Palm Beach Hotel And Resort, Pattaya, Thailand. (Oral presentation)

2. Kotutha I, Swatsitang E, Meewassana W, and Maensiri S. Effect of $CoFe_2O_4$ nanoparticles and rGO nanosheets ratio on the Electrochemical Performance of $rGO/CoFe_2O_4$ nanocomposite. The 4th Thailand International Nanotechnology Conference 2014; November 25-28, 2014, Thailand Science Park Convention Center, Pathumthani, Thailand. (Oral presentation)

3. Kotutha I, Swatsitang E, Meewassana W, and Maensiri S. One-pot hydrothermal synthesis, characterization, and electrochemical properties of $rGO/MnFe_2O_4$ nanocomposite. 27th International Microprocesses and Nanotechnology Conference, November 4-7, 2014, Fukuoka, Japan. (Oral presentation)

4. Kotutha I, Swatsitang E, Meewassana W, and Maensiri S. One-pot hydrothermal synthesis, characterization, and electrochemical properties of $rGO/CoFe_2O_4$ nanocomposite. The 19th International Conference on Ternary and Multinary

Compounds (ICTMC-19) TOKI MESSE, Niigata, Japan and from Sept. 1 to Sept. 5, 2014. (Poster presentation)

5. Kotutha I, Swatsitang E, and Maensiri S. Synthesis of rGO/Ag Nanocomposites via Chemical Reduction of Exfoliated Graphite Oxide. The 3rd Academic Conference on Natural Science for Master and PhD. Students from ASEAN countries (CASEAN-2013); November 11-15, 2013, Phnom Penh, Cambodia. (Poster presentation)

CURRICULUM VITAE

Name: Mr. Isara Kotutha

Date of Birth: 16th October 1973

Place of Birth: Roi Et, Thailand.

Education:

2010-2016   **Ph.D. candidate in Physics**

School of Physics, Institute of Science,

Suranaree University of Technology,

Nakhon Ratchasima, Thailand

Synthesis, Characterization and Electrochemical Properties of

Reduced Graphene Oxide/Ferrite Nanocomposites

2001-2005   **M.Sc. (Physics)**

Department of Physics, Faculty of Science,

Khon Kaen University, Khon Kaen, Thailand

A High Temperature Solar Furnace

Assoc. Prof. Dr.Ekaphan Swatsitang

1998-2001   **B. Sc. (Physics)**

Department of Physics, Faculty of Science,

Khon Kaen University, Khon Kaen, Thailand

Trace metal quantity measurement by EDXRF technigue

Assoc. Prof. Dr.Ekaphan Swatsitang